CROPS WATER STATUS QUANTIFICATION USING THERMAL AND MULTISPECTRAL SENSING TECHNOLOGIES

by

Yan Zhu

A Dissertation

Submitted to the Faculty of Purdue University

In Partial Fulfillment of the Requirements for the degree of

Doctor of Philosophy

School of Agricultural and Biological Engineering

West Lafayette, Indiana

May 2022

THE PURDUE UNIVERSITY GRADUATE SCHOOL
STATEMENT OF COMMITTEE APPROVAL

Dr. Keith A. Cherkauer, Chair
Department of Agricultural and Biological Engineering

Dr. Melba M. Crawford
Department of Civil Engineering

Dr. Mitchell R. Tuinstra
Department of Agronomy

Dr. Ayman Habib
Department of Civil Engineering

Dr. Dharmendra Saraswat
Department of Agricultural and Biological Engineering

Approved by:
Dr. Nathan Mosier

ACKNOWLEDGMENTS

The information, data, or work presented herein was funded in part by the Advanced Research Projects Agency-Energy (ARPA-E), U.S. Department of Energy, under Award Number DE-AR0000593.

TABLE OF CONTENTS

LIST OF TABLES

LIST OF FIGURES

LIST OF ABBREVIATIONS

ACRE	Agronomy Center for Research and Education
CT	Canopy Temperature
CWSI	Crop Water Stress Index
DAP	Days after Planting
DSM	Digital Surface Model
ET	Evapotranspiration
EDT	Eastern Daylight Time
FAO	Food and Agriculture Organization
FC	Field Capacity
G	Reflectance in Green Band
GCP	Ground Control Point
GOES	Geostationary Operational Environmental Satellites
GRVI	Green Red Vegetation Index
H	Heritability
LAI	Leaf Area Index
LE	Latent Heat Flux
LST	Land Surface Temperature
MAE	Mean Absolute Error
MODIS	Moderate Resolution Imaging Spectroradiometer
MODTRAN	MODerate resolution atmospheric TRANsmission
NCSS	National Cooperative Soil Survey
NEDT	Noise Equivalent Temperature Difference
NIST	National Institute of Standards and Technology
NIR	Reflectance in Near Infrared Band
OSAVI	Optimized Soil-Adjusted Vegetation Index
OSEB	One-Source Energy Balance
PM	Penman-Monteith Equation
PRI	Photochemical Reflectance Index
R	Reflectance in Red Band
REI	Red-edge Ratio
RMSE	Root Mean Square Error
RTD	Resistance Temperature Detector
SM	Soil Moisture
SMI	Soil Moisture Index
TCARI	Transformed Chlorophyll in Reflectance Index
TSEB	Two-Source Energy Balance Model
UAS	Unmanned Aircraft System
UAV	Unmanned Aerial Vehicle
WRI	World Resources Institute
WP	Wilting Point

ABSTRACT

Thermal and multispectral imagery can provide users with insights into the water stress status and evapotranspiration demand of crops. However, traditional platforms, such as satellites, for these thermal and multispectral sensors are limited in their usefulness due to low spatial and temporal resolution. Small unmanned aircraft system (UAS) have the potential to have similar sensors installed and provide canopy temperature and reflectance information at spatial and temporal resolutions more useful for crop management; however, most of the existing research on the calibration or the estimation of water status were established based on the satellite platforms either for the sensors calibration or water status quantification. There is, therefore, a need to develop methods specifically for UAS-mounted sensors. In this research, a pixel-based calibration and an atmospheric correction method based on in-field approximate blackbody sources were developed for an uncooled thermal camera, and the higher accurate vegetative temperature acquired after calibration was used as inputs to an algorithm developed for high-resolution thermal imagery for calculating crop latent heat flux. At last, a thermal index based on the Bowen ratio is proposed to quantify the water deficit stress in a crop field, along with this, a method for plot-level analysis of various vegetation and thermal indices have been demonstrated to illustrate its broad application to genetic selection. The objective was to develop a workflow to use high-resolution thermal and multispectral imagery to derive indices that can quantify crops water status on a plot level which will facilitate the research related to breeding selection.

The camera calibration method can effectively reduce the root mean square error (RMSE) and variability of measurements. The pixel-based thermal calibration method presented here was able to reduce the measurement uncertainty across all the pixels in the images, thus improving the accuracy and reducing the between-pixel variability of the measurements. During field calibration, the RMSE values relative to ground reference targets for two flights in 2017 were reduced from 6.36°C to 1.24°C and from 4.56°C to 1.32°C, respectively. The latent heat flux estimation algorithm yields an RMSE of 65.23 W/m^2 compared with the ground reference data acquired from porometer. The Bowen ratio has a high correlation with drought conditions quantified using the soil moisture index, stomatal conductance, and crop water stress index (CWSI), which indicates

the potential of this index to be used as a water deficit stress indicator. The thermal and multispectral indices on a plot level displayed will facilitate the breeding selection.

1. INTRODUCTION

According to data from World Resources Institute (WRI) (2019), more than a billion people currently live in water-scarce regions, and as many as 3.5 billion could experience water scarcity by 2025. Since agricultural water use comprises a significant part of total consumptive water, one of the most efficient ways to reduce water stress is to increase crop water use efficiency.

Canopy temperature information can be related to stomatal conductance (Bower et al., 2009; Jones, 1999; Baluja et al., 2012; Berni et al., 2009a), and evapotranspiration (ET) estimation (Maes and Steppe, 2012; Hoffmann et al., 2016). Both of these are important traits for crop phenotyping and genotypic selection. Canopy temperature (CT) has often been measured by hand-held thermometers. However, the application of hand-held instruments in large fields is laborious, time-consuming and sensitive to weather fluctuations over short periods of time. Moreover, difficulties associated with maintaining a constant view angle and avoiding "contamination" from soil further complicate hand-held CT measurements (Deery et al., 2016). Because of these disadvantages, recent studies have focused on the possibilities of using remote sensing method for acquiring temperature information for various crops.

Historically, satellite sensors have provided relatively accessible remotely sensed data including land surface temperature information with worldwide coverage. Common satellites with thermal sensors are Geostationary Operational Environmental Satellites (GOES), Moderate Resolution Imaging Spectroradiometer (MODIS) Terra/Aqua and Landsat ETM+/TIRS. The spatial resolution of these sensors range from 5 km to 30 m and their temporal resolution varies from 1 day to 16 days (Torres-Rua et al., 2017). However, these combinations of repeat times and spatial resolutions are not favorable for many agricultural applications, such as plant breeding, which require sub-meter resolution and multiple observations at specific times of a day. The advent of small unmanned aircraft systems (UAS) with mounted thermal cameras can be used to monitor the canopy temperature with higher spatial, temporal resolution compared with satellites.

Currently, thermal cameras can be classified into two categories: cooled and uncooled cameras. A cooled thermal camera usually has higher sensitivity and spatial resolution as a result of having a

cryocooler installed which helps reduce thermally-induced noise and thus can sense shorter infrared wavelengths. Also, a cooled thermal camera has a faster capture rate and the ability to easily perform spectral filtering in order to uncover details and take measurements that otherwise would be unachievable with uncooled thermal cameras (FLIR® Systems, Inc.2018). Although cooled thermal cameras have several advantages over uncooled cameras, high cost and large size limit their applications on the small UAS. So, currently, uncooled thermal cameras are considered to be the most useful for UAS based flights for agriculture research.

The sensors in the uncooled thermal camera are designed to be sensitive to the radiance emitted from target objects however, the response of each detector can be different even for the same temperature (non-uniformity effects). Additionally, when viewing an object from a distance, thermal energy tends to be absorbed and attenuated by the media through which it passes especially the atmosphere. Removing the effects of the uncooled camera and the atmosphere are necessary steps for thermal sensing to get accurate temperature estimates of target objects, as these factors contribute to the inaccuracy in temperature estimation. The factory reported accuracy of the uncooled FLIR thermal is ±5°C regardless of the atmospheric effects. This means that calibration of the camera and correction for atmospheric effects are both important for an uncooled thermal camera mounted on an unmanned aerial vehicle (UAV).

There are two commonly used radiometric calibration methods: internal blackbody source referencing and air-to-ground calibration. The first method takes the form of two temperature-controlled ("hot" and "cold") blackbody radiation sources positioned so that they are viewed by the sensor periodically during flight. By comparing the signal recorded from the earth's surface to the radiation from these two precisely controlled blackbody calibration sources, a mathematical relationship can be established to calibrate the sensor. This methodology accounts for temperature drift in the camera but does not account for the atmospheric effects. The other method is air-to-ground calibration which corrects for atmospheric effects and can be used for temperature drift if targets are observed multiple times during flight operations. Observations are typically made at points where temperatures are assumed to be constant. The corresponding scanner output value is then determined for each point of ground-based surface temperature measurement. A calibration

curve is then constructed relating the scanned output values to the corresponding ground-based radiant temperature (Lillesand et al., 2014).

Atmospheric effects can also be accounted for in thermal image calibration by using radiative transfer models like the MODTRAN model, which takes air temperature, relative humidity, barometric pressure, atmospheric transmittance emissivity, downwelling and upwelling thermal radiation as inputs. (Berni et al., 2009b, Maes, Huete and Steppe, 2017, Maes and Steppe, 2012).

Accurate temperature measurements will improve estimates of evapotranspiration based on them. Evapotranspiration (latent heat flux) has played a key role in determining the water status of crops and thus serving as an important indicator for management of irrigation and water resources in areas of water scarcity (Anderson et al., 2012). However, direct measurements of evapotranspiration (ET) require measurements of turbulent fluxes and the mass change of an isolated soil volume and the plants growing in it can be infeasible or too expensive (Todd et al., 2000). There are several control factors for ET. The primary weather factors are solar radiation, humidity and wind speed. Air temperature has a minor direct impact on evaporation (E) or ET rate, although it has been highly correlated with both solar radiation and ET. Other factors such as type of vegetation, soil and management factors can also affect the rate of ET (Jensen and Allen, 2016; Allen et al., 1998). Traditional measurement systems for ET include: lysimetry (measures evaporation and transpiration based on the change in weight of a lysimeter) (Marek et al., 1988; Howell et al., 1985), eddy covariance systems (directly quantify ET by measuring wind velocity, water vapor content of different air fluxes) (Swinbank, 1951), Bowen Ratio energy balance systems (indirectly quantify ET by measuring net radiation, soil heat flux and vapor pressure at two different heights based on Bowen ratio energy balance equation) (Bowen 1926), and remote sensing platforms (unmanned aircraft systems and satellites) with thermal sensors installed (Singh and Irmak, 2009; Jensen and Allen, 2016; Anderson et al., 2012).

In order to accommodate remote sensing technology for surface flux prediction. Some models based on energy balance theory have been created to indirectly quantify the latent heat flux. In these models, an assumption of no significant heat advection has been made (Hoffmann et al., 2016), so that net radiation can be divided into three components: sensible heat flux, latent heat flux and soil heat flux. Successful estimations of the other two components will lead to an

estimation of latent heat flux. Among the numerous models that have been developed, dual-source models have proved to be superior to one-source models in many ways. This is mainly due to the fact that one-source models simulate bulk ET from the land surface by primarily using remotely sensed land surface temperature and vegetation index while two-source models represent physical processes and simulate evaporation (E) and transpiration (T) separately over larger areas. The latter could be more useful for understanding the hydrological and biological processes of the terrestrial biosphere (Yang et al., 2015). Norman et al. (1995) introduced an iterative method known as Two-Source Energy Balance Model (TSEB) to calculate latent heat flux of canopy and soil by using remote measurements of surface directional brightness temperature and some ancillary data. This is a two-layer model where energy fluxes are partitioned between the soil and vegetation (Norman et al., 1995). In this model, brightness temperature is assumed to be available only at a single viewing angle so a Priestly-Taylor approximation (Priestley and Taylor, 1972) is used to acquire an initial estimation of canopy temperature then E and T are calculated in an iterative manner. Other dual-source models include the hybrid dual-source and trapezoid framework-based ET model (HTEM) and MOD16 ET algorithm (Yang et al., 2015).

Most evapotranspiration prediction models are developed for satellite remote sensing systems. Because of the coarse temporal and spatial resolution of satellites, there are usually many assumptions in the models and these assumptions will degrade the prediction accuracy. With the increased availability of high-quality thermal cameras and inexpensive UAS platforms, new opportunities have opened up to use remote sensing to study latent heat fluxes within fields or between experimental plots. To perform these studies on a field or a plot level, however, the assumptions made in models developed for satellites will need to be reevaluated.

Crop water stress is a deficiency in water supply, detected as a reduction in soil water content or from the physiological responses of the plant to water deficiency. In response to a water deficit stress, ion- and water-transport systems across membranes function to control turgor pressure changes in guard cells and stimulate stomatal closure which results in decreasing in CO2 absorption thus impacting photosynthesis and plant growth (Osakabe et al., 2014). Severe water stress may cause crop physiological damage, yield loss and other irreversible damages (Ihuoma and Madramootoo, 2017). There are several ways to quantify water stress levels: soil water balance

approaches, plant-based approaches as well as remote sensing approaches. Although the first two approaches can provide relatively accurate estimation of soil water status, they are usually labor intensive and can only offer point measurements which can be a problem if field scale information is required. Remote sensing technologies can offer information at a larger scale and are viewed as an alternative to the other two approaches. The wide application of unmanned aircraft systems as platforms for thermal, hyperspectral and multispectral sensors have further improved remote sensing technologies as a method to detect water stress.

Within the sphere of remote sensing methods, there are two specific methods for detecting water stress: Infrared thermometry and spectral vegetation indices. Canopy temperature has long been recognized as an indicator for crop water stress (Jackson et al., 1981; Idso et al., 1981; Jackson et al., 1988). If the crops have not been provided with enough water, stomata will close and transpiration rate will be decreased. Since transpiration functions as a cooling mechanism for the plant, once it has been decreased, the canopy temperature will increase. As water stress can damage crops, successful detection of water stress is helpful for irrigation scheduling and other management practices. To quantify crop's water stress level, researchers have developed a Crop Water Stress Index (CWSI) (Jackson et al., 1981; Idso et al., 1981; Jackson et al., 1988) which takes canopy temperature and ambient meteorological conditions (net radiation, vapor pressure deficit and wind speed etc.) into consideration. Recently, Berni et al. (2009a) applied models based on canopy temperature estimated from high resolution airborne imagery to calculate tree canopy conductance and CWSI.

Due to the ability to detect physiological changes such as photosynthetic pigment changes or non-stomatal reductions of photosynthesis under water stress conditions, spectral vegetation indices such as Photochemical Reflectance Index (PRI), Red-edge Ratio (REI), Green Red Vegetation Index (GRVI) and the ratio of Transformed Chlorophyll in Reflectance Index (TCARI) to Optimized Soil-Adjusted Vegetation Index (OSAVI) can also be used as plant water stress indicators (Suárez et al., 2008; Baluja et al., 2012; Ballester et al., 2019).

CWSI and the above spectral indices were used as indicators of crop water stress, but none of them have taken solar radiation and evapotranspiration into consideration, which are the driving factor for the stomatal opening and a direct indicator of crop water status. The Bowen Ratio is the ratio

of sensible heat flux to latent heat flux and it takes the above two factors (solar radiation and evapotranspiration) into consideration, which implies that it can potentially be a better indicator of crop water status.

Generally speaking, the research gaps are that current uncooled thermal camera calibration methods are complicated and difficult to conduct and few of them have applied both non-uniformity and radiometric calibrations to in-field measurements; the existing energy balance ET models have been designed for the coarse resolution satellite imagery and there is a lack of appropriate models for high resolution thermal imagery from UAS; and current water stress indicators (CWSI, PRI and TCARI/OSAVI) have not taken solar radiation and crops ET into consideration. In order to address these gaps, we propose to (1) develop a methodology to calibrate uncooled thermal infrared cameras mounted on UAS to improve their accuracy when operating in the field, (2) adapt a two-source energy balance model designed to estimate evapotranspiration from vegetation using satellite imagery for use with high-resolution thermal imagery from UAS, and (3) evaluate the performance of the Bowen Ratio as an indicator of crop water stress relative to other existing methods.

1.1 Hypotheses and Objectives

The goal of this research is to build a tool which takes canopy temperature and other auxiliary data as inputs to estimate instantaneous water status of crops, which farmers or researchers can use for improved management of water resources and genotypic selection in breeding. To address this goal, four main hypotheses are proposed for this research project:

- Hypothesis 1: Calibration and atmospheric correction of uncooled thermal infrared cameras will increase the accuracy and decrease the variability in canopy temperature measurements from UAS platforms as compared to uncalibrated and uncorrected imagery.
- Hypothesis 2: High resolution thermal infrared and RGB imagery from a thermal camera system, mounted on a UAS can distinguish between soil and plants, thus increasing the accuracy of estimated ET from agricultural crops as compared to coarser resolution satellite imagery.

- Hypothesis 3: Bowen ratio can be used as an alternative crop water stress indicator to other spectral or temperature-derived indicators of water deficit stress.
- Hypothesis 4: UAS derived vegetation indices from multispectral and thermal cameras assessed on the plot level can be beneficial for genotypic selection in breeding.

In order to test the hypotheses above, the following objectives will be completed.

1. Conduct indoor thermal camera calibration using water targets and compare calibrated and uncalibrated temperature measurements to quantify how the calibration improves the temperature measurements accuracy of the camera.
2. Conduct atmospheric correction of the uncooled thermal camera by deploying water targets in the field during flight operations to reduce atmospheric effects on temperature measurements.
3. Customize the TSEB model to adapt it for high resolution thermal imagery from UAS for estimating evapotranspiration from field plots and evaluate accuracy against ground reference datasets.
4. Collect ground reference data of radiant temperature from multiple ground targets, and leaf porometry measurements from locations within the crop canopy.
5. Build mosaic imagery for each thermal camera flight using ground control points using (a) Pix4Dmapper software (Pix4D S.A., Switzerland).
6. Produce maps of calibrated and atmospherically corrected canopy temperature for each flight date.
7. Extract targeted plots from mosaics and calculated mean and standard deviation of canopy temperature, latent heat and ET by plot.
8. Evaluate canopy temperature, latent heat and ET with observed differences in phenotypic traits between experimental plots and with time during the growing season.
9. Calculate OSAVI, REI, GRVI, CWSI and Bowen Ratio by using spectral information and infrared thermometry information and test how these indices change with stomatal conductance and each other.

1.2 Thesis Format

The thesis is divided into five chapters. The first chapter reviews background knowledge of thermal remote sensing and crop water status monitoring in current literature then identifies current research gaps and poses hypotheses and identifies specific objectives required to address these hypotheses. Chapter 2 details the methods for improving small uncooled thermal camera measurement accuracy by using both laboratory and in-field calibration methods. A manuscript related to Chapter 2 has been published. In Chapter 3, a latent heat flux calculation algorithm for high resolution thermal imagery is developed and tested against reference data calculated from stomatal conductance and Penman-Monteith equations. A publication related to Chapter 3 is ready for submission. In Chapter 4, the Bowen ratio has been proposed as a water deficit stress indicator. Its performance is tested by some well-known indicators including CWSI, stomatal conductance, and SMI. Also, the correlation between Bowen ratio and vegetation indices like OSAVI, GRVI and REI will be investigated. Chapter 4 also demonstrates a method for plot level traits analysis in a field, which will be beneficial for genotypic selection in breeding. Chapter 5 summarizes the findings and presents overall conclusions based on the research presented in this dissertation and also provides a future work plan.

2. PIXEL-BASED CALIBRATION AND ATMOSPHERIC CORRECTION OF A UAS-MOUNTED THERMAL CAMERA FOR LAND SURFACE TEMPERATURE MEASUREMENTS

Acknowledgment: This chapter is copyright 2021 by the American Society of Agricultural and Biological Engineers and it has been included with the permission of ASABE.

Abstract

Thermal imagery can be used to provide insight into the water stress status and evapotranspiration demand of crops but satellite-based sensors are generally too coarse spatially and too infrequent temporally to provide information of use for the management of specific fields. Thermal cameras mounted to small unmanned aircraft systems (UAS) have the potential to provide canopy temperature information at high enough spatial and temporal resolutions to be used for crop management; however, without appropriate camera corrections, the measurements biases of these uncooled thermal cameras can be larger than ±5°C. Such uncertainty can render such camera measurements useless. In this research, a pixel-based (non-uniformity) calibration algorithm and an atmospheric correction method based on in-field approximate blackbody sources (water targets) are developed for a thermal camera. The objective is to improve the temperature measurement accuracy of the thermal camera on various land surfaces including soil and vegetation. With sufficient accuracy, temperature measurements can be used for the estimation of latent heat flux of field crops in the future. The thermal camera was first calibrated in a laboratory setting where the camera and environmental conditions were controlled. The results indicate that in the range between 10°C and 45°C, the calibrated temperatures are accurate with an average bias of 1.76°C and have a high linear correlation with reference temperatures (water target temperatures) (R^2 > 0.99). Variability of measurements is also better constrained. In-field atmospheric correction is also important to obtaining high accuracy thermal imagery. By applying both pixel-based calibration and atmospheric corrections, the root mean square error (RMSE) of validation targets from two dates in 2017 is reduced from 4.56°C and 6.36°C before calibration to 1.32°C and 1.24°C after calibration. The calibration process also increases the range of temperatures in the imagery, which enhances contrast and may help with identification of tie-points and stitching of images together to form whole field mosaics.

2.1 Introduction

Thermography is a non-invasive, non-contact, and non-destructive technique used to determine the thermal properties and features of any object of interest and therefore has potential use in agriculture (Ishimwe et al., 2014). It has been successfully applied to, but not limited to, nursery and greenhouse monitoring (Kranner et al., 2010; Eitel et al., 2010), irrigation scheduling (Osroosh et al., 2015; Gowda et al., 2008; Barbagallo et al., 2009), plant disease detection (Mahlein et al., 2012), crop yield estimation (Smith et al., 1985; Stajnko et al., 2004), soil texture mapping (Wang et al., 2012), residue cover and tillage mapping (Kozak et al., 2007), soil salinity detection, evaluating maturity of crops and bruise detection in fruits and vegetables (Khanal et al., 2017; Scotford and Miller, 2004; Pen et al., 1985), and estimation of transpiration and stomatal conductance (Hoffmann et al., 2016; Ortega-Farías et al., 2016; Sepúlveda-Reyes et al., 2016; Berni et al., 2009a).

Before the advent of small unmanned aircraft system (UAS), satellite thermal sensors or cameras were the most com-mon methods used to obtain thermal feature information of ground objects. However, their repeat times and spatial resolutions are not suitable for many applications in agricultural research that require sub-meter resolution and multiple observations at specific times of day (Cherkauer et al., 2005).

Currently, thermal cameras can be classified into two categories: uncooled and cooled. Uncooled thermal cameras are used on UAS because of their small size, light weight, and affordable price. Due to the lack of cooling components, they have slower image capture rates and are less sensitive than cooled cameras to differences in temperature within their field of view. Ribeiro-Gomes et al. (2017) and Budzier and Gerlach (2015) identified five types of calibration that should be conducted for a typical uncooled thermal camera: non-uniformity correction, defective pixel correction, shutter correction, radiometric calibration, and temperature dependence correction. For modern thermal cameras, defective pixel correction and shutter correction are generally integrated into the firmware included in the system. Temperature dependence correction can be reduced by bringing cameras to equilibrium with the local environment before data collection and operating them at a constant environmental temperature. That leaves users to address non-uniformity correction and radiometric calibration.

Many studies have focused on laboratory calibration of uncooled thermal cameras (e.g., Perry and Dereniak, 1993; Orżanowski, 2016; Sosnowski et al., 2010; Nugent et al., 2013; Ribeiro-Gomes et al., 2017). For example, Perry and Dereniak (1993) proposed a two-point correction method in which two separate calibration temperatures were used to remove additive and multiplicative nonuniformities from the sensor output. They found that the residual spatial noise was reduced from above 0.2°C to below 0.05°C compared to using only one calibration temperature; however, they assumed that the camera response to a wide range of temperatures would be linear, which cannot be assumed for uncooled cameras (Ribeiro-Gomes et al., 2017). Nugent et al. (2013) described a method for stabilizing a thermal camera's response based on the difference between the camera's response at a measured temperature and at a reference temperature. They reported a maximum error of 0.75°C after calibration for a thermal camera with initial uncertainty of ±2°C. More recently, Ribeiro-Gomes et al. (2017) developed a calibration algorithm based on artificial neural networks for an uncooled thermal camera in a laboratory. Inputs for the algorithm include sensor temperature and digital response of the microbolometer. They reported that the measurement bias was reduced from 3.55°C with the original camera configuration to 1.37°C after calibration.

For field calibration, Lillesand et al. (2014) summarized the two most commonly used radiometric calibration methods for thermal infrared sensors: internal blackbody source referencing and air-to-ground calibration. The first method takes the form of two temperature-controlled ("hot" and "cold") blackbody radiation sources positioned near the camera in a place where they are viewed by the sensor periodically during flight. By comparing the signal recorded from the Earth's surface to the radiation from these two precisely controlled blackbody calibration sources, a mathematical relationship can be established to calibrate the sensor. This method does not account for atmospheric effects; however, because the blackbodies are positioned near the camera, there is little impact from atmospheric conditions. The other radiometric calibration method, air-to-ground calibration, can be used to correct for atmospheric effects. Observations are typically made at points where temperature is assumed to be constant. The corresponding scanner output value is then determined for each point of the ground-based surface temperature measurements. A calibration curve is then constructed relating the scanned output values to the corresponding ground-based radiant temperature.

Young et al. (2002) developed a method for atmospheric compensation of thermal hyperspectral data. They analyzed coarse-resolution satellite imagery from a hyperspectral camera, and the emissivity of all ground features was assumed to be unity. Spectral radiance emitted from the ground was approximated at a fixed reference spectral channel (a particular wavelength) where the maximum value of brightness temperature occurred. They demonstrated the ability to effect an atmospheric compensation of thermal hyperspectral data using only the data collection itself.

Additionally, radiative transfer models such as MODerate resolution atmospheric TRANsmission (MODTRAN) are also used to compensate for atmospheric effects (Berni et al., 2009b; Kay et al., 2005; Handcock et al., 2006).

Laboratory calibrations and atmospheric corrections have been demonstrated previously in the literature, but so far there have been few applications of these methods to UAS-mounted thermal infrared cameras. The non-uniformity correction methods developed previously have used only two calibration temperatures and assumed that the response from the infrared focal plane array to a wide range of temperatures is linear, which may be problematic for the variety of low-cost uncooled thermal cameras currently being employed.

In this research, we built our own in-field approximate blackbody sources (water targets), which are affordable and easy to make, and used them to develop a straightforward method for performing laboratory and field calibrations of thermal infrared cameras. In the laboratory calibration, 22 different calibration temperatures (from 0°C to 50°C) were applied to develop pixel-based calibration equations. The lab-calibrated camera was then used for field operations, and methods are presented to calibrate and correct selected raw images for atmospheric effects. Finally, an assessment of the accuracy of the calibrated surface temperatures captured during a series of UAS flights is presented.

The objective of this research is to demonstrate a method to improve the measurement accuracy and precision of a low-cost, uncooled thermal camera mounted on a UAS platform for various land surfaces including soil and vegetation.

2.2 Methods

A FLIR Vue Pro R camera (FLIR Systems, Wilsonville, Ore.) was used for all data collection. This camera has a pixel resolution of 640 × 512 and a focal length of 19 mm with a field of view 32° × 26°. The camera is sensitive to spectral wavelengths from 7.5 to 13.5 μm, with a manufacturer-reported measurement accuracy of ±5°C or 5% of reading in its operating temperature range (-20°C to +50°C).

The camera has a factory radiometric calibration that allows the image digital numbers to be converted to temperature. As with most sensors, calibration of the specific system under conditions similar to how it will be operated is critical for obtaining the most accurate data. For the FLIR camera, we conducted calibration experiments in the laboratory to quantify the absolute accuracy and the noise equivalent temperature difference (NETD) and then used in-field water bodies to conduct in-flight atmospheric corrections. Detailed methods for these calibration processes are provided in the following sections.

The radiance from each calibration target that arrives at the sensor can be described by the following equation (Equation 2.1) (Barsi et al., 2003; Young et al., 2002):

$$L(\lambda) = \varepsilon(\lambda)B_\lambda(T)\tau(\lambda) + L_u(\lambda) + [1 - \varepsilon(\lambda)]L_d(\lambda)\tau(\lambda) \quad (2.1)$$

Where $L(\lambda)$ = detected spectral radiance at wavelength λ (m) (W m^{-2} sr^{-1} μm^{-1}), $\varepsilon(\lambda)$ = surface emissivity. $\tau(\lambda)$ = atmospheric transmittance for the path between the surface and the sensor, $L_u(\lambda)$ = upwelling atmospheric radiance for the same path (W m^{-2} sr^{-1} μm^{-1}), $L_d(\lambda)$ = hemispherical downwelling radiance from the entire sky (W m^{-2} sr^{-1} μm^{-1}), and $B_\lambda(T)$ = spectral radiance emitted from a blackbody with the same temperature as the target (W m^{-2} sr^{-1} μm^{-1}).

The spectral radiance emitted by an object is estimated using the Planck function (Equation 2.2):

$$B_\lambda(T) = \frac{c_1\lambda^{-5}}{\pi\left(e^{\frac{c_2}{\lambda T}} - 1\right)} \quad (2.2)$$

where T is temperature (K), and the constants are defined as $c_1 = 3.74 \times 10^{-16}$ W m^2 and $c_2 = 1.45 \times 10^{-2}$ mK. When conducting atmospheric corrections, the calibration target temperature is assumed to be equal to the bulk water temperature because the target is well mixed.

At-sensor radiance recorded by the thermal camera is calibrated to the radiance emitted by the ground calibration targets, as calculated from Equation 2.2. For the calibration process, equation 2.1 can be simplified by not considering the downwelling radiance from the entire sky (Equation 2.3) (Young et al., 2002):

$$L(\lambda) = \varepsilon(\lambda) B_\lambda(T) \tau(\lambda) + L_u(\lambda) \tag{2.3}$$

There are now only two unknowns left: $\tau(\lambda)$ the atmospheric transmittance and $L_u(\lambda)$ the upwelling atmospheric radiance. Equation 2.3 is also now simplified into a linear function. In this research, we use ground reference temperature measurements and can directly derive the emitted radiance and emissivity of the ground targets (water, paint, fabric, etc.). Because the thermal camera is sensitive to a wide spectral range, from 7.5 to 13.5 μm, the integration of emitted spectral radiance over the full range was used for the purpose of calibration and temperature estimation. In practice, for the range of normal terrestrial temperatures, all bodies can be treated as gray bodies so that the emissivity of the targets is considered constant across the sensitive spectral range of the thermal camera.

To conduct both the laboratory-based and in-field calibrations of the thermal camera, we constructed three water targets (Figure 2.1). Each water target consists of a reservoir containing about 30 L of water shaded from direct sunlight. A pump pulls water from the reservoir and pushes it out into the middle of a circular pan. The pan is made of vinyl with a diameter of 43 cm to make sure it is visible in the thermal imagery. The depth of the water surface on top of the pan is about 5 cm, and the height of the water target is 60 cm. Water pumped into the pan flows from the center to the edge, where it falls back into the reservoir. By continually moving the water visible to the UAS sensor, the water target minimizes the formation of a cooler skin layer on the surface of the water. This process means that the water surface is constantly being refreshed, so emissions in the thermal infrared reflect the bulk temperature of the water rather than the cooler skin temperature that forms from evaporation (Kay et al., 2005). Because we use tap water for the targets, the thermal emissivity of water is assumed to be 0.98 (Campbell and Norman, 2012).

One resistance temperature detector (RTD) (Omega Engineering, Stamford, Conn.) with an accuracy of ±0.2°C was deployed in the reservoir of each target and used to continuously measure

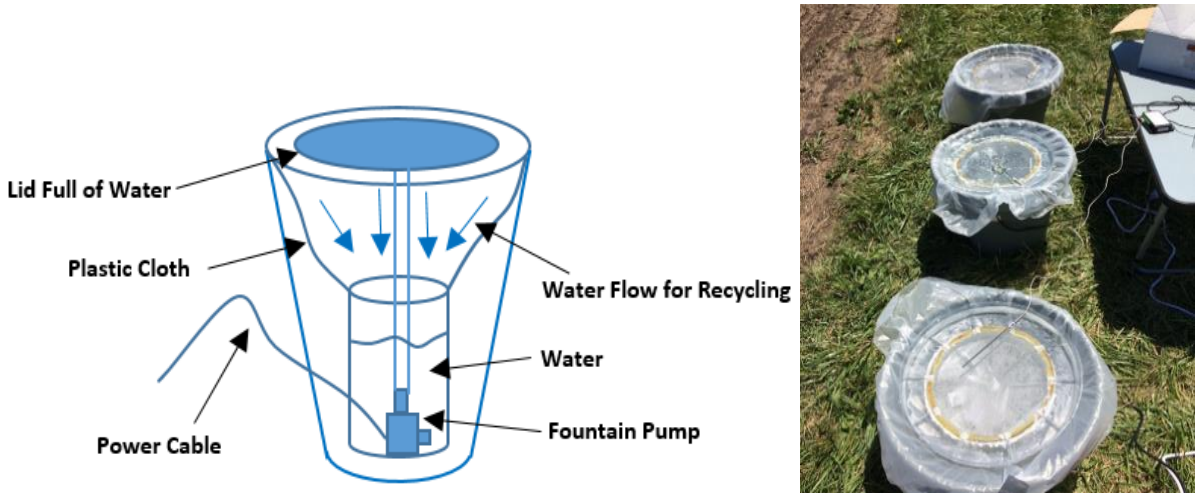

Figure 2.1. (left) Schematic of a water target and (right) photo of water targets deployed in the field during flight operations.

the bulk water temperature during calibration operations. The targets provide a range of temperatures for calibration, with the temperatures of the warm and cool water selected to ensure that the temperatures of all objects in the field of view fall within this range. This means that we only need to interpolate the temperature information of unknown pixels, instead of extrapolating it, which makes the calibration more accurate.

2.2.1 Laboratory-based calibration

The thermal camera and all other temperature sensors used during field operations were first calibrated in a laboratory setting where the camera and environmental conditions could be controlled. The temperature of the laboratory during calibrations was 25°C. The NETD of the camera was then quantified.

The camera is composed of 640 × 512 detectors. Because each pixel value reflects the radiance it detects, we correlated the pixel values (digital numbers) with the emitted radiance from a water target such that we optimized the measurements of the thermal camera. Absolute accuracy was

calibrated against a high-accuracy National Institute of Standards and Technology (NIST)-certified temperature sensor across a range of water temperatures.

Laboratory calibration was conducted using a single water target to provide a well-mixed water body and an effective approximate blackbody. The thermal camera was allowed to warm up by turning it on about 20 min before calibration, which helped to stabilize the sensor temperature and minimize its impact on calibration. The range of water temperatures for the calibration process was varied from about 0°C to 50°C to ensure that the range of naturally occurring temperatures in the field during a growing season was captured. The water temperature was changed by an interval of approximately 5°C for each calibration measurement. The water temperature was first decreased from 50°C to 0°C, and then the calibration process was repeated by increasing the water temperature over the same range. Measurements were conducted in both directions to compensate for potential hysteretic performance of the various sensors (Doebelin and Manik, 1996). The time interval between each measurement was about 30 min, and the entire experiment took about 10 h to complete.

A NIST-certified traceable temperature sensor was used as a reference, and special attention was paid to making sure that recordings from the sensors were taken only when the water temperature had reached equilibrium. The thermal camera was mounted to a support stand using a small three-prong dual-adjustable clamp. It was positioned 10 cm above the water target with well-mixed water surface (Figure 2.2). At this distance, the full frame of the camera captured an approximately 5.7 cm × 4.6 cm rectangular area. This ensured that the full image scene focused only on the well-mixed water surface, and the temperature within this small area was assumed to be uniform.

Because each detector responds individually to a given temperature level, calibration equations were developed for each detector. Pixel values at different temperatures were calibrated by computing a least-squares linear regression relationship, and the intercepts and slopes were stored in variables that can be used for calibrating any raw image from this camera in the future. The linear relationships between raw digital numbers (DN) and radiance (RI) of the water target at different temperatures were established in the form (Equation 2.4):

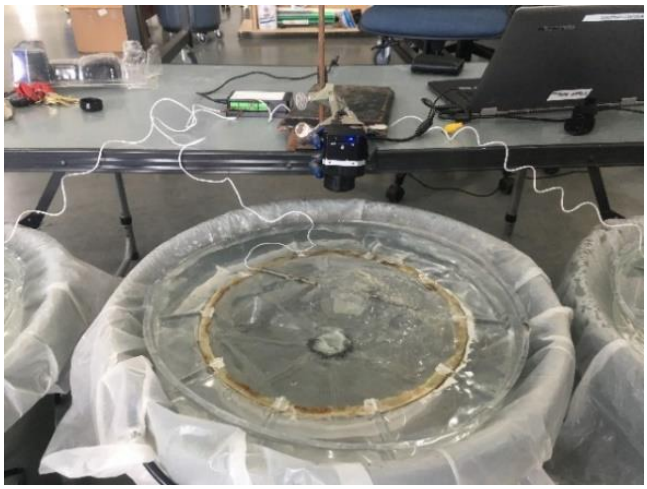

Figure 2.2. Thermal camera positioned 10 cm above the water surface for laboratory calibration.

$$\mathrm{DN} = \mathrm{Slope} \times \mathrm{RI} + \mathrm{Intercept} \tag{2.4}$$

The three RTDs and three handheld infrared thermometers (TG54 spot IR thermometer, FLIR Systems, Wilsonville, Ore.) were also calibrated during this process for use in collecting ground reference data during field operations. Measurements from the thermal camera and the infrared thermometers were synchronized with those of the traceable sensor, and the time of measurement was also recorded to identify data from the RTDs because they collected data continuously. The RTDs and NIST-certified temperature probes were placed near the center of the target without making physical contact with each other or breaking the water surface within the field of view of the camera. This allowed all temperature sensors to be calibrated simultaneously.

The NETD, which measures the thermal camera's signal-to-noise ratio, or in other words its ability to distinguish between temperatures, was measured by looking at the temperature variability across the image when the field of view was locked on a constant, uniform temperature. This is a critical measure of the sensitivity of a thermal infrared camera, so we used the following method, based in part on the FLIR manual (FLIR, 2018a), to measure it.

Three water targets were set up using warm (41.06°C), intermediate (18.23°) and cool (0.18°C) water, and the position of the camera remained the same as mentioned above. The water temperatures were measured by the RTDs submerged in the bulk water. Sixty-four frames of the warm and cool targets were captured at 1 s intervals; these were used to calculate the average

pixel-level response at both temperatures. Next, 128 sequential image frames were collected for the intermediate temperature target at 1 s intervals; these were used to calculate the standard deviation (temporal noise) of each pixel value. During the measurement periods, the standard deviations of the water temperature for the three targets (warm, intermediate, and cool) were 0.06°C, 0.02°C, and 0.01°C, respectively, indicating that the bulk water temperatures did not change significantly during the short measurement periods.

The cool response array was subtracted from the warm response array and then divided by the difference of their average bulk water temperatures. This gave us a responsivity array with units of counts per degree. Dividing the temporal noise array by the responsivity array produced an NETD array with units of Kelvin. Taking the average of all the pixels in this array (neglecting bad pixels) produced the NETD of the camera (FLIR, 2018a).

In this research, temperature measurements of the targets in thermal imagery are reported as (Equation 2.5) (Doebelin and Manik, 1996):

$$\text{Temperature} = T_{avg} \pm 3 \times s_{T_{meas}} \tag{2.5}$$

where T_{avg} (°C) is the mean pixel measurements of a target in a thermal image, and s_{Tmeas} is the standard deviation of these pixel measurements. In this way, the temperature measurement of the targets falls within three standard deviations of the mean 99.7% of the time.

2.2.2 Compensation for atmospheric effects

To compensate for atmospheric effects during flight operations, and to further optimize the outputs from the thermal camera, additional radiometric calibration was conducted. The aim of this process was to reduce the effects of thermal radiation emitted by the atmosphere between the camera and the objects on the ground by correcting the images to objects of known temperature on the ground.

The field study was conducted in 2017 and 2020 at the Purdue Agronomy Center for Research and Education (ACRE) (West Lafayette, Ind.), which is located about 8 km (5 mi) northwest of Purdue University's main campus (Figure 2.3). All ground targets including the water targets were deployed on the grass lane or bare soil near the agricultural fields targeted during flight operations. Weather data were collected from the ACRE weather station (centered on 40° 28′ 30.6″ N, 86° 59′

31.6″ W). Flights for this analysis were conducted on three days in 2017 and 2020, and the weather information for each date is summarized in Table 2.1.

Table 2.1. Weather parameters for experimental days.

Date and Time	Air Temperature (°C)	Wind Speed (m s^{-1})	Relative Humidity (%)
25 Aug. 2017 (16:30)	22.6	2.3	44.5
28 Sept. 2017 (17:00)	22.1	2.7	43.2
6 Aug. 2020 (17:30)	24.2	1.2	51.0

When the camera was used as part of flight operations, it was mounted on the underside of a rotary-wing DJI S1000 in 2017 and DJI M200 in 2020 (DJI, Shenzhen, China) and focused directly at the ground. The camera was fixed, not on a gimbal. The UAS altitude was set to 70 m above the field surface to achieve a ground resolution of about 7.17 cm $pixel^{-1}$. The camera was turned on about 20 minutes before each flight and triggered to take pictures every second during the flight. The camera was allowed to acclimate to the local air temperature and kept out of direct sunlight during the 20 minutes warmup period to minimize camera temperature drift during data collection. All targets (calibration and validation targets) were placed where they would be in the field of view of the camera during flight operations. In 2017, the calibration targets (including vegetative surface, spectral targets, and ground control points) and the water targets were visible in the same image. In 2020, the calibration targets (including bare soil, grass, water targets, ground control points, and spectral targets) were deployed away from each other, and only one validation target could be seen in any individual image. These individual images were taken within 15 minutes of the images of ground calibration targets.

Water targets were visible multiple times during every flight. For instance, all three water targets appeared in three images on 25 August 2017 and in five images on 28 September 2017. In 2017, only one set of three water temperatures was used, while in 2020, the temperatures of the three water targets were changed twice during flight operations, resulting in nine different temperatures. All water target temperatures were continuously monitored with submerged RTDs.

Only the images with the targets closest to the image center were used for atmospheric correction to reduce the effect of vignetting on temperature accuracy. We refer to these images as “seed images” in this article.

Ground reference data were collected using the handheld infrared thermometers calibrated as part of the laboratory-based calibration process. The handheld infrared thermometers, with an accuracy of ±0.2°C after calibration, were used to measure at least four points within each ground feature to obtain an average radiative temperature. When taking a measurement, the thermometer was pointed directly down to avoid interference from direct solar radiation. The height of the handheld thermometer above the target was used to confirm that the spot measurement size fell completely within the desired target. Each handheld thermometer was shaded as much as possible during data collection to minimize the effect of solar heating on the thermometer measurements. The time of each handheld thermometer measurement was recorded, and measurements were taken before and after flight operations to check for significant changes in ground reference target temperatures. Ground reference values are represented by means ±3 times the standard deviations based on the laboratory calibration; however, when used to calculate bias, only the mean of the reference measurements is used.

Selected ground reference features must be visible in the thermal imagery, must be generally uniform in composition, and must not change temperature significantly during each day’s flight operations. Temperature information for each ground reference target was extracted from the calibrated thermal imagery and was compared against the information from the handheld infrared thermometers. This provided an independent evaluation of the calibrated image temperatures.

The raw images were first calibrated by applying the slope and intercept values, which were derived from the pixel-based calibration. The atmospheric correction relationships developed from the seed image using the detected and emitted radiance of the water targets were then applied to produce images in which the pixels represented the calibrated emitted radiance from the ground surface with minimal atmospheric effects. After this, radiance was converted to temperature for all images based on the emissivity of the surface material, and temperatures from additional ground reference targets were extracted from the images for evaluation purposes.

Evaluation of the calibration methods was conducted by comparing the calibrated image temperatures with the handheld infrared thermometer measurements of ground reference features including ground control points, vegetative surface, bare soil, water targets and spectral calibration targets. All targets occupied four to nine pixels in the images; to be consistent, the four most central pixels were used to derive the temperatures from all imagery.

Bulk temperatures measured from the water targets at other times during the flight, not seed images, were used to evaluate the thermal drift of the camera during flight operations. The correction equation for each flight was then applied to all images taken during that flight. The entire calibration and validation process is summarized in Figure 2.4.

2.2.3 Laboratory based calibration results

Figure 2.5 shows the slope and intercept values from the linear calibration equations developed for each pixel of the thermal camera. Slope values were highest at the right and left edges of the camera's field of view (Figure 2.5a), while intercept values were highest in the middle (Figure 2.5b). This phenomenon is due to the vignetting effect of the camera lens on the resulting thermal images. The variation between thermal camera pixels was small, but the calibrated accuracy was best in the middle of the temperature range (Figure 2.6 and Table 2.2). The error bounds from the calibration process indicate that most camera measurements fell within the 99.7% uncertainty range (±2.3°C), with exceptions arising at the highest and lowest temperatures used for calibration.

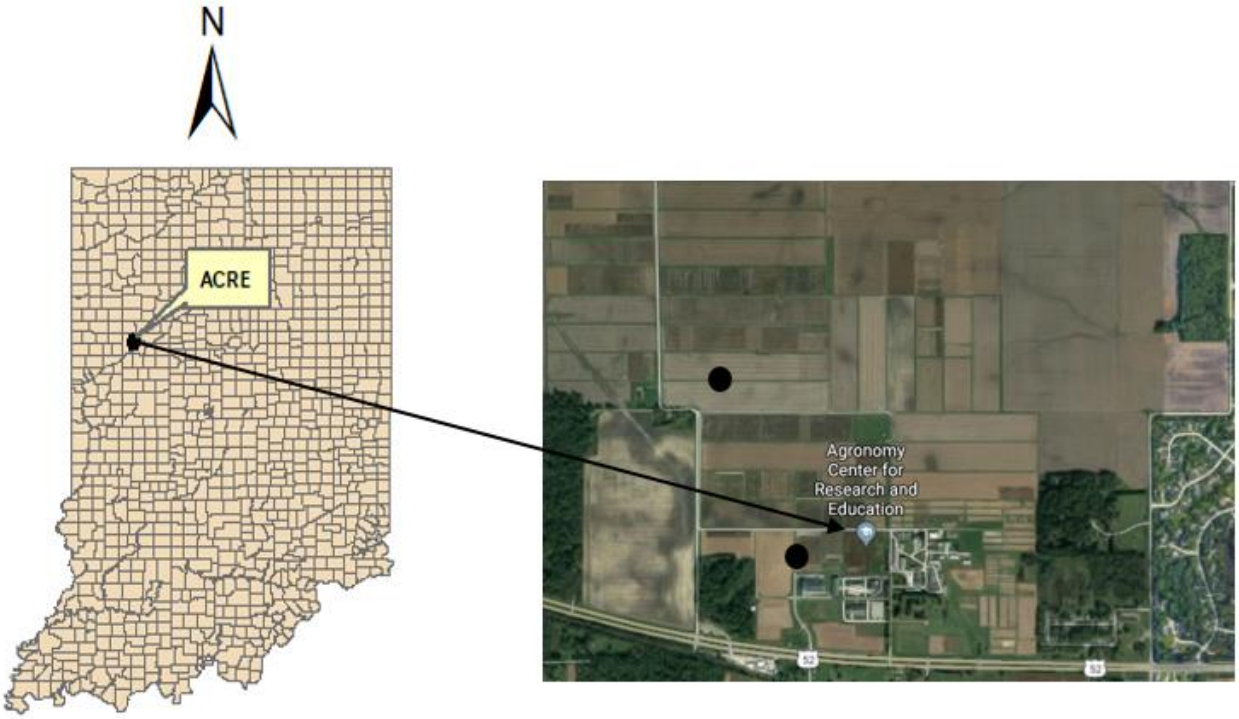

Figure 2.3. Location of the Purdue Agronomy Center for Research and Education (ACRE) and the 2017 and 2020 field sites. In the right image, the upper and lower dots indicate the 2017 and 2020 sites, respectively (image acquired from Google Maps).

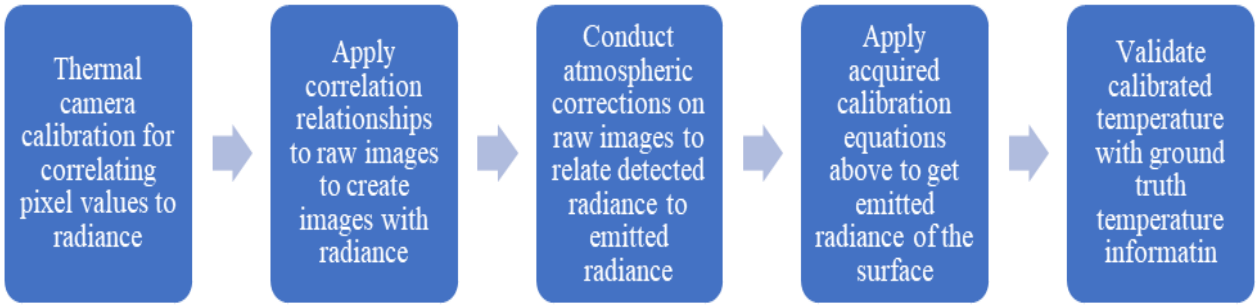

Figure 2.4. Flowchart of thermal imagery calibration and validation.

2.3 Results

Figure 2.7 and table 2.2 illustrate how well the algorithm calibrated the raw images. The calibration process reduced the bias and also reduced the variance of the measured temperatures (Figure 2.7), especially in the range of temperatures that are dominant for agricultural applications. For the examples shown, the temperature bias decreased by as much as 5.32°C for the water target with a

bulk temperature of 35.80°C, while the standard deviation decreased by 0.28°C for the water target with a bulk temperature of 28.47°C.

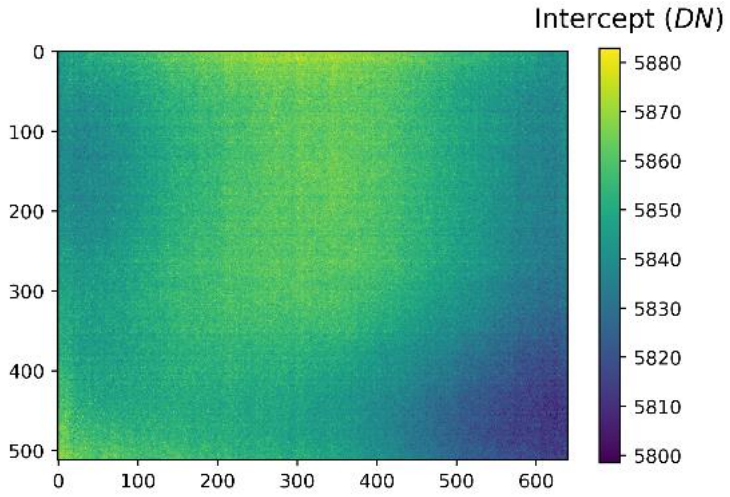

(a)

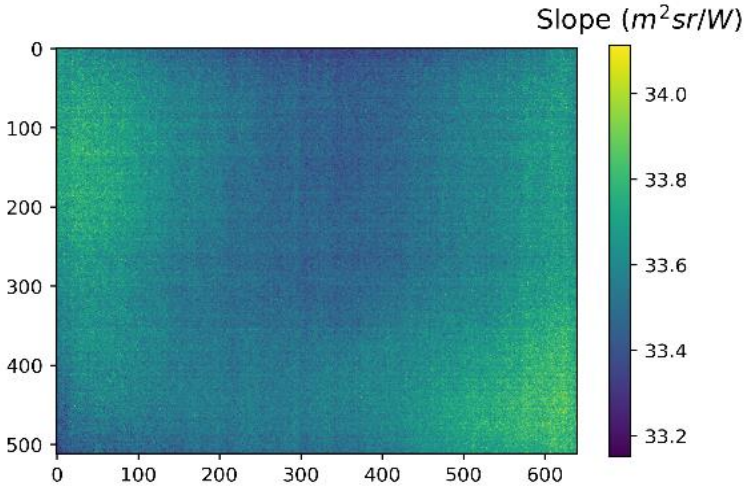

(b)

Figure 2.5. (a) Slope and (b) intercept values from the linear calibration equations developed for each thermal camera pixel. Images represent the entire field of view of the camera.

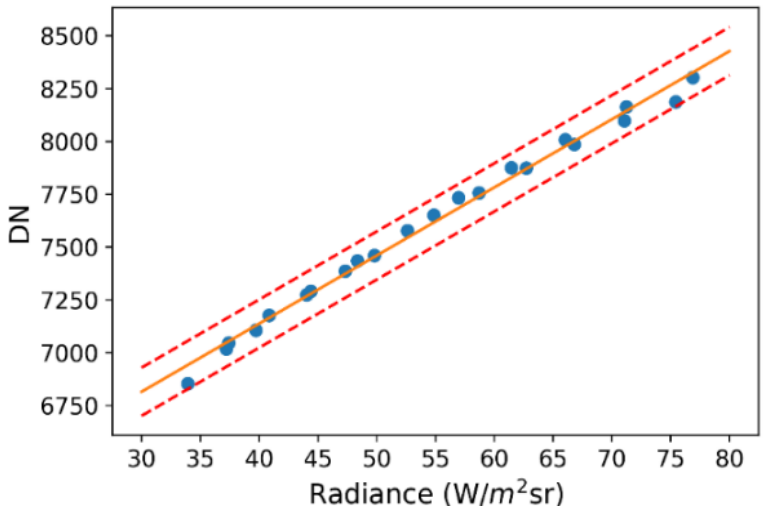

Figure 2.6. Calibration relationship between the camera digital number (DN) and the radiance of the water target across the range of bulk water temperatures used for calibration. The solid line indicates the average calibration equation for all pixels, while the dashed lines indicate 99.7% error bounds. Data points are the mean DN value of the camera image at each temperature.

Table 2.2 also shows that, without calibration, the measurements from the thermal camera tend to overestimate the reference temperatures, while the measurements underestimate the reference temperatures after calibration. In addition, the calibration bias is worse than the uncalibrated bias at the highest and lowest temperatures used for calibration. This is especially true for the cold water temperatures, as the calibrated bias is larger than or similar to the uncalibrated bias for all measurements less than 10°C. The most significant bias is for the reference temperature of 0.71°C, where the calibrated bias is 5.38°C, while there is no bias for the uncalibrated temperature. The calibrated bias exceeds the uncalibrated bias at a reference temperature of 49.89°C, but not for any of the other high-temperature calibration points. One of the reasons for increased inaccuracy at extreme temperatures is that when the water temperature is significantly higher (49.89°C) or lower (0.71°C, 5.69°C, and 9.31°C) than the ambient temperature, the reflected thermal emissions from the background contribute a larger portion of the radiation detected by the thermal camera than that at intermediate temperatures (10°C to 45°C) (FLIR, 2018b). The root mean square error (RMSE) was reduced from 4.73°C to 2.74°C for the full temperature range and from 4.12°C to 1.70°C for the more limited intermediate temperature range (10°C to 45°C).

The NETD for the thermal camera used in this study was calculated to be 145.5 mK. This is higher than the 50 mK expected from the FLIR documentation. Because the NETD uncertainty can be

either positive or negative, the camera can only distinguish temperature differences greater than 0.291 K. To be more specific, if the temperature difference between objects in a thermal image is less than 0.291 K or 0.291°C, then we cannot with confidence conclude that their temperatures are different.

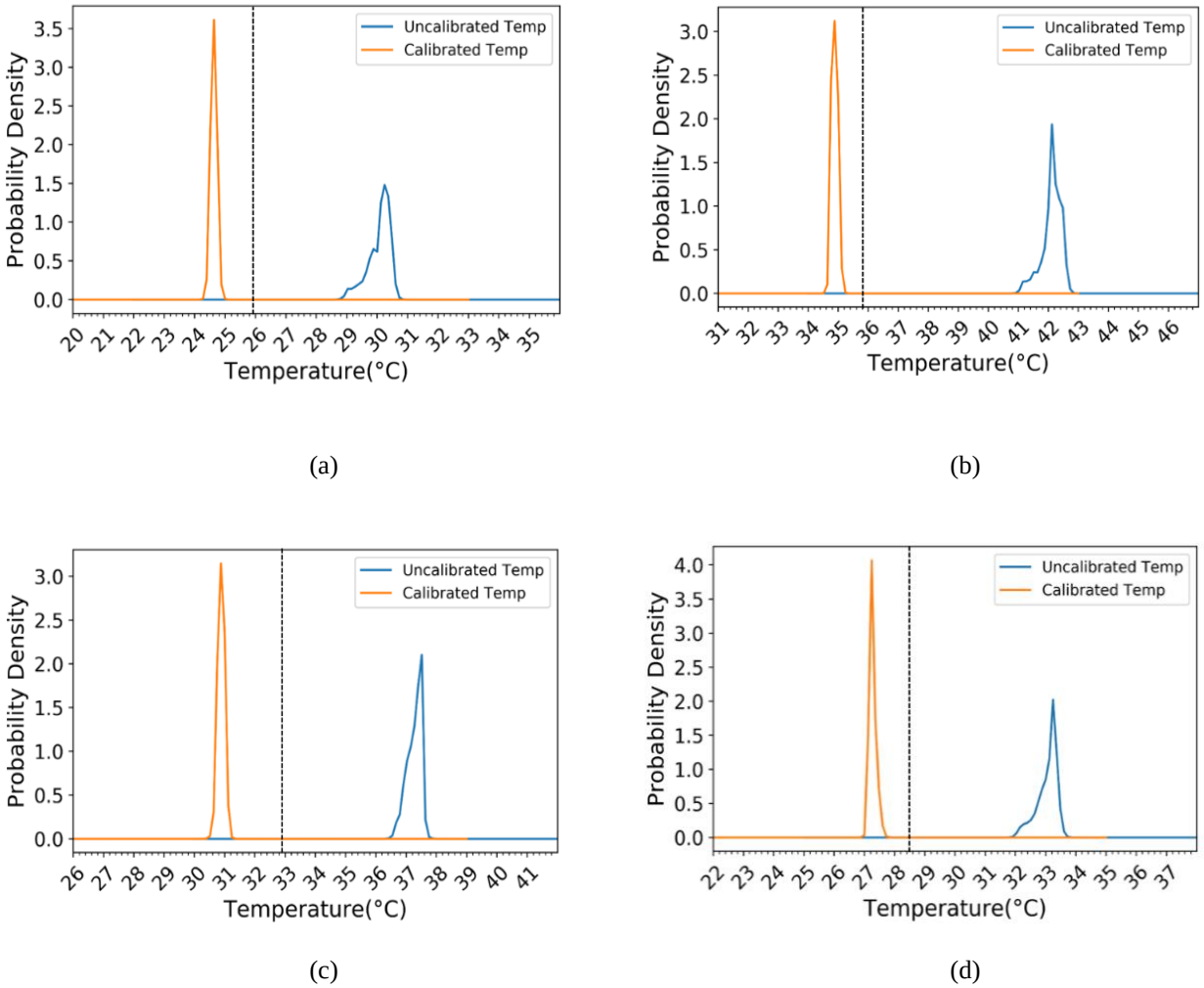

Figure 2.7. Temperature distributions for pixels of uncalibrated (blue) and calibrated (orange) thermal images over the water target blackbody with bulk temperatures of (a) 35.80°C, (b) 25.86°C, (c) 32.82°C and (d) 28.47°C. Each bulk temperature is represented by a black dashed line.

Table 2.2. Reference temperatures and mean temperatures extracted from imagery. Means include uncertainties, defined as ±3 standard deviations of all measurements collected for the same target. Means and uncertainties are presented for uncalibrated and calibrated images of the water target taken during the calibration process (temperatures are listed in chronological order).

Reference Temp. (T_{ref}, °C)	Uncalibrated Temp. (T_{uncal}, °C)	Calibrated Temp. (T_{cal}, °C)	Uncalibrated Bias (°C) ($T_{uncal} - T_{ref}$)	Calibrated Bias (°C) ($T_{cal} - T_{ref}$)
51.25	59.43 ±1.05	47.54 ±0.36	8.18 ±1.05	-3.71 ±0.36
45.84	53.76 ±1.06	43.61 ±0.36	7.92 ±1.06	-2.23 ±0.36
40.61	47.45 ±0.66	38.97 ±0.42	6.84 ±0.66	-1.64 ±0.42
35.80	42.11 ±1.00	34.81 ±0.30	6.31 ±1.00	-0.99 ±0.30
30.89	36.32 ±0.86	30.06 ±0.27	5.43 ±0.86	-0.83 ±0.27
25.86	30.06 ±1.11	24.64 ±0.31	4.20 ±1.11	-1.22 ±0.31
20.71	24.25 ±1.05	19.34 ±0.27	3.54 ±1.05	-1.37 ±0.27
15.64	18.44 ±1.05	13.80 ±0.30	2.80 ±1.05	-1.84 ±0.30
10.87	13.85 ±1.35	9.24 ±0.69	2.98 ±1.35	-1.63 ±0.69
6.00	8.50 ±1.35	3.73 ±0.61	2.50 ±1.35	-2.27 ±0.61
0.71	0.71 ±1.21	-4.67 ±0.43	0.00 ±1.21	-5.38 ±0.43
5.69	7.39 ±1.14	2.56 ±0.36	1.70 ±1.14	-3.13 ±0.36
9.31	10.96 ±1.01	6.30 ±0.90	1.65 ±1.01	-3.01 ±0.90
15.19	17.76 ±1.17	13.14 ±0.39	2.57 ±1.17	-2.05 ±0.39
19.40	22.28 ±0.95	17.49 ±0.77	2.88 ±0.95	-1.91 ±0.77
22.52	25.26 ±1.11	20.28 ±0.28	2.74 ±1.11	-2.24 ±0.28
28.47	33.05 ±1.00	27.26 ±0.34	4.58 ±1.00	-1.21 ±0.34
32.82	37.26 ±0.72	30.84 ±0.35	4.44 ±0.72	-1.98 ±0.35
37.16	42.06 ±0.84	34.77 ±0.18	4.90 ±0.84	-2.39 ±0.18
41.40	46.57 ±0.75	38.30 ±0.20	5.17 ±0.75	-3.10 ±0.20
45.66	51.15 ±0.85	41.73 ±0.21	5.49 ±0.85	-3.93 ±0.21
49.89	54.70 ±0.86	44.28 ±0.44	4.81 ±0.86	-5.61 ±0.44

2.3.1 Atmospheric effects compensation

The final process is to correct the thermal infrared images collected from the UAS platform for atmospheric effects. Flights on three dates (25 August 2017, 28 September 2017, and 6 August 2020) are used to demonstrate the method used to build atmospheric correction models using in-field water targets and validate those models versus supplemental ground reference data.

The emitted radiance and detected radiance of the water targets in 2017 are summarized in tables 2.3 and 2.4 and are used to derive linear atmospheric correction equations for the 25 August and 28 September flights. For both flights, the detected radiance of the water targets is lower than their emitted radiance, except for the cold target. This is because the temperature of the cold target was significantly lower than the measured air temperature, so it was more susceptible to atmospheric interference, which increased the emitted radiance collected at the sensor. For the warmer targets, the atmosphere attenuated their emitted radiance.

After applying both pixel-based calibration and atmospheric correction to the raw images (Figure 2.8a), radiance was converted to temperature based on the Planck function, and calibrated thermal images were generated (Figure 2.8b). Generally, calibration reduced the cooler vegetative surface temperature, while the warmer ground temperature was increased, thus the contrast of the images was enhanced (Figure 2.8c).

Table 2.5 shows that the bias between the ground reference temperatures and the temperatures extracted from the calibrated thermal imagery was reduced relative to the temperatures extracted from uncalibrated imagery. For the vegetative surface, the resulting change in detected temperature after calibration and correction for atmospheric effects (0.29°C) is smaller than the NETD of the camera, and therefore not significant. However, the change in temperature registered for the white calibration panel is larger than the measurement uncertainty, with the bias between the raw temperatures and those from the calibrated and atmospherically corrected images decreased by 1.36°C.

Table 2.3. Emitted radiance and sensor-detected radiance of water targets on 25 August 2017 (16:37:11).

Water Target	Temperature (°C)	Emitted Radiance (W m^{-2} sr^{-1})	Detected Radiance (W m^{-2} sr^{-1})
Cold	8.56	37.62	39.74
Intermediate	24.73	49.58	47.39
Hot	33.89	57.29	49.94

Table 2.4. Emitted and detected radiance of water targets on September 28, 2017 (17:10:21).

Water Target	Temperature (ºC)	Emitted Radiance (W m^{-2} sr^{-1})	At-Sensor Radiance (W m^{-2} sr^{-1})
Cold Target	1.05	32.76	39.54
Intermediate Target	22.70	47.96	46.61
Hot Target	34.93	58.20	56.60

The effectiveness of the atmospheric correction was further tested by applying the calibration equation for 25 August 2017 to subsequent images taken on the same day, in which at least one water target or ground reference target was visible (Tables 2.6 and 2.7). Because all images were taken within 2 min, the weather conditions were assumed to be stable during this period of time, and the same reference temperature measurement of each ground target was used for validation between images.

When applying the calibration equation to the water targets in subsequent images, the observed bias decreased to below 1.94°C for all cases. Meanwhile, the calibrated bias of the vegetative surface is less than 1.19°C, which is the same or less than that of the initial validation (Table 2.5). These results indicate that the atmospheric correction developed earlier can be applied to subsequent images to acquire accurate temperatures. The RMSE (Zhu et al., 2019) for all validation targets on 25 August 2017 was reduced from 4.56°C to 1.32°C after calibration.

Ground reference temperatures were collected for additional targets for the 28 September 2017 flight, resulting in a larger evaluation dataset (Tables 2.8 and 2.9). For this flight, the uncalibrated bias ranged from 1.41°C to greater than 3.00°C. After calibration and correction, the largest bias was 0.98°C for the black ground control point. However, measurement uncertainty increased after calibration for the vegetative surface measurements.

The atmospheric calibration was again evaluated by applying it to other images from the same day in which at least two of the ground targets or water targets were visible. When applying the atmospheric calibration equation to the water targets that appeared in images not used to seed the atmospheric correction equation, the bias decreased, with an average absolute calibrated bias of 1.87°C. Even with only 2 s between images, there was variation in the temperatures extracted from the thermal infrared images. There are multiple potential causes for these variations. As noted previously, the performance of each pixel (detector) is different, so even though we assumed that the reference temperatures of the ground targets did not change in such a short period of time, the measurements can change because they are in a different part of the camera's sensor array. Finally, the performance of the camera can fluctuate with time due to the lack of a cooling mechanism, which can lead to thermal drift in the instrument.

Temperature bias increased for the white ground control point, vegetative surface, and white reference panel between the seed image and the other images (Table 2.9). After calibration and atmospheric correction, the difference between the calibrated bias of earlier images (17:10:19 and 17:10:23) and later images (17:11:59 and 17:12:01) was not consistent; however, the RMSE of all validation targets on this day decreased from 6.36°C to 1.24°C.

Table 2.5. Comparison between reference, uncalibrated, and calibrated temperature measurements. Uncertainty, defined as ±3 standard deviations of all measurements collected for the same target, is presented after the mean values. The values in this table are for ground reference targets on 25 August 2017 (16:37:11). This image was used as the seed image for the atmospheric correction.

Ground Reference Target	Ground Reference Temperature (T_{ref}, °C)	Uncalibrated Temperature (T_{uncal}, °C)	Calibrated Temperature (T_{cal}, °C)	Uncalibrated Bias (°C) ($T_{uncal} - T_{ref}$)	Calibrated Bias (°C) ($T_{cal} - T_{ref}$)
Vegetative surface	23.70 ±0.40	22.31 ±0.93	22.60 ±0.56	-1.39 ±0.93	-1.10 ±0.56
White reference panel	25.76 ±0.52	23.39 ±0.62	24.75 ±1.22	-2.37 ±0.62	-1.01 ±1.22

Table 2.6. Effectiveness of the atmospheric correction when applied to non-seed images of the water targets also taken on August 25, 2017. Time of image acquisition is indicated. All temperature values are presented as mean ± 3 standard deviations of all measurements collected for the same target. For the ground reference target this includes several discrete measurements using handheld TIR sensors, while for the camera measurements standard deviation is based on pixel variation.

Ground Reference Target	Time	Ground Reference Temperature (°C) (T_{ref})	Uncalibrated Temperature (°C) (T_{uncal})	Calibrated Temperature (°C) (T_{cal})	Uncalibrated Bias (°C) (T_{uncal} - T_{ref})	Calibrated Bias (°C) (T_{cal} - T_{ref})
Cold	16:38:53	8.77	7.01±2.00	7.14±1.28	-1.76±2.00	1.63±0.83
	16:38:55	8.77	10.98±4.22	6.83±1.71	2.21±4.22	1.94±1.71
Intermediate	16:38:53	24.75	19.61±1.06	22.86±1.10	-5.14±1.06	1.89±1.10
	16:38:55	24.75	20.66±0.95	23.35±1.79	-4.09±0.95	1.40±1.79
Hot	16:38:53	33.72	24.94±0.36	31.88±0.80	-8.78±0.36	1.84±0.80
	16:38:55	33.72	26.25±0.65	33.26±1.60	-7.47±0.65	0.46±1.60

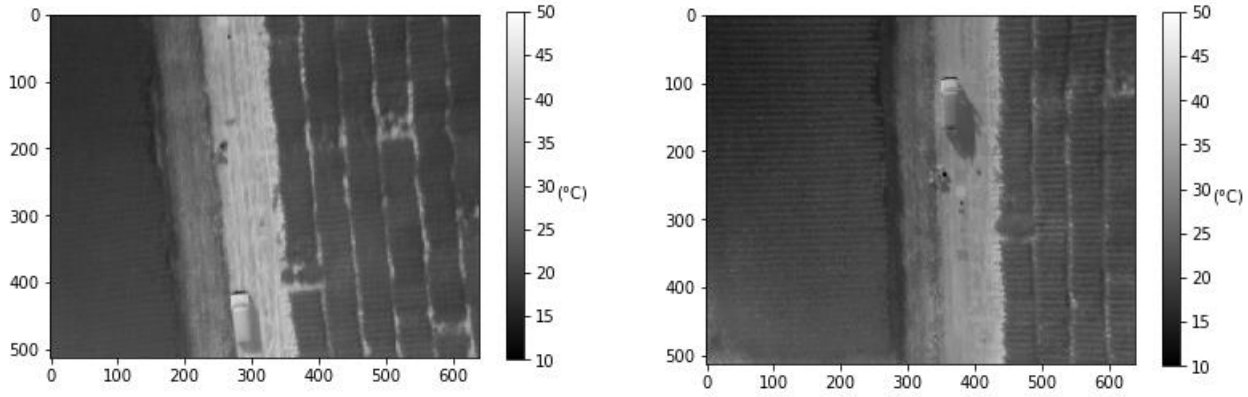

(a)

Figure 2.8. Thermal images from 25 August 2017 (left) and 28 September 2017 (right): (a) raw temperature images converted using FLIR radiometric calibration equations; (b) the same images after pixel-based calibration and atmospheric correction, and (c) the bias between thermal images (raw – corrected). The *X* and *Y* axes labels are image coordinates that help to identify the location of any pixel in the image.

Figure 2.8 continued

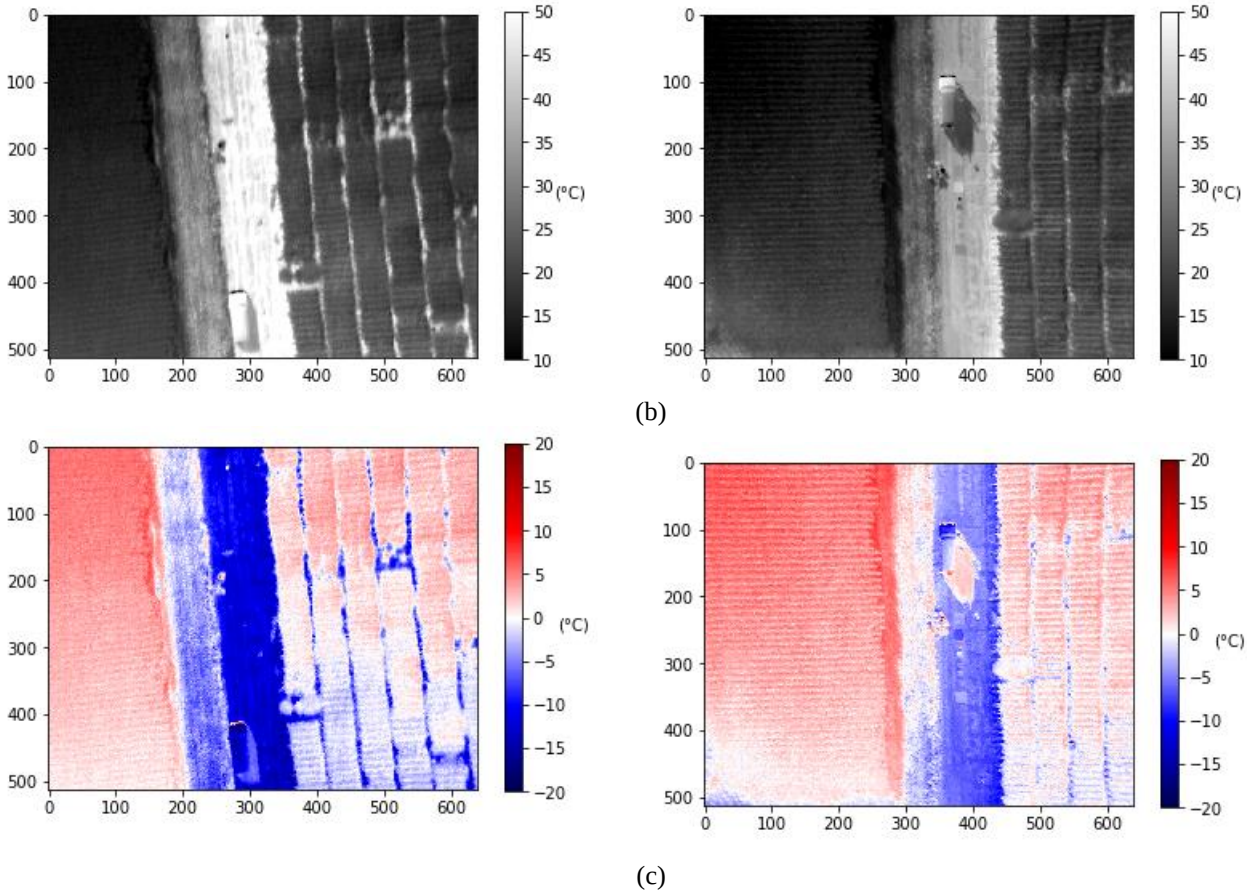

Table 2.7. Effectiveness of the atmospheric correction on non-seed images on August 25, 2017 based on vegetative surface temperature. All temperature values are presented as mean ±3 standard deviations of all measurements collected for the same target. For the ground reference target this includes several discrete measurements using handheld TIR sensors, while for the camera measurements standard deviation is based on pixel variation.

Time of Reference Target Acquisition	Ground Reference Temperature (°C) (T_{ref})	Uncalibrated Temperature (°C) (T_{uncal})	Calibrated Temperature (°C) (T_{cal})	Uncalibrated Bias (°C) (T_{uncal}- T_{ref})	Calibrated Bias (°C) (T_{cal}- T_{ref})
16:37:13	23.70±0.40	21.66±0.79	23.86±1.28	-2.04±0.93	0.16±1.28
16:38:53		19.41±1.07	23.46±0.30	-4.29±1.07	-0.24±0.30
16:38:55		19.83±0.75	22.51±1.05	-3.87±0.75	-1.19±0.75

The results indicate that the calibration and atmospheric correction method can be applied to the image from which it was developed (seed image) as well as to other images collected during the same flight. While there was increased variability and no consistent bias in the temperatures extracted from the non-seed images, the calibration and atmospheric correction method reduced the RMSE in all cases. While these experiments were not specifically designed to quantify thermal drift over the duration of the flight, the results illustrate that drift can be managed over a relatively short flight using these correction methods.

2.3.2 Accuracy assessment of using three water targets

To further evaluate the effectiveness of atmospheric correction with in-field water targets and to assess the impact of the number of target temperatures on the accuracy of the correction method, an additional experiment was conducted in 2020. During the flight on 6 August 2020, the three water target temperatures were adjusted twice by adding additional cold water. This resulted in flights with a total of nine different target temperatures. Atmospheric correction equations were developed using two to nine temperatures, and all possible combinations were evaluated.

Table 2.8. Effectiveness of the atmospheric correction on non-seed images from September 28, 2017. Ground reference temperature measurements based on bulk temperature measurements from water targets. Values are presented as mean ±3 standard deviations of all measurements collected for the same target.

Ground Reference Target	Time	Ground Reference Temperature (°C) (T_{ref})	Uncalibrated Temperature (°C) (T_{uncal})	Calibrated Temperature (°C) (T_{cal})	Uncalibrated Bias (°C) (T_{uncal} - T_{ref})	Calibrated Bias (°C) (T_{cal} - T_{ref})
Cold	17:10:19	1.07	5.89±1.42	2.39±0.49	4.82±1.42	1.32±0.49
	17:10:23	1.05	8.29±2.01	2.69±1.63	7.24±2.01	1.64±1.63
	17:11:59	1.10	16.17±3.23	2.59±0.52	15.07±3.23	1.49±0.52
	17:12:01	1.10	15.04±2.24	2.97±0.17	13.94±2.24	1.87±0.17
Intermediate	17:10:19	22.70	20.82±0.96	21.07±1.77	-1.88±0.96	1.63±1.36
	17:10:23	22.72	23.47±0.86	22.23±1.01	0.75±0.86	0.49±1.01
	17:11:59	22.76	29.26±0.92	21.04±2.02	6.5±0.92	1.72±2.02
	17:12:01	22.76	27.93±1.12	21.08±0.41	5.17±1.12	1.68±0.41
Hot	17:10:19	34.93	30.91±0.87	33.94±0.84	-4.02±0.87	0.99±0.84
	17:10:23	34.90	33.34±0.48	36.01±0.65	-1.56±0.48	1.11±0.65
	17:11:59	34.67	38.84±0.33	36.10±1.58	4.17±0.33	1.43±1.58
	17:12:01	34.67	37.22±0.61	35.07±1.51	2.55±0.61	0.40±1.51

Using any three water target temperatures yielded a large range in RMSE, from nearly 0.69°C to 7.93°C, while using all nine temperatures resulted in an RMSE of 0.86°C. However, when the temperatures of the three water targets are carefully set, such that the difference between each target is at least 4°C and the range between the hottest and coldest targets is greater than 25°C, the variability in RMSE can be constrained. The first criterion ensures that the water target temperatures can be differentiated in the thermal images, meaning that the temperatures must be farther apart than the in-field temperature uncertainty. Because this uncertainty can be slightly higher than ±1°C, the 4°C buffer ensures that they are distinguishable. The second criterion ensures that target temperatures are selected for current conditions.

Table 2.9. Comparison between ground reference, uncalibrated and calibrated temperature measurements for targets in the seed image (highlighted) and non-seed images for September 28, 2017. Ground reference temperature measurements were made using handheld FLIR thermometers for a selection of points within each ground-based target. Values are presented as mean ±3 standard deviations of all measurements collected for the same target.

Ground Reference Target	Time	Ground Reference Temperature (°C) (T_{ref})	Uncalibrated Temperature (°C) (T_{uncal})	Calibrated Temperature (°C) (T_{cal})	Uncalibrated Bias (°C) (T_{uncal} - T_{ref})	Calibrated Bias (°C) (T_{cal} - T_{ref})
White GCP [a]	**17:10:21**	22.32±0.35	25.27±1.40	22.97±0.98	2.95±1.40	0.65±0.98
	17:11:59		31.09±0.49	23.26±1.43	8.77±0.49	0.94±1.43
	17:12:01		30.29±2.35	23.62±1.87	7.97±2.35	1.30±1.87
Black GCP	17:10:19	31.19±0.35	28.11±1.53	29.78±1.66	-3.08±1.53	-1.41±1.66
	17:10:21		28.10±1.74	30.21±0.81	-3.09±1.74	-0.98±0.81
	17:10:23		29.87±0.99	30.55±0.46	-1.32±0.99	-0.64±0.46
	17:11:59		35.32±3.10	30.69±1.54	4.13±3.10	-0.50±1.54
	17:12:01		33.29±1.31	30.02±1.94	2.10±1.31	-1.17±1.94
Vegetative Surface	17:10:19	23.14±0.36	21.10±0.95	21.81±1.54	-2.04±0.95	-1.33±1.54
	17:10:21		24.55±0.43	23.02±0.83	1.41±0.43	-0.12±0.83
	17:10:23		24.29±1.18	23.38±1.23	1.15±1.18	0.24±1.23
	17:11:59		29.01±0.91	22.32±0.40	5.87±0.91	-0.82±0.40
	17:12:01		28.04±0.68	21.67±0.99	4.90±0.68	-1.47±0.99
White reference panel	17:10:19	25.01±1.64	19.47±1.34	23.71±1.01	-5.54±1.34	-1.30±1.01
	17:10:21		21.33±1.64	25.20±1.09	-3.68±1.64	0.19±1.09
	17:11:59		28.71±0.82	26.03±1.45	3.70±0.82	1.02±1.45
	17:12:01		27.18±1.71	25.41±1.84	2.17±1.71	0.40±1.84

[a] GCP: ground control point

Analysis of the dataset shows that if the minimum temperature is less than 10°C, the maximum temperature is above 35°C, and no water targets are closer than 4°C from each other, then the RMSE is always less than 1.00°C (Figure 2.9). If the temperature range criterion is eased to 20°C, then there is only a 64% chance that the RMSE will be less than 1.49°C. The water target temperatures used for all analyses in the previous sections conformed to these characteristics.

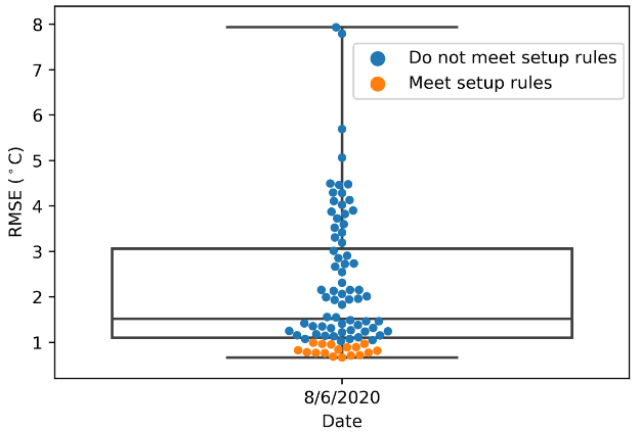

Figure 2.9. Distribution of RMSE between ground reference temperatures and thermal image estimated temperatures when using all combinations of three water targets selected from all nine temperature targets. The RMSE for each model is shown as a dot. The distribution of RMSE for all combinations is shown with a box plot, where the top whisker indicates the worst RMSE, the top of the box indicates the 25th percentile RMSE, the middle line indicates the median RMSE, the bottom of the box indicates the 75th percentile RMSE, and the lower whisker indicates the lowest RMSE. Orange dots indicate RMSE values for sets of three targets that meet the setup criteria, and blue dots indicate RMSE values for those that do not meet the setup criteria.

2.4 Discussion

Inexpensive, uncooled thermal infrared cameras mounted on UAS are becoming an increasingly important method of measuring various land surface temperatures, with the expectation that derived variables, such as latent heat flux, will eventually be computed from the resulting images. However, without appropriate calibration and correction of atmospheric effects, the temperature bias can be significant. This study presents a novel pixel-based calibration method and in-field atmospheric correction method and quantifies the resulting reduction in bias and uncertainty in temperature estimates from a small, uncooled thermal infrared camera. The use of such cameras for UAS is still relatively new, so there are currently only a few similar studies, but there is a larger body of work using cooled cameras on satellite and aircraft platforms (Jensen et al., 2014).

For calibration accuracy, Budzier and Gerlach (2015) and Ribeiro-Gomes et al. (2017) reported after-calibration uncertainties of ±1.00°C and approximately ±1.50°C for uncooled thermal cameras, respectively (without reporting standard deviations). This is similar to the uncertainty of ±1.70°C reported here. For atmospheric correction, uncertainty ranges from ±0.89°C to ±2.00°C

have been reported in the literature using MODerate resolution atmospheric TRANsmission (MODTRAN) and local measurements to derive the terms in the governing equation (Equation 2.1) for radiation propagation for UAS-based sensors (Berni et al., 2009b; Torres-Rua, 2017) and from ±1.00°C to ±2.00°C for satellite-based sensors (Schott et al., 2012; O'Donnell et al., 2002), which supports the conclusion that the accuracy reported here (less than ±1.32°C) is acceptable, given the quality of the camera used.

It should be noted that previous studies used a variety of camera models, which had an impact on their calibration results. The camera used in the present research has a manufacturer's uncertainty of ±5.00°C, while the uncertainty of many of the cameras used in previous studies (specifically Ribeiro-Gomes et al., 2017; Berni et al., 2009b; Torres-Rua, 2017) was ±2.00°C. Given that the cameras used in previous studies had higher base accuracy, the ability of the method described here to provide a similar range of uncertainty with a lower-accuracy camera is significant.

The accuracy reported in this research is sufficient to differentiate the canopy from bare soil, with an average temperature difference of 7.40°C for the flights reported here. How the reported accuracy will affect latent heat estimates is still being determined. Challenges remain for the use of thermal infrared cameras when temperature accuracy is important. The water targets used in this research are cumbersome and time-consuming to set up, which limits the number of targets that can be deployed in the field as well as the locations at which they can be deployed. In addition, the performance of the water targets has only been tested under a limited number of atmospheric and surface conditions. How well they will work under more extreme weather conditions and for targets with different emissivity is a subject for future research.

2.5 Conclusion

A method was presented to improve the accuracy of temperature observations from a UAS-based uncooled thermal infrared camera using a combination of laboratory calibration and in-field water targets for atmospheric correction. The pixel-based thermal calibration method presented here was able to reduce the measurement uncertainty across all the pixels in the images, thus improving the accuracy and reducing the between-pixel variability of the measurements. After calibration, the camera was more accurate over the range of normal temperatures within its field of view during

the growing season. The results suggest that a non-linear calibration function might be more appropriate if a wider calibration range is required.

During field calibration, the RMSE values relative to ground reference targets for two flights in 2017 were reduced from 6.36°C to 1.24°C and from 4.56°C to 1.32°C, respectively. The results also indicate that building a single atmospheric correction relationship using the seed image and the ground-based water targets was sufficient to reduce measurement uncertainty in all cases for the duration of the flight.

Further data analysis from flights in 2020 indicated that when using water targets with three temperatures, a minimum temperature less than 10°C, and a maximum temperature above 35°C, the RMSE of the calibrated temperature will always be less than 1.00°C. If the temperature range requirement is eased to 20°C, then there is only a 64% chance that the RMSE will be less than 1.49°C.

Calibration and atmospheric correction increased the range of measured temperatures in the images and increased the image contrast, which may help with identification of tie-points and stitching of images together to form whole-field mosaics. Image calibration and atmospheric correction are important for achieving the best accuracy in measured temperatures, which will become even more important as vegetative surface temperature is used to estimate latent heat flux and is included in multi-sensor fusion to better predict crop biomass and yield.

Future work includes improving the design of the water targets to incorporate lessons learned after multiple seasons of use, with a focus on making the targets more mobile with a larger water surface area to increase their visibility in the thermal imagery collected from UAS platforms and testing the performance of the developed calibration methods under a broader range of weather and surface conditions.

3. ESTIMATION OF LATENT HEAT FLUX FROM HIGH RESOLUTION THERMAL IMAGERY

Abstract

Crop evapotranspiration (ET) which is directly related to latent heat flux is also a key indicator in determining the water status of crops. In order to estimate the latent heat flux, two source energy balance models (TSEB) have been developed for thermal imagery from satellite platforms. However, because of the coarse resolution of thermal sensors on the satellite, distinguishing soil and vegetation is difficult which complicates the calculation process and introduces errors in latent heat estimates. In this research, very high- resolution thermal datasets (0.05 m) and corresponding RGB datasets (0.03 m) were used for calculating crop latent heat flux using an adapted TSEB model. The RGB datasets were used for supervised classification of soil and vegetation, the classification results were then used to filter the thermal mosaics to separate vegetation and soil temperatures, then the vegetation temperature is used for calculating latent heat flux and finally the results are validated against ground porometry measurements as well as latent heat flux calculated from the Penman-Monteith (PM) equation using local weather data. The objective of this research is to introduce a work flow including an adapted TSEB model, which is customized for high resolution thermal images from unmanned aircraft systems (UAS), to estimate latent heat flux of row crops in agricultural fields. Nine dates of data collection in 2018 and 2020 have been evaluated and the root mean square error (RMSE) varies between 16 to 106 W/m^2 depending on the days after planting (DAP) and the time of measurement for each day. The results indicate that the workflow introduced here is able to provide instantaneous latent heat flux (evapotranspiration) measurements for row crops in agricultural fields which will enable people to make reliable decisions related to irrigation scheduling.

3.1 Introduction

Crop evapotranspiration (ET), which transfers a large volume of water into the atmosphere from the combination of evaporation from soil, water bodies, vegetated surfaces (E) and transpiration (T), which is a fundamental part of the photosynthesis process in plants, is directly related to latent heat flux (latent heat flux is converted to ET by dividing by $\lambda \times \rho_w$, where λ is the latent heat of

vaporization and ρ_w is the density of water) (Jensen and Allen, 2016) and has played a key role in determining the water status of crops, thus serving as an important indicator for management of irrigation and water resources in areas of water scarcity. (Anderson et al., 2012; Khanal et al., 2016). ET estimation is critical for addressing immediate needs at farm scales, including improved crop water management and irrigation efficiencies, weather and crop-stress forecasting, and decision-support tools as water supplies become increasingly constrained in the 21st century.

The primary controls on ET are energy inputs such as incoming solar radiation, and the capacity of the air to hold more water vapor both from local water vapor (humidity) and from mixing with drier air controlled by wind speed. Air temperature has a less direct impact on the ET rate (latent heat flux) because it affects the water holding capacity of the air and it is therefore highly correlated with both solar radiation and ET. Other factors such as different growing stages for the agricultural crops, soil and management factors (soil's water content, its water characteristic curve and available soil water content) can also affect the latent heat flux (Jensen and Allen, 2016; Allen et al., 1998; Heitman et al., 2010).

Traditional measurement systems for crop ET include: (1) lysimetry, which measures evaporation and transpiration based on the change in weight of a lysimeter where weight change is associated with the change in soil water storage once precipitation and drainage are removed (Marek et al. 1988, Howell, McCormick and Phene, 1985); (2) eddy covariance systems that directly quantify ET by measuring three-dimensional wind velocities and water vapor content of air fluxes at very high resolutions (Swinbank, 1951;Twine et al., 2000); and (3) Bowen Ratio energy balance systems that indirectly quantify ET by measuring net radiation, soil heat flux and vapor pressure at two different heights and applying the Bowen ratio energy balance equation (Bowen, 1926). Each of these methods require great care and expense to collect accurate measurements for inputs, and are very limited in the spatial area for which they are representative.

In 1948, Penman combined the energy balance with the mass transfer method and derived an equation to compute the evaporation from an open water surface from standard climatological records of sunshine, temperature, humidity and wind speed. This method was further developed and extended to cropped surfaces by introducing resistance factors. In 1990, the FAO

recommended the adoption of the Penman-Monteith combination method as a new standard for reference evapotranspiration and advised on procedures for calculation of the various parameters (Allen et al., 1998). However, these measurements are very labor intensive and require substantial time for data collection and sensor maintenance. Their measurement footprints are also very limited so cannot meet the increasing needs to have high-resolution spatially explicit measurements for mapping field, regional and meso scale patterns of ET on the Earth's surface. The variability of ET also makes it very difficult for any sort of interpolation and extrapolation based on the values from coverage area. In this case, remote sensing platforms (unmanned aircraft systems and satellites) with thermal sensors installed have been used for this purpose more often recently (Singh and Irmak, 2009; Jensen and Allen, 2016; Anderson et al., 2012; Song et al., 2016).

Surface energy balance models are based on balancing net radiation with ground heat flux, sensible heat flux and latent heat flux assuming that heat advection is negligible (Hoffmann et al., 2016). Surface temperature estimates from those remote sensing systems can be used in the models to indirectly estimate sensible heat flux, net radiation and ground heat flux using some local weather data, and in this way, latent heat flux can be solved as the residual. Such models can be used to estimate latent heat over large areas without significant investment in specialized equipment and may be the only approach available for ungauged areas where man-made measurements are extremely difficult to conduct.

Original development of these energy balance models assumed a single incoming energy source at the land surface, effectively representing the land surface as covered by a single big leaf. Norman et al. (1995) introduced an iterative method known as Two-Source Energy Balance (TSEB) model that includes energy transfer from the soil to the vegetation as a separate, second source of energy to more accurately calculate the joint latent heat flux of the plant canopy and soil. This method uses remote sensing measurements of surface directional brightness temperature and some ancillary data (weather parameters such as air temperature, humidity, wind speed and ground measurements like soil temperature, and leaf area index (LAI)). Since brightness temperature measurements are typically available only at a single viewing angle, a Priestly-Taylor approximation (Priestley and Taylor, 1972) is used to acquire an initial estimation of canopy temperature then latent het flux can be calculated in an iterative manner. Because the TSEB was

developed for satellite remote sensing systems, it suffers from a lack of fine spatial resolution data to distinguish between soil and plants and fine scale temporal data to monitor the water status of crops in real time.

The potential to adapt the TSEB method to data collected from unmanned aircraft systems (UAS) can reduce the limitations of satellite-based ET estimates by obtaining imagery with centimeter level spatial resolution and the potential to collect imagery several times a week or even within the same day as needed. For example, Benner et al. (2017) mapped ET from a grass site with land surface temperature acquired from UAS as an input to both one and two-source energy balance models. They collected thermal imagery with a spatial resolution of 5 cm during the months of June and July. When comparing the simulated latent heat flux from these models with coincident eddy covariance measurements, they found that the two-source model, with a more complex treatment of the energy and surface temperature partitioning between the soil and vegetation, outperformed the simpler one-source model in estimating sensible and latent heat fluxes. Norman et al. (2000) developed the dual-temperature-difference (DTD) model by incorporating two temperature observations into the TSEB modelling scheme: one conducted an hour after sunrise and another conducted later the same day when flux estimations are desired. Hoffmann et al. (2016) compared the performance of two dual-source models (TSEB and DTD) by using land surface temperature (LST) from mosaics of thermal imagery from UAS with a spatial resolution of 0.2 m as an input to the models. They found that both TSEB and DTD simulations were in good agreement with eddy covariance measurements. The DTD model results were better, but significantly limiting its potential use given the need for two acquisitions per day rather than one.

One of the main sources of error for the TSEB model derives from the estimation of canopy and soil temperature through an iterative process rather than from direct measurements. Ortega-Farías et al. (2016) incorporated thermal and multispectral imagery into a remote sensing energy balance (RSEB) algorithm to simulate net radiation, soil, sensible and latent heat fluxes in an olive orchard. They separated canopy and soil surfaces from imagery manually by using discrimination and segmentation supervised techniques. With this technique they found that the simulated values were generally in good agreement with flux measurements from an eddy covariance system. All of their data acquisition occurred near solar noon. Riveros-Burgos et al. (2021) applied a clumped

model developed by Brenner and Incoll (1997) to estimate olive orchard evapotranspiration using high resolution thermal imagery. They found the estimated values were in accord with the ground-based measurements while the main disagreements were associated with olive trees under moderate water stress and high atmospheric demand for water vapor. In order to distinguish between canopy and soil temperature, the K-means clustering algorithm was applied to the thermal orthomosaics and a binary raster was created with two clusters where pixels were classified for canopy and soil. However, this classification may cause a problem since under lots of conditions, there is no clear difference in temperature values between soil and canopy.

Previous research indicates the potential of using high resolution thermal imagery along with energy balance model for calculating latent heat flux of orchard or grass, but little research has done to test the performance of the model on row crops. Also, the model has only been tested under a certain illumination condition and on a relatively coarse resolution, so to what extent the models can be applied to higher resolution imagery is still questionable. Partitioning between the canopy and soil is always important, since calculations of energy components of these two will require different sets of equations, and this was done previously by using the NDVI and temperature difference (Nieto et al., 2019; Riveros-Burgos et al., 2021). However, under field condition, the temperature difference of the two is not certain and also the NDVI threshold values for the vegetation and soil are empirical and will result in errors from day to day.

The objective of this research is to introduce a work flow including using an adapted TSEB model, customized for high resolution thermal images from UAS, to estimate latent heat flux from row crops in agricultural fields. In this research, very high-resolution thermal datasets (0.05 m) and corresponding RGB datasets (0.03 m) were used for calculating crop latent hear flux. The RGB datasets were used for supervised classification of soil and vegetation, the classification results were then used to filter the thermal mosaic to separate vegetation and soil temperatures, then the vegetation temperature is used for calculating latent heat flux and finally the results are validated against in situ porometry measurements as well as latent heat flux calculated from the Penman-Monteith (PM) equation using local weather data. Multiple flights are processed using the model, and the variance of latent heat flux between different days from a single growing season is assessed using supplementary information including weather parameters.

3.2 Methods

3.2.1 Field site

Data was collected in the summer of 2018 and 2020. All of the flights took place at Agronomy Center for Research and Education (ACRE), a research farm operated by Purdue University. A mixture of corn and sorghum fields identified as “field 54” (40°28'44.98"N, 86°59'23.57"W) (Figure 3.1) is the target for all flights. This field is about 5 hectares and was set up to support breeding experiments, with one or more experiments established in it every other year, each experiment consisting of hundreds to thousands of smaller plots with specific genotypes of sorghum or corn.

The air temperature, relative humidity, solar radiation, precipitation, and wind speed are measured at 30-min intervals using an automatic meteorological station located near the experimental site (500 m away). These data were used to calculate the hourly reference latent heat flux according to the Penman-Monteith model (Allen et al., 1998) and also used as inputs to the modified TSEB model for calculating latent heat flux from UAS imagery.

Figure 3.1. Locations of ACRE and the research field.

3.2.2 Remote sensing data acquisition and processing:

A FLIR DUO Pro R camera (FLIR Systems, Wilsonville, Oregon.) and a ThermalCapture Fusion Zoom camera (TeAx, Germany) were used to capture all thermal infrared imagery used in this

analysis. Each of these cameras consists of two sensors: a thermal infrared imager and a visible-light imager. The thermal imagers are the same with a resolution of 640×512 and a focal length of 19 mm with a field of view 32°× 26°. Both thermal imagers are sensitive to spectral wavelengths from 7.5 to 13.5 µm. Their measurement accuracy is ±5°C or 5% of reading in its operating temperature range (20°C to +50°C). The visible-light imager of FLIR DUO Pro R has a resolution of 4000×3000, while that of ThermalCapture Fusion Zoom is 1920×1080 and has a 10 times optical zoom. Both cameras have been calibrated in the lab using methods described in (Zhu and Cherkauer, 2021).

The FLIR camera was mounted on the underside of a DJI M200 Drone and the ThermalCapture Fusion Zoom camera was mounted on the underside of a DJI M600 Drone (Shenzhen, China) with a gimbal so that nadir images were collected during flights. Flights were conducted at a height of 60 m so that the ground sampling distance is about 5.4 cm per pixel for the imagery from both thermal imagers, and 3.3 cm per pixel for the visible imagery from FLIR camera and 4.2 cm per pixel from ThermalCapture camera. The speed of the M200 drone was 5.6 m/s and that of M600 was 7.5 m/s. The spacing between flight paths was set to be 6.8 m for both drones to achieve a frontal overlap of 80% and 95% for thermal images from FLIR and ThermalCapture and a side overlap of 80%. The ThermalCapture camera takes still images at a frame rate of 5 fps. A software named ThermalViewer (TeAx, Germany) is used for extracting thermal and RGB frames from the ThermalCapture camera. Most of the flights were conducted in the afternoon around 2-4 pm to provide for stable air temperature conditions.

Pix4D mapper software (Pix4D S.A., Switzerland) was used for creating mosaics for both RGB and thermal datasets. The mosaics of these two datasets on the same day and same flight were then registered to each other in ENVI (L3Harris Geospatial, Colorado, USA) using ground control points deployed around the field. The RGB images were used as the base images for warping the corresponding thermal images. Four other GCPs on each side of the field which were not used in the coregistration process were used for accuracy evaluation. The RMSE for both horizontal and vertical directions of these GCPs in both images have been calculated for evaluating the accuracy of registration. After the registration, areas of interest (an area within the field usually contains multiple plots in the shape of rectangle) were extracted from the full mosaic image. A supervised

classification workflow in ENVI was run on the RGB images. The Mahalanobis Distance algorithm (De Maesschalck et al., 2000) was selected to provide a conservative result which largely avoid misclassifying soil pixels into vegetation pixels but may ignore some dark vegetation pixels. The classification accuracy was evaluated by a confusion matrix method as described by Lillesand et al. (2014). More than 100 points were selected randomly between classification results and original images for three classes: dark soil, sunlit soil and crops. These points were used to compute the producer and user accuracies of the classified imagery. The classification results were then overlaid on the corresponding thermal images as a mask to separate vegetation from soil, as only the vegetation temperature is used for calculating latent heat flux.

Canopy temperature and soil temperature are directly acquired from the high-resolution thermal imagery. Thermal imagery was calibrated by on-site water targets to get accurate temperature measurements (Zhu and Cherkauer, 2021).

3.2.3 Two-Source Energy Balance (TSEB) model

Instead of treating the land surface as a big leaf with a single uniform layer as was done with the original one source energy balance (OSEB) models, the TSEB model distinguishes between the surface energy transfer of soil and vegetation sub-systems and requires soil and canopy surface temperatures to solve the energy budgets of these layers separately (Colaizzi et al., 2012; Tang et al., 2012) which improves the accuracy of the resulting latent heat flux estimates. An overview of the critical components of the TSEB employed in this research is provided below, along with a discussion of how the model was modified and employed for this project.

The canopy and soil energy balance is described as:

$$R_N = G + H + LE \tag{3.1}$$

In which, R_N is the net radiation, G is the soil heat conduction flux; H is the sensible heat flux and LE is the latent heat flux. With high resolution thermal imagery becoming more available these days, vegetation and soil can be separated in imagery and surface energy fluxes calculated

separately. Because the focus of this study is on LE from crops, only the canopy energy balance equations are discussed below.

Latent heat flux of canopy is calculated by following equations.

$$LE_C = R_{n,CANOPY} - H_C \tag{3.2}$$

In which, and $R_{n,CANOPY}$ is the canopy net radiation and H_C is sensible heat flux of the canopy.

Net Shortwave Radiation

Net radiation is the balance between net shortwave radiation and net longwave radiation. Net shortwave radiation consists of two components: net direct radiation and net diffuse radiation.

Canopy direct visible radiation S_{dirvis} is expressed as follows (Kustas and Norman, 2016):

$$S_{dirvis} = (1 - \tau_{dirv}(\psi)) \times (1 - \rho_{dirv}(\psi)) \times S\_dir \times fvis \tag{3.3}$$

In which $\tau_{dirv}(\psi)$ is the flux density of radiation under the canopy, $\rho_{dirv}(\psi)$ is the canopy reflection coefficient for beam irradiance, S_dir is the total direct shortwave radiation and $fvis$ is the fraction of visible radiation in total shortwave radiation. The wavelength of energy, ψ, can be used to split shortwave radiation into visible and near infrared radiation.

The flux density of radiation under the canopy can be calculated by (Campbell and Norman, 2012):

$$\tau_{dirv}(\psi) = \frac{[(\rho^*_{b,cpy}(\psi)^2 - 1]\, exp(-\sqrt{\alpha} K_{be}(\psi) L_t)}{(\rho^*_{b,cpy}(\psi)\rho_s - 1) + \rho^*_{b,cpy}(\psi)(\rho^*_{b,cpy}(\psi) - \rho_s)\, exp(-2\sqrt{\alpha} K_{be}(\psi) L_t)} \tag{3.4}$$

In this equation, ρ_s is the soil reflectance in visible spectrum which is 0.05(0.1 for near infrared spectrum), $K_{be}(\psi)$ is the extinction coefficient which depends on the canopy structure and the beam zenith angle; L_t is the depth of the canopy, and beam reflection coefficient for the canopy $\rho^*_{b,cpy}(\psi)$ can be acquired from the following;

$$\rho^*_{b,cpy}(\psi) = \frac{2K_{be}(\psi)}{K_{be}(\psi)+1}\rho^H_{cpy} \tag{3.5}$$

The canopy hemispherical reflection coefficient, ρ^H_{cpy}, depends on the leaf absorptivity (α) and is calculated as:

$$\rho^H_{cpy} = \frac{1-\sqrt{\alpha}}{1+\sqrt{\alpha}} \tag{3.6}$$

The leaf absorptivity of radiation in the visible spectrum and the near infrared spectrum is 0.8 and 0.2 respectively.

The extinction coefficient is calculated as follows:

$$K_{be}(\psi) = \frac{\sqrt{\chi^2+tan^2\psi}}{\chi+1.774(\chi+1.182)^{-0.733}} \tag{3.7}$$

In which, ψ is the solar zenith angle and χ is the ratio of average projected areas of canopy elements on horizontal and vertical surfaces. This value depends on crop types and for maize, the focus of this work, it equals 1.37 (Campbell and Norman, 2012).

The canopy reflection coefficient for beam irradiance is calculated by:

$$\rho_{dirv}(\psi) = \frac{\rho^*_{b,cpy}+[\frac{\rho^*_{b,cpy}-\rho_s}{\rho^*_{b,cpy}\rho_s-1}]\,exp(-2\sqrt{\alpha}K_{be}(\psi)L_t)}{1+\rho^*_{b,cpy}[\frac{\rho^*_{b,cpy}-\rho_s}{\rho^*_{b,cpy}\rho_s-1}]\,exp(-2\sqrt{\alpha}K_{be}(\psi)L_t)} \tag{3.8}$$

The total directive and diffusive shortwave radiation can be expressed as:

$$S\_dir = S\_dn \cdot f_{vis} \cdot f_V + S\_dn \cdot f_{nir} \cdot f_N \tag{3.9}$$

$$S\_dif = S\_dn \cdot f_{vis} \cdot (1 - f_V) + S\_dn \cdot f_{nir} \cdot (1 - f_N) \tag{3.10}$$

In which S_dn is the measured incoming shortwave radiation (W/m^2). f_{vis} is the fraction of visible radiation in the total shortwave radiation; f_V is the faction of direct beam in the visible radiation; f_{nir} is the fraction of near infrared radiation in the total shortwave radiation; and f_N is the faction of direct beam in the near infrared radiation.

The above fraction parameters can be acquired from the following equations (Weiss and Norman 1985):

$$f_V = \frac{R_{DV}}{R_V}\left[1 - \left(\frac{A - RATIO}{B}\right)^{2/3}\right] \tag{3.11}$$

$$f_N = \frac{R_{DN}}{R_N}\left[1 - \left(\frac{C - RATIO}{D}\right)^{2/3}\right] \tag{3.12}$$

$$f_{vis} = \frac{R_V}{R_V + R_N} \tag{3.13}$$

$$f_{nir} = \frac{R_N}{R_V + R_N} \tag{3.14}$$

In the above equations, A, B, C and D are constants and equal to 0.9, 0.7, 0.88 and 0.68 respectively. R_{DV} is the potential visible direct beam radiation falling on a horizontal surface; R_V is the total potential visible radiation; R_{DN} is the potential direct beam near-infrared radiation on a horizontal surface; R_N is the total potential near-infrared radiation; RATIO is defined as the ratio of measured to potential radiation.

$$RATIO = \frac{S\_dn}{R_V + R_N} \tag{3.15}$$

The potential shortwave radiation consists of two components: R_V potential visible radiation and R_N potential near-infrared radiation. Either of them is the sum of direct and diffuse radiation of its own.

$$R_V = R_{DV} + R_{dV} \tag{3.16}$$

$$R_N = R_{DN} + R_{dN} \tag{3.17}$$

The potential visible direct beam radiation falling on a horizontal surface is approximated by

$$R_{DV} = 600 \exp\left[-0.185\left(\frac{P}{P_0}\right)m\right]\cos(\psi) \tag{3.18}$$

In which $\frac{P}{P_0}$ is the ratio of actual to sea level pressure (101.325 kPa); $m = (cos\psi)^{-1}$ is the optical air mass.

The potential visible diffuse radiation is calculated from:

$$R_{dV} = 0.4(600 - R_{DV})\cos(\psi) \tag{3.19}$$

The potential direct and diffuse beam near-infrared radiation on a horizontal surface are calculated by Equations 3.19 and 3.20.

$$R_{DN} = [720 \exp\left(-0.06\left(\frac{P}{P_0}\right)m\right) - \omega]\cos(\psi) \tag{3.20}$$

$$R_{dN} = 0.6[720 - R_{DN} - \omega]\cos(\psi) \tag{3.21}$$

In which, ω is the water absorption in the near infrared for 10 mm of precipitable water.

$$\omega = 1320 antilog_{10}[-1.1950 + 0.4459 log_{10}m - 0.0345(log_{10}m)^2] \tag{3.22}$$

Similarly, canopy diffuse visible radiation (S_{difvis}), direct near infrared radiation (S_{dirnir}), and diffuse near infrared radiation (S_{difnir}) can be expressed as:

$$S_{dirnir} = (1 - \tau_{dirn}(\psi)) \times (1 - \rho_{dirn}(\psi)) \times S\_dir \times fnir \tag{3.23}$$

$$S_{difvis} = (1 - \tau_{dirv}(\psi)) \times (1 - \rho_{difv}(\psi)) \times S\_dif \times fvis \tag{3.24}$$

$$S_{difnir} = (1 - \tau_{difn}(\psi)) \times (1 - \rho_{difn}(\psi)) \times S\_dif \times fnir \quad (3.25)$$

In which, S_dif is the incoming diffuse shortwave radiation. Similarly, $\tau_{dirn}(\psi), \tau_{dirv}(\psi),$ and $\tau_{difn}(\psi)$ can be calculated by Equation 3.4 with respective parameters. $\rho_{dirn}(\psi)$, $\rho_{difv}(\psi)$, $\rho_{difn}(\psi)$ is acquired through different absorptivities through Equation (3.8). Adding all four components together, we will get net shortwave radiation on the canopy.

Longwave radiation

The net longwave radiation on the canopy, where incoming longwave radiation from the sky and soil is balanced by outgoing longwave radiation from the canopy itself, is calculated using (Kustas and Norman, 1999):

$$L_{N,C} = [1 - \tau_{bt}(\psi)][L_{sky} + L_S - 2L_C] \quad (3.26)$$

Where L_{sky}, L_C and L_S are longwave radiation (W m^{-2}) from the sky canopy and soil, respectively. $\tau_{bt}(\psi)$ is the percent of total beam radiation (direct and down scattered) transmitted through the canopy, which is computed as:

$$\tau_{bt}(\psi) = exp(-\sqrt{\alpha}K_{be}(\psi)L_t) \quad (3.27)$$

Latent heat from the sky and canopy are calculated using Stefan-Boltzmann law based on their observed temperatures. Most of the thermal images acquired are nadir images which means that much of the soil is obscured by the canopy at later growth stages, and this part of the soil cannot be separated by the classification algorithm. Since the soil is completely shaded, L_s is calculated using the minimum values of neighboring soil temperature measurements of the target vegetative surface.

Monin-Obukhov similarity theory:

Obukhov stability length is defined as (Brutsaert, 2005; Kustas and Norman, 1999):

$$L = \frac{-u_*{}^3}{L_{constant}(\frac{H_v}{\rho c_p})} \tag{3.28}$$

Where u_* is friction velocity (m s^{-1}), H_v is the virtual sensible heat flux (W m^{-2}), ρ is the density of air (kg m^{-3}), c_p is the heat capacity of air (J kg^{-1} °C^{-1}); $L_{constant}$ is expressed as follows:

$$L_{constant} = \frac{kg}{T_A} \tag{3.29}$$

Where k is von Karman's constant (≈0.4), g is the acceleration of gravity (m s^{-2}) and T_A is the air temperature at the time of measurement.

The virtual sensible heat flux is defined as:

$$H_v = H + (0.61 \times T_A \times c_p \times \frac{LE}{\lambda}) \tag{3.30}$$

In which, λ is the latent heat of vaporization, LE (W m^{-2}) is the latent heat flux and H is the sensible heat flux (W m^{-2}). In this research, the latent and sensible heat flux are assumed to be for vegetation.

The Aerodynamic Resistance is expressed as:

$$R_A = \frac{[ln(\frac{z_U - d}{z_M}) - \Psi_m][ln(\frac{z_T - d}{z_M}) - \Psi_h]}{0.16U} \tag{3.31}$$

Where z_U and z_T are the height of wind speed measurement U and air temperature measurement. Ψ_m and Ψ_h are the diabatic correction factors for momentum and heat. d is displacement height ($d \approx 0.65h_C$, where h_C is canopy height.) z_M is the roughness length for momentum ($z_M \approx 0.125h_C$)

When leaves are cooler than the air, the atmosphere is stable and the direction of sensible heat flux is downward with a negative sign. In that case, the following equation is used to calculate Ψ_m and Ψ_h(Brutsaert, 2005):

$$\Psi_m(\zeta) = \Psi_h(\zeta) = -5\zeta \tag{3.32}$$

Otherwise, if the atmosphere is unstable, empirical linear equations, which are a simplified version of original equations are used:

$$\Psi_m = -2.486\zeta + 0.0036 \tag{3.33}$$

$$\Psi_h = -5.624\zeta + 0.0449 \tag{3.34}$$

where ζ is defined in the following equation:

$$\zeta = \frac{h_c - d}{L} \tag{3.35}$$

Substituting into the equation for R_A (Equation 3.30) can be expressed as a parameter with only one unknown value which is the canopy sensible heat flux.

Canopy sensible heat flux can be calculated as (Norman et al., 1995):

$$H_C = \rho C_P \frac{T_C - T_A}{R_A} \tag{3.36}$$

Then latent heat flus can be calculated by substituting the sensible heat flux into Equation 3.2.

3.2.4 Ground reference measurements

Given the difficulty of measuring ET directly from a large field, two methods were used to provide ground reference for the UAS based latent heat estimates. These were the calculation of ET using the Penmen-Monteith method and local atmospheric conditions, and the direct measurement of

stomatal conductance from a small number of plants within the field experiment. More about each of these methods is provided below.

Penmen-Monteith Method for ET Estimation

Hourly Crop reference ET (ET_O) is calculated using the method defined by the United Nation's Food and Agriculture Organization (FAO; Allen et al., 1998). The relationship between crop ET (ET_c) and ET_o is:

$$ET_c = K_c \times ET_O \tag{3.37}$$

In which K_c is the crop coefficient which can be acquired from Piccinni et al. (2009) and Allen et al. (1998) based on the number of days after planting (DAP) for each field plot.

Stomatal Conductance Method for ET Estimation

Stomatal conductance is the measure of the rate of water loss through stomata on a leaf. This rate is a function of the plant type (density and size of the stomata) and the degree to which the stomata are open. Plants can close their stomata when stressed or at night to reduce water loss. The degree to which the stomata are open can be measured using a commercially available porometer, which measures the conductance of the leaf in series with two known conductance elements and comparing the humidity between them. The humidity difference across each of the known conductance elements results in measurements of the water vapor flux. The stomata conductance is a function of the distances between humidity sensors, temperature, and the humidity inside the leaf and at both of the humidity sensors (Devices, 2006).

Latent heat flux for the porometer measurement location can be calculated from the stomatal conductance measurement by the following equation (Jackson et al., 1981; Gerosa et al., 2012):

$$\lambda ET = \rho c_p (e_c^* - e_A)/[\gamma(r_b + r_s)] \tag{3.38}$$

Where ρ is the density of air (kg m^{-3}), c_p is the heat capacity of air (J kg^{-1} °C^{-1}), e_c^* is the saturated vapor pressure (Pa) dependent on canopy temperature, e_A is the vapor pressure of the air, γ is the

psychrometric constant (Pa°C^{-1}), r_b is the resistance of the leaf boundary laminar sub-layer and r_s is the resistance to the stomatal openings. r_b is calculated by the following equation:

$$r_b = 132(\frac{d_{leaf}}{u})^{0.5} \quad (3.39)$$

Where d_{leaf} is the downwind leaf dimension and can be approximated by the sample area of the porometer which is 4 cm^2.

In this research, we measured the stomatal conductance (the reverse of r_s) by using the porometer. The values of ρ, $c_p$and γ are known constants and r_b can be derived from the above equation. Finally, $e_c{}^*$and e_A can be acquired from the weather station that is located about 500 m from the target field.

Each porometer measurement is for only a small part of a single leaf on a plant, so a sampling strategy was implemented to obtain ET estimates relevant for estimating latent heat for the entire canopy. The plot was selected to be the second plot inside the northern boundary of field and is located in line with a ground control point so that the plot is easily located in UAS imagery. Within the 8-row plot, 2 central rows were selected to minimize edge effects. The length of each row was determined with a tape measure. Knowing the length of each row will allow for the selection of two equidistant sampling locations within the row. The strategy is to use the porometer to measure the top two leaves of a green and healthy plant at each point. Top leaves were selected as they will receive the most solar radiation compared with other leaves on the same plant. Since nadir images from the UAS were taken, these leaves are also visible to the camera more frequently than leaves farther down the plant stem. Consistent measurements between flight dates are taken at the same point in the same rows. Within a segment in a plot, four measurements were taken. As the growing season progresses, it sometimes became necessary to adjust the points and plants where measurements were taken to avoid measurements of damaged, unhealthy, or dying plants. Because of this, the row being sampled had to be changed one or two times (one in 2018 and two times in 2020) to avoid yellowing plants towards the end of the growing season. Additional measurements of soil temperature and canopy temperature were taken by handheld infrared thermometers (TG54 spot IR thermometer, FLIR Systems, Wilsonville, Oregon, USA); plant height and soil moisture

were also collected from tape measurements and water content sensor (CS 620, Campbell Scientific, Logan, Utah, USA). All these measurements were collected within the same segments where stomatal conductance was measured. LAI were measured by a LAI-2200C plant canopy analyzer (LI-COR Biosciences, Nebraska, USA). These supplemental data will be used as inputs for calculating latent heat flux. The stomatal conductance measurements were used as inputs for equation (3.39) to calculate ground reference latent heat flux, while the plant height and LAI are inputs for the TSEB model. Soil and canopy temperature are ancillary data used for the evaluation of UAS thermal temperature measurements.

TSEB Latent Heat Estimate Evaluation

Since locations of ground reference measurements in the plant canopy could not be recorded accurately enough to match the resolution of thermal imagery, measurements from the UAS imagery were extracted from multiple pixels representing the established sample area. The central point was based on the length of a row (about 4.8m) and the equidistant sampling points, then 3 extra pixels are selected in both vertical directions and 2 extra pixels in both horizonal directions to represent an area of 35 pixels (0.09 m^2 in real size with pixel size equals 0.05m) which incorporates the location where the ground measurements were made. The average and standard deviation of pixel values within this area were used to represent the modeled latent heat flux in the vicinity of the porometer measurements. Additional ancillary data, including air temperature, relative humidity, wind speed, solar radiation and 5-day precipitation totals, are used to assess the representativeness of latent heat flux values from all estimation methods based existing moisture conditions. The root mean squared error (RMSE) is used in the quantitively assess the uncertainty between the various latent heat estimation methods.

3.2.5 Image analysis workflow

The work flow for UAS based latent heat flux calculations is summarized in Figure 3.2. After the acquisition of the imagery, Pix4D mapper is used to generate mosaics for thermal and RGB images. The mosaics are then registered with each other in the ENVI software package (L3Harris Geospatial, Colorado, USA). Then areas of interest which could be plots or the entire field are extracted from the mosaics. Supervised classification is run on the RGB extractions to separate

canopy from soil and the resulting mask is applied to the corresponding thermal extractions to separate vegetation and soil. Only the pixels classified as vegetation are used for latent heat flux. Finally, results are evaluated versus independent measurements of latent heat flux.

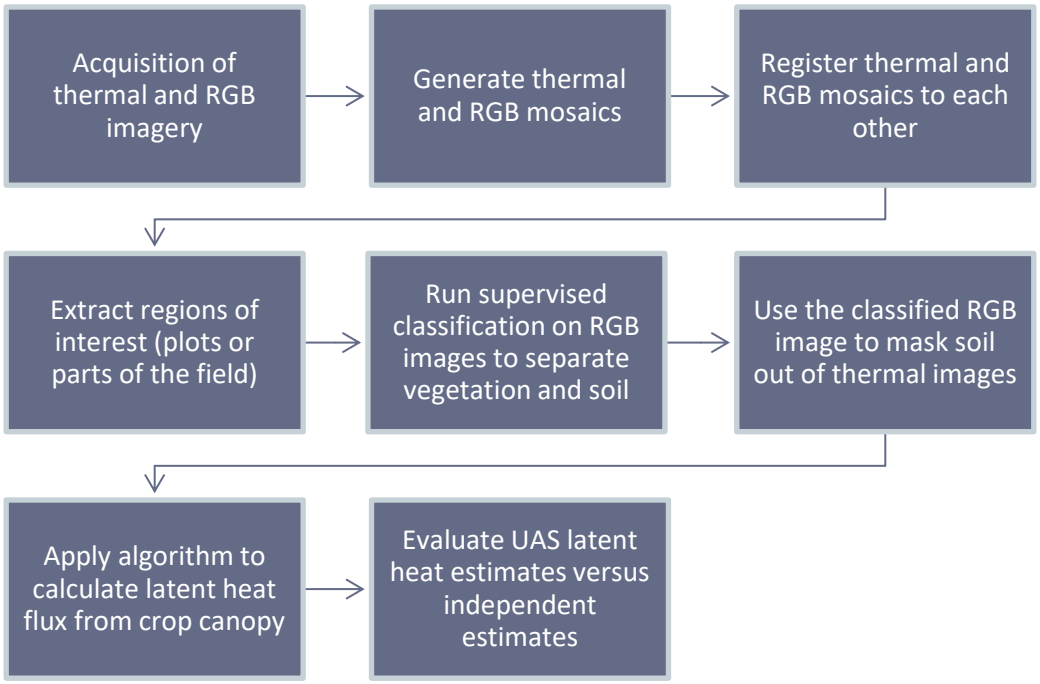

Figure 3.2. Latent heat flux calculations work flow

3.3 Results

3.3.1 Image registration accuracy

Image registration and classification accuracy have also been evaluated on a sample dataset. Because of the lower resolution and limited contrast in the thermal infrared imagery finding the ground control points deployed for georegistration around this field is difficult and their positions cannot be determined with the same degree of precision as in higher resolution imagery used on other flights. Four ground control points (GCPs) around the perimeter of the field (identified in Figure 3.3) are used to compute the RMSE of image coregistration between thermal and RGB imagery and that of x (horizontal) direction is 0.019 m and that of y (vertical) direction is 0.028 m. Additionally, image registration can be evaluated through visible inspection of image overlap as illustrated in Figure 3.3. From the Figure 3.3, it can be seen the individual segment and other

ground features from both field level and plot level registration align with each well. Further, the registration accuracy is evaluated by the ground control points.

Canopy classification accuracy

In order to separate the vegetation from soil, a supervised classification work flow was established in the ENVI software and applied to the RGB images. In order to demonstrate the accuracy of classification scheme, Figure 3.4 presents an example of the classification results for one plot in F54N and the classification accuracy results are summarized in Table 3.1.

The goal for this classification is to separate vegetation from soil pixels and only calculate the latent heat flux using those pixels identified as containing vegetation. While the method was applied to the entire experiment, results are demonstrated here using a single 8-row plot. In this example, there are three classes in the sample plot and the overall classification accuracy for all classes is above 96%. As the experimental field is captured using the same RGB camera under similar illumination conditions and over a short period of time (typically less than 20 minutes), we assume that application of the same classification method to the whole field will result in a similar classification accuracy. The same classification methodology was applied to RGB images for all flight dates.

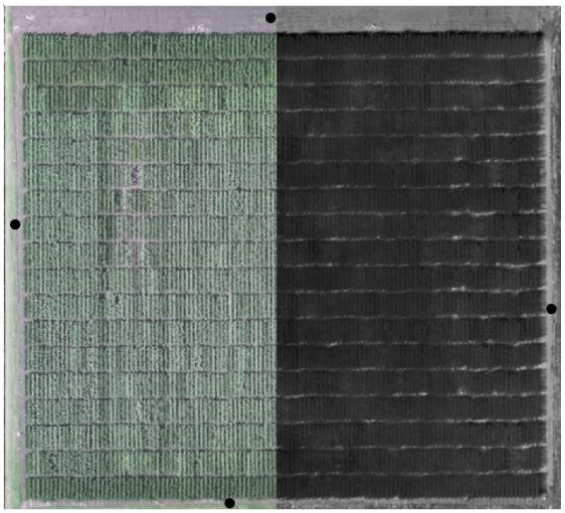

(a)

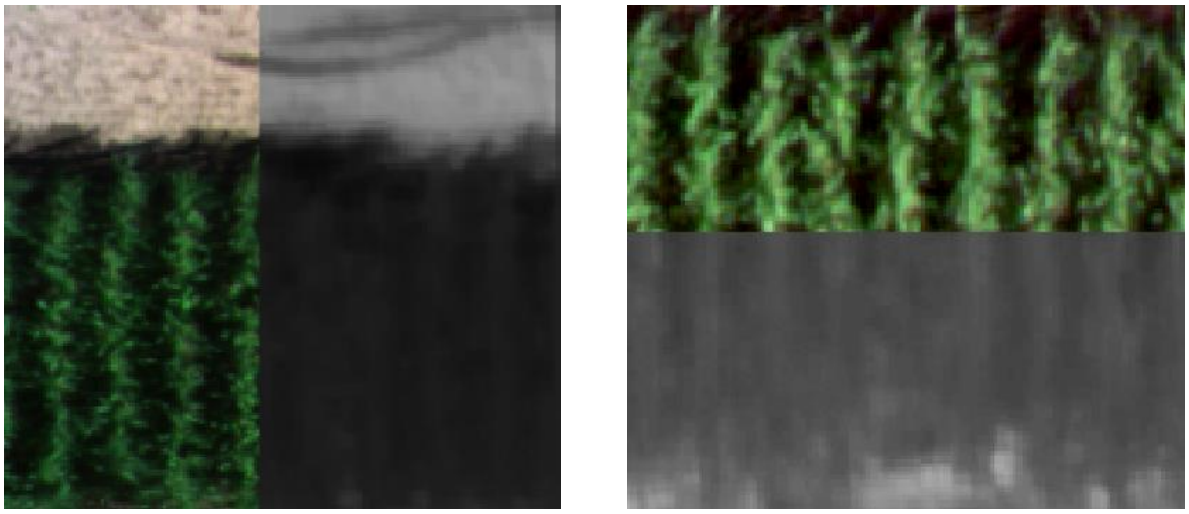

(b) (c)

Figure 3.3. Comparison of the registration between RGB (left) and thermal infrared (right) images taken on July 28, 2020. Both images were collected at the same time from the same camera during flight, but have slightly different fields of view and resolutions, so co-registration is required to remove any offsets. (a) field level registration with black dots indicate the GCPs used for registration accuracy evaluation; (b) plot level registration (vertical registration); (c) plot level registration (horizontal registration).

(a) (b) (c)

Figure 3.4. Supervised classification result of a plot in F54 north on July 28, 2020. (a) original RGB image; (b) original thermal image; (c) supervised classification result based on the RGB image.

Table 3.1. Classification results. Confusion matrix for classification evaluation including producer and user accuracy of three classes: Crop, Sunlit Soil and Shaded Soil is of a plot in F54N on July 28, 2020.

		Ground Reference				
	Class	Crop	Sunlit Soil	Shaded Soil	Row Total	User Accuracy
Predicted	Crop	107	0	2	109	98.17%
	Bright Soil	1	30	0	31	96.77%
	Shaded Soil	4	0	43	47	91.49%
	Column Total	112	30	45	187	
	Producer Accuracy	95.54%	100.00%	95.56%		Overall Accuracy 96.26%

3.3.2 Evaluation of TSEB model latent heat estimates

Porometer Based Latent Heat

Porometer measurements of stomatal conductance were collected for a total of in nine dates during the 2018 and 2020 field campaigns (Table 3.2) as described in the methods section. These measurements were used to estimate canopy transpiration, which in turn are compared with TSEB latent heat estimates for canopy pixels in the vicinity of the porometer measurements (Figure 3.5). The correlation between latent heat flux calculated from stomatal conductance measurements and that from the TSEB model is high with a R^2 higher than 0.90 and a low RMSE of 65.23 W/m^2.

When latent heat flux is less than 400 W/m^2, outputs from the model tend to overestimate the reference latent heat flux, while when the latent heat flux is over this threshold, outputs from the model underestimate the reference latent heat flux. The uncertainty of the model estimates is below 20 W/m^2 for most of the measurements, which indicates that the temperature is relatively uniform across an area consisting of about 35 pixels. The variability of model estimates is smaller than that from the porometer measurements. This is most likely because the model assumes weather parameters (solar radiation, wind speed, air temperature, humidity, etc.) and plant phenotypic traits (plant height) are the same within an 8-row plot and the only variable is the vegetative temperature measured by the UAS camera. The ground reference measurements are subject to microclimate effects as well as to the actual measurement locations within the canopy.

Penmen-Monteith Based Latent Heat

The Penmen-Monteith (PM) equation was also used to estimate the latent heat flux for the crop at the time of UAS flight operations using local weather observations. This results in a single value of LE for corn for the entire experiment, which can be compared against the distribution of LE that is calculated from the UAS imagery (Figure 3.6). For all dates in 2018 and 2020 included in the analysis, the Penmen-Monteith (PM) estimated latent heat is within the range of UAS estimated latent heat for the single plots where porometry measurements took place PM latent heat values are well below the median UAS estimated LE for all observations between 60 and 80 days after planting (DAP), while late season estimates August 31, 2018 (DAP 115) and August 28, 2020 (DAP 108) fall between the median and first quartile line for both years. Overall, both the UAS and PM estimated latent heat fluxes respond as expected to the growth stage with latent heat increasing in the early season, stabilizing, then dropping late in the growing season. The effect of growth stage on latent heat is best illustrated by comparing observations with similar weather and growth stage between the years of observation, for example July 12, 2018 (DAP 65) with a median latent heat flux of 561.58 W/m^2 and July 14, 2020 (DAP 63) of 556.47 W/m^2 as well as August 31, 2018 (DAP 115) of 300.16 W/m^2 and August 28, 2020 (DAP 108) of 292.11 W/m^2.

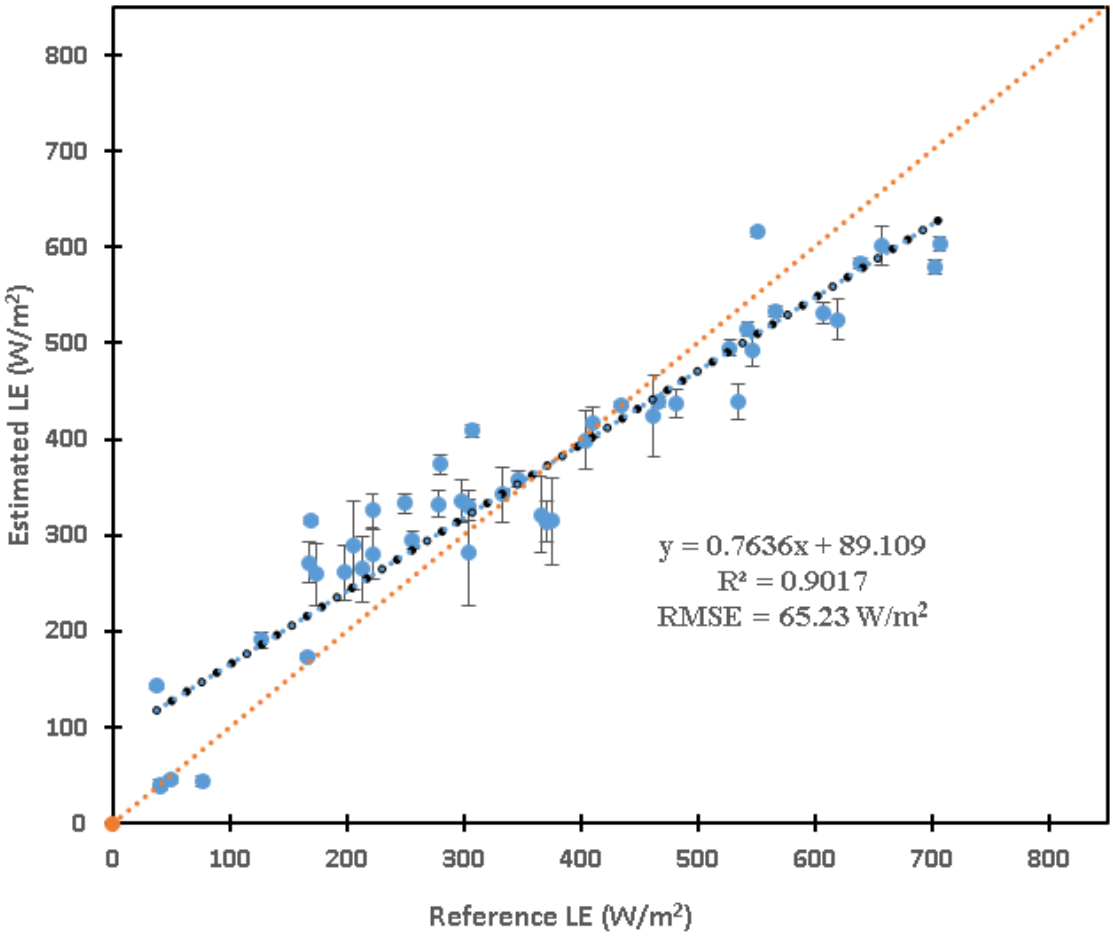

Figure 3.5. Scatter plot of reference latent heat flux calculated using porometer measurements versus TSEB model estimations. Symbol indicates the average value of measurements, while the error bars indicate the standard deviation of model estimates based on all pixels identified as potentially representing the location of the porometer measurements. Data is for all days of flight operations in 2018 and 2020.

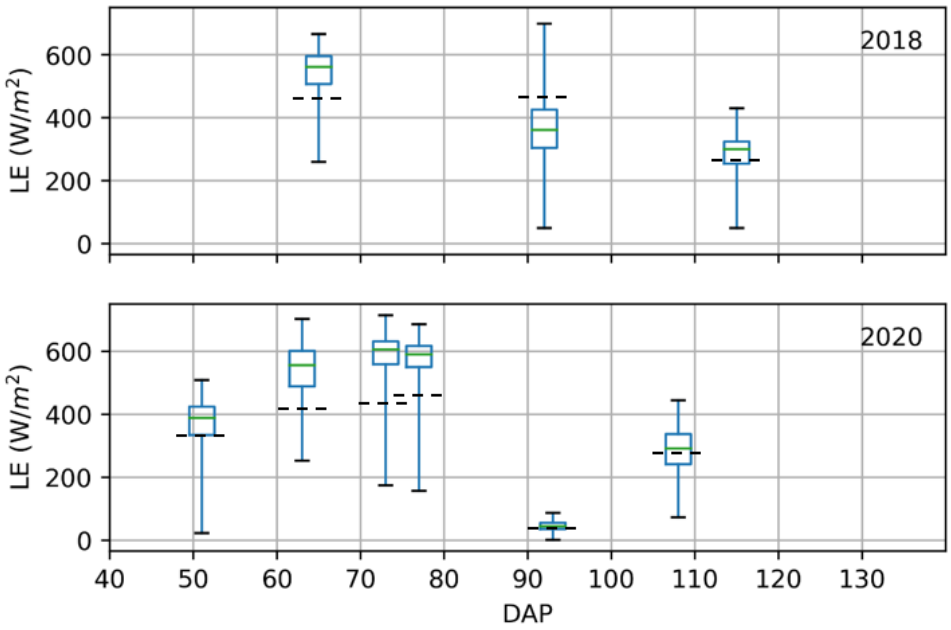

Figure 3.6. Box plots of latent heat flux distribution of model estimates within the sample area of target plots in Field 54 north, where the black dashed lines indicate the latent heat flux values calculated from the Penman-Monteith equation for the time of observation and top whisker indicates the highest LE values, the top of the box indicates the 25th percentile LE, the middle line indicates the median LE, the bottom of the box indicates that 75th percentile LE, and the lower whisker indicates the lowest values of LE. The x-axis is labeled based on the days after planting (DAP) which is specific to the year and field being evaluated.

Additional climate metrics are calculated (Table 3.2) and used to assess the role of real-time and antecedent environmental conditions on the estimated LE, with dates of special note described here in greater detail. The flight on August 13, 2020 (DAP 93) was especially late in the day (19:30) when the reduced incoming solar radiation (109.40 W/m^2) contributes to the closure of the stomata which results in the low latent heat flux (< 100 W/m^2). The 5-day accumulated rain prior to the flight was also found to be helpful in understanding observed latent heat fluxes, for example, in July, 2020, the incoming solar radiation is above 700 W/m^2 for all dates, however, the accumulated rain prior to the July 2 (DAP 51) flight was only 2.03 mm which is significantly lower than the rest of dates, which results in its overall latent heat flux (median just under 400 W/m^2) being amongst the lowest observed that in July 2020.

The PM estimated latent heat flux values are generally lower than those estimated using the TSEB method. That is because of the need for standardization and to be able to quantify ET for most conditions, the constants in the PM equation presume a constant surface resistance of 70 s/m during

all periods. This constant surface resistance which is equivalent to aerodynamic resistance in the TSEB model may cause some underprediction of hourly reference ET during some daytime periods when actual surface resistance may be somewhat lower (Allen et al., 1998).

Table 3.2. Weather parameters on the day of flight operations and the RMSE of latent heat estimated from the model for each flight date in 2018 and 2020.

Time	Air Temperature (^{0}C)	Wind Speed (m/s)	Relative Humidity (%)	Solar Radiation (W/m^2)	5-day Rain (mm)	DAP	RMSE (W/m^2)
2018/07/12 (16:00)	29.5	2.1	44.7	836.94	10.16	65	69.37
2018/08/08 (15:30)	28.5	4.7	57.7	699.17	24.13	92	63.03
2018/08/31 (17:00)	31.1	3.0	56.5	459.58	9.14	115	60.99
2020/07/02 (17:00)	31.1	3.6	40.9	705.00	2.03	51	71.82
2020/07/14 (16:30)	29.0	4.0	43.5	743.65	27.69	63	54.52
2020/07/24 (17:00)	28.9	2.2	49.1	731.64	15.49	73	70.08
2020/07/28 (17:00)	28.8	3.1	46.2	707.90	34.04	77	106.63
2020/08/13 (19:30)	26.6	2.7	64.5	109.40	20.32	93	16.76
2020/08/28 (16:30)	30.7	3.1	60.0	568.30	5.84	108	65.02

Change in Latent Heat through the Growing Season

The change in latent heat fluxes through the growing season shown in Figure 3.6 can also be visualized by looking at the spatial distribution of latent heat estimated at the plot scale (Figure 3.7). There is some increase in canopy closure through the first four dates in 2020, but the latent heat is estimated only for the leaf area in Figure 3.6, so the change in latent heat between days should be independent of the canopy area. As noted previously, the solar radiation between the first four measurements dates in 2020 (Figure 3.7a-d) is very similar (between 705 and 744 W/m^2) but latent heat flux is low on July 6th (DAP 51; Figure 3.7a). In this case, most of the other environmental factors are similar, the biggest difference is the total rainfall over the previous 5 days, which was very low (2.03 mm) compared to the next three days which had precipitation

totals of 27.69, 15.49 and 34.04 mm, respectively. This suggests that the target plot was under greater water stress on the first date of observation, than on the subsequent ones.

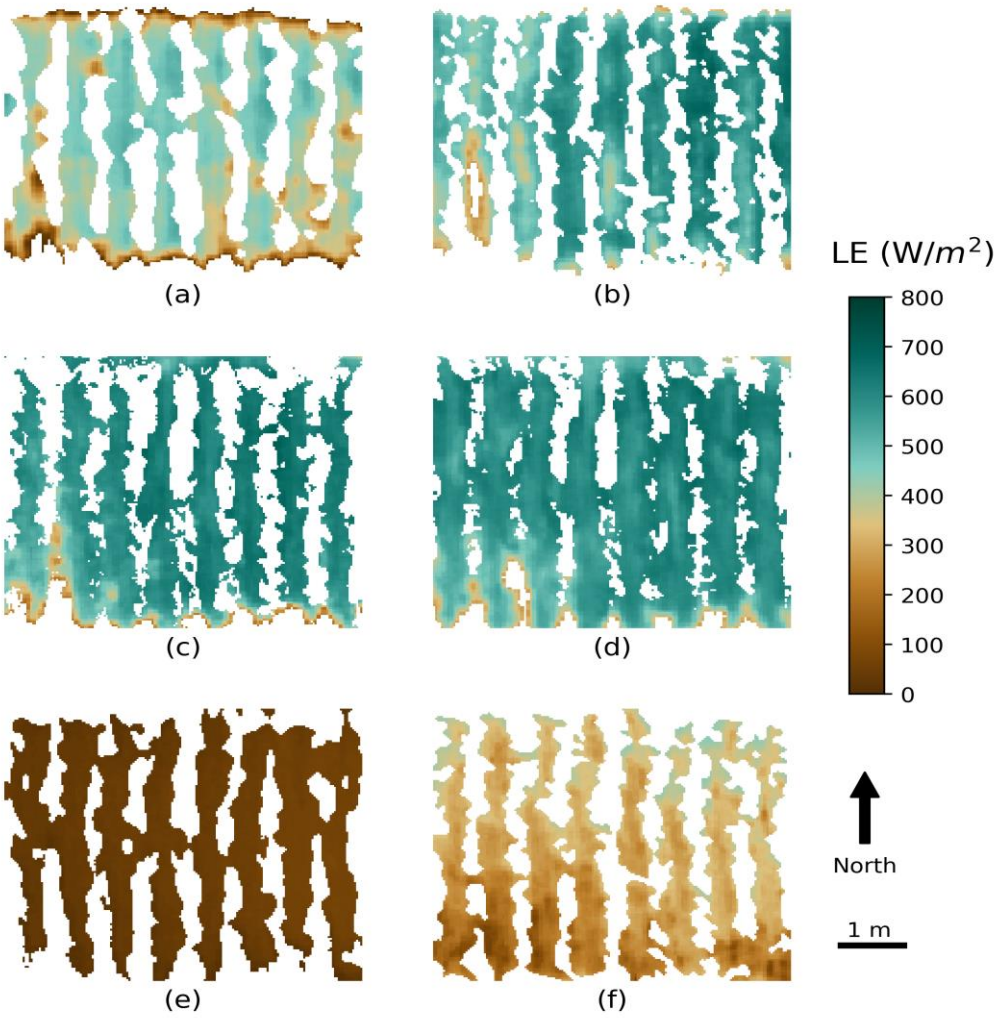

Figure 3.7. Latent heat flux estimates for the target plot in F54 north of six different dates. (a) July 2, 2020 (DAP 51); (b) July 14, 2020 (DAP 63); (c) July 24, 2020 (DAP 73); (d) July 28, 2020 (DAP 77); (e) August 13, 2020 (DAP 93); (f) August 28, 2020 (DAP 108). Images are clipped so latent heat flux is estimated only for canopy pixels.

Measurements on August 13, 2020 (Figure 3.7e) are later in the growing season, but not late enough that a substantial drop in latent heat flux would be expected. Air temperature, wind speed and rainfall are comparable with other sampling dates. The humidity is higher and the incoming solar radiation is lower than all other observations dates. While the higher humidity likely helps constrain latent heat, the bigger factor is the reduced solar radiation. Flights on that day occurred

much later in the day, at 19:30 local time, and latent heat is severely limited by the incoming solar radiation that is only 109.4 W/m^2.

The final flight date of the 2020 season on August 28 (DAP 108) also found consistently low latent heat fluxes across the plot (Figure 3.6f). Flight time is again in-line with the earlier dates, as are temperature, wind speed and antecedent precipitation. Humidity is still higher, while solar radiation is still lower than found in the July flights. Lower latent heat estimates are consistent with the lower solar radiation, but the crop is also nearing senesce which would also reduce latent heat.

It can also be seen from Table 3.2 that the range of RMSE is from 16.76 to 106.63 W/m^2. The lowest RMSE appear on August 13, 2020 when there is low solar radiation and low latent heat flux in general; the highest RMSE however happened on July 28, 2020 when the latent heat flux is one of the highest among all dates in 2020. This is in consistent with the findings in Figure 3.5 which indicates the largest errors occur when the reference latent heat flux is low or high. On July 2, 2020, since there was a water deficit stress, the soil temperature was consistently higher than the canopy temperature measured. That is visualized in the Figure 3.7 (a) in which the northern and southern parts of the vegetative plots have obviously lower latent heat flux compared with the other parts of the plots. That is because soil of high temperature emits radiation that heats the leaves. Leaves of high temperature are considered to have less latent heat flux.

Latent heat flux of the entire field

A latent heat flux map of an entire field (Figure 3.8) has been generated to demonstrate the ability of the workflow to provide information at a larger scale. This map shows that for a large part of the field, the latent heat flux is above 400 W/m^2 with the lowest latent heat fluxes concentrated at the ends of field plots. The area around 20 m east and 50 m north is mostly devoid of latent heat flux estimates because the crops in this area are not well developed. The area of relatively consistent high latent heat between 0 and 15 m east and 40 to 80 m north is a single experiment with more consistent genetics. The full field is subdivided into three breeding experiments in the east, middle and west parts of the field with border rows of a commercial variety (same genetics) between them and between the experiments and the field edges. The central experiment is also

visible as an area with more consistent high latent heat flux. In general, the field on this day is not under water stress which is consistent with the weather conditions listed in Table 3.2. The plot identified in the figure is the same plot as in Figure 3.7(d).

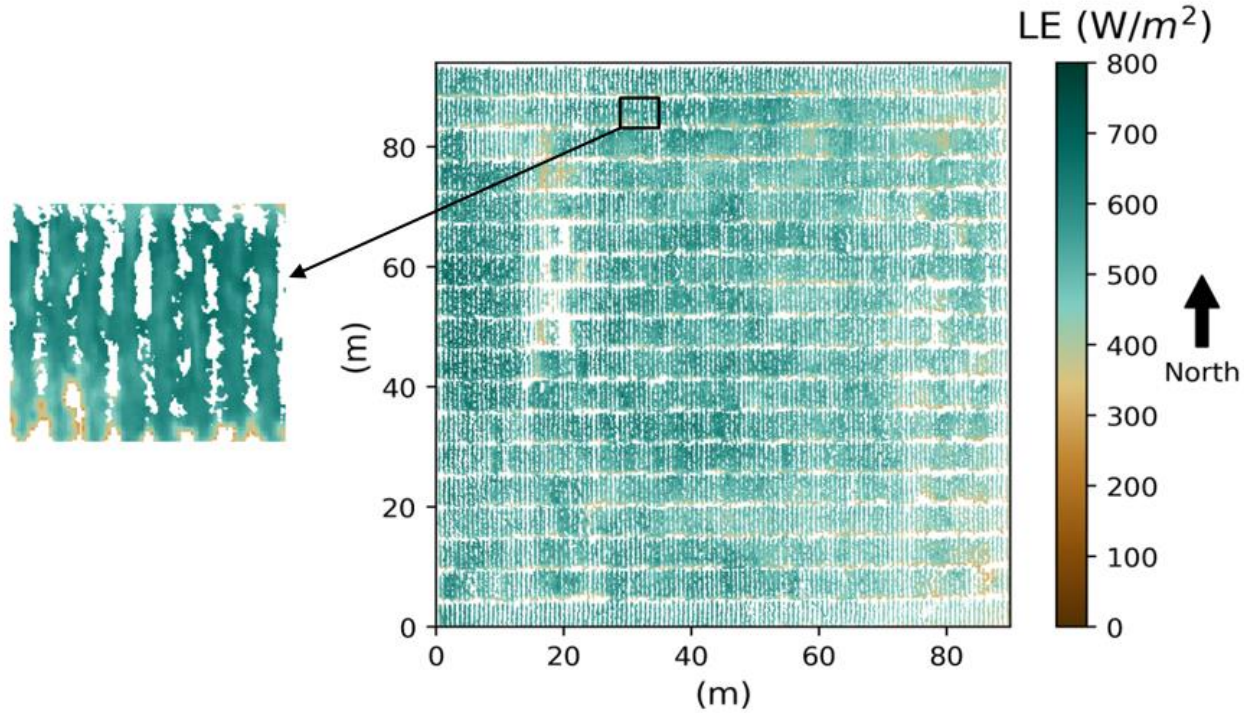

Figure 3.8. Latent heat flux map of field 54 north on July 28,2020 with a zoomed in picture showing the plot in detail.

3.4 Discussion

Remote sensing platforms with thermal infrared sensors have been used for quantifying the water status of crops for many years but interest has been growing in recent years with the increased availability of inexpensive thermal infrared cameras mounted on UAS platforms. Obtaining accurate canopy and soil temperature measurements from such systems was addressed in Chapter 2, while this chapter focuses on the estimation of latent heat flux from the crop canopy using thermal infrared imagery and local weather observations. Traditional work flows for latent heat estimation were designed for coarser resolution datasets collected from satellite or aircraft systems that cannot distinguish between vegetation and soil. Latent heat estimation methods from such datasets must deal with errors and uncertainty introduced into the latent heat estimates from the

mixture of soil and vegetation in the remote sensing imagery. This study presents a novel work flow for crop latent heat flux quantification from high-resolution (around 5 cm per pixel) imagery, in which RGB imagery was used to distinguish between vegetation and soil by supervised classification and then used to mask thermal imagery so that only canopy pixels were included in the latent heat calculations. As with the two-source energy balance (TSEB) model on which it is based, the method made use of two atmospheric stability scenarios where the relative temperature of the canopy to the air was used to determine if conditions were stable and unstable which affects the estimation of latent heat flux.

For latent heat flux estimation from the TSEB model, Benner et al (2017) reported a RMSE (root mean square error) of 69 W/m^2 which is higher than the RMSE reported here. Riveros-Burgos et al. (2021) reported a RMSE and MAE values of 37 and 27 W/m^2 for latent heat flux estimations using a clumped model to directly estimate LE over discontinuous canopies in an olive orchard. However, the flights starting time varied from 12:39 to 14:17 and the LE range is from 100 to 220 W/m^2, which makes increase their estimation accuracy because only low latent heat flux conditions were considered.

Similarly, Ortega-Farías et al. (2016) reported the RMSE and mean absolute error (MAE) values for LE are 50 and 43 W/m^2 using energy balance algorithm over a drip-irrigated olive orchard. The flight time is constrained between 11:56 to 12:46 local time and the incoming solar radiation is from 801 to 901 W/m^2.

Nieto et al. (2019) used four different TSEB approaches to estimate the component soil and canopy temperatures and ET partitioning between soil and canopy. Thirteen data acquisition flights were conducted from 2014 and 2016. They were using an empirical NDVI threshold to differentiate between canopy and soil to retrieve soil and canopy temperatures separately. The pixel resolution for their visible and near-infrared datasets are 0.15 m and 0.6 m respectively. They estimated the RMSE range of latent heat flux estimates is from 49 to 75 W/m^2 for the four approaches used in their research.

The accuracy reported here is sufficient to estimate the instantons latent heat flux with an average of RMSE is 65.23 W/m^2 which is within the range achieved ny other researchers. Challenges

remain for the testing of algorithm for more types of crops and a variety of atmospheric conditions. Also, the latent heat flux acquired here is on a pixel level, how to reduce the information to provide a value for a plant and a plot accurately will need to be investigated in the future.

3.5 Conclusion

A workflow was presented to estimate the latent heat flux of row crops from a UAS-based thermal and RGB camera system. The main part of the workflow is to use a modified TSEB model to calculate the values of canopy latent heat on a pixel level. The workflow developed here requires high resolution RGB and thermal imagery from a single camera, and a variety of weather parameters collected locally. The RGB data is classified into canopy and soil and used to mask the thermal imagery to extract canopy temperature that are then used to calculate latent heat flux from a field experiment with corn being planted in.

The latent heat estimates are evaluated against ground reference measurements using both in-situ porometer measurements and calculating latent heat using the Penmen-Monteith method using local weather conditions. When comparing with the ground reference data calculated from porometer measurements, the RMSE for between latent heat estimated using UAS imagery and porometer surveys for nine flight dates in 2018 and 2020 is 65.23 W/m^2 with a coefficient of determination (R^2) that is above 0.9. The results indicate that the workflow developed here is suitable for using high resolution thermal imagery to calculate latent heat flux of corn accurately.

Future work includes testing the performance of this workflow on more types of crops and also to develop an appropriate way to account for the variance of latent heat flux on different parts of leaves, for example differences in LE estimation from sunlit and shaded leaves, even on the same plant.

Best estimation results were achieved in cloudless weather conditions when solar radiation did not change abruptly. When there were intense clouds in the sky, solar radiation could change dramatically which bring in huge errors to the estimation results. It is also observed that when the solar radiation is higher, there is a stronger linear relationship between estimated latent heat flux

and reference latent heat flux, which indicated the performance of the model is more robust under high incoming solar radiation conditions.

However, the root mean square error is large when the reference LE is low or high in some extreme situations. In the end, through the calibrations, we are still able to achieve reasonable results.

4. A NEW WATER DEFICIT STRESS INDEX DERIVED FROM THERMAL IMAGERY

Abstract

Crop water deficit stress is a deficiency in water supply, detected as a reduction in soil water content or from the physiological responses of the plant to that lack of sufficient water. Many methods are used to monitor the crop water stress level, including those based on the soil water balance, plant-based approaches and remote sensing approaches. Since remote sensing approaches can offer water status information at a large geospatial scale (such as on a field or farm level) in a short period of time at relatively low costs, this method has gained more attention in recent years. However, the current water stress index calculation usually requires extra experiments that make it more difficult to implement operationally. In this research, the Bowen ratio is assessed as a metric for water deficit stress quantification. Very high- resolution thermal datasets (0.05 m) and corresponding RGB datasets (0.03 m) were used as inputs for the index calculation. The RGB datasets were used for supervised classification of soil and vegetation, the classification results were then used to filter the thermal mosaics to separate vegetation and soil temperatures, then the vegetation temperature is used for calculating the Bowen ratio. Finally, the results are validated against three measures of water stress: the soil moisture index (SMI), crop water stress index (CWSI), stomatal conductance. Several spectral indices derived from multi-spectral images and commonly used to assess crop stress are also evaluated against the measures of water stress. The objective of this research is to assess the potential for the Bowen ratio to be used as a measure of crop water stress. Data from nine dates in 2018 and 2020 have been evaluated and the coefficient of determination (R^2) of Bowen ratio and SWI, CWSI and stomatal conductance are all above 0.73. The results indicate that the Bowen ratio can be used as an alternative for the well-known CWSI.

4.1 Introduction

Irrigated agriculture is essential to global food production, utilizing only 20% of cultivated land to provide 40% of the world's food supply (Garces-Restrepo et al., 2007). Meanwhile, the irrigation of agricultural crops accounts for 80 percent of the US's water consumption. Faced with the need to increase global food production in the face of increasing climate variability, agriculture needs

new tools to improve crop water management (Behmann et al., 2014), and this requires a deeper understanding of plant response to water stresses (Ihuoma and Madramootoo, 2017).

Water stress may arise as a result of two extreme conditions either an excess of water or a deficit of water. Most work on crop water stress has focused on water-deficit stress also known as drought stress (Mahajan and Tuteja, 2005). Crop water deficit stress is a deficiency in water supply, detected as a reduction in soil water content or from the physiological responses of the plant to the lack of sufficient water. In response to a water deficit stress, ion- and water-transport systems within the pant function to control turgor pressure changes in guard cells and stimulate stomatal closure to minimize water loss to the environment. This results in a decrease in CO_2 absorption which in turn impacts photosynthesis and plant growth (Osakabe et al., 2014). Wang et al. (2015) indicated that water stressed crops have reduced transpiration, increased leaf temperature and manifest other symptoms such as leaf wilting, stunted growth, and leaf area reduction. Also, water stress impedes photosynthesis adversely affects the physiological and nutritional development of crops, leading to reduced biomass, yield, and quality of crops (Aladenola and Madramootoo, 2014; Rossini et al., 2013; Zhang et al., 2017a, 2017b; Katsoulas et al., 2016), which is detectable with multispectral remote sensing.

There are several ways to monitor plant water stress level: soil water measurements coupled with soil water balance approaches that indicate the deficit in available moisture often used for planning irrigation; plant-based approaches that include measurements of stomatal conductance, leaf and stem water potential, relative water content measurement, sap flow and stem and fruit diameter measurement; and finally remote sensing approaches including infrared thermometry and spectral vegetation indices (Ihuoma and Madramootoo, 2017). Although the first two approaches can provide relatively accurate estimation of soil and plant water status, they are usually labor intensive, time consuming and can only offer point measurements (information for a leaf or a plant). This can be a problem if field or larger scale information is required. Remote sensing technologies can offer information at those large scales in a rapid and non-destructive fashion. Remote sensing techniques have gained more attention in recent years with the growing availability of inexpensive thermal infrared and multispectral cameras mounted to unmanned

aircraft systems (UAS). This has in turn facilitated an interest in remote sensing technologies as a method to detect water stress across fields and in near-real time.

Within the sphere of remote sensing methods, there are two specific methods for detecting water stress: Infrared thermometry and spectral vegetation indices. Canopy temperature has long been recognized as an indicator for crop water stress (Jackson et al., 1981; Idso et al., 1981; Jackson et al., 1988). If the crops do not have access to enough water to support optimal growth, stomata will close and the transpiration rate will decrease which results in an increase of canopy temperature as the plant's ability to regulate its temperature is compromised. In order to quantify crop's water stress level, researchers have developed a Crop Water Stress Index (CWSI) (Jackson et al., 1981; Idso et al., 1981; Jackson et al., 1988). The CWSI is derived from canopy temperature and has been adopted as a tool to indicate plant water status and schedule irrigation in the production of many crops (Aladenola and Madramootoo, 2014; Alchanatis et al., 2010; Bellvert et al., 2016; Yildirim et al., 2012). CWSI theory is based on the principle that transpiration cools the leaf surface and as root zone soil moisture is depleted, stomatal conductance and transpiration decrease and leaf temperature increases. The concept of using CWSI for improving irrigation scheduling gained popularity when Idso et al. (1981) observed a linear relationship between canopy temperatures measured using infrared thermometry and air temperature difference and vapor pressure deficit. They used that relationship to develop an empirical method of quantifying crop water stress that takes canopy temperature and ambient meteorological conditions (e.g., net radiation, vapor pressure deficit and wind speed) into consideration.

The use of remotely sensed spectral indices relies on the fact that stressed plants undergo physiological changes that can affect their coloration. Plant leaves absorb the majority of radiance in the visible band through plant pigments located in mesophyll such as chlorophyll and xanthophylls but are highly reflective in the near-infrared (NIR) part of the spectrum. In addition, water content in sponge cavities as well as carbon content in different forms (sugar, starch, cellulose and lignin) within mesophyll cells affect leaf spectral properties. Although canopy temperature may be a direct indicator of canopy transpiration, it does not account for all other physiological changes to plants under water stress such as photosynthetic pigment changes

(occurring to chlorophyll, carotenoids, and xanthophylls) and non-stomatal reductions of photosynthesis.

Due to the ability to detect physiological changes such as photosynthetic pigment changes or non-stomatal reductions of photosynthesis under water stress conditions, spectral vegetation indices such as the Photochemical Reflectance Index (PRI), the Normalized Difference Vegetation Index (NDVI), the Red-edge ratio (REI), the Green Red Vegetation Index (GRVI), the ratio of Transformed Chlorophyll in Reflectance Index (TCARI) to Optimized Soil-adjusted Vegetation Index (OSAVI), Optimized Soil Adjusted Vegetation Index (OSAVI), the Water Index (WI), WI/NDVI, and Normalized Water Index (NWI) have all been investigated for predicting plant water status. (Ihuoma and Madramootoo, 2017; Katsoulas et al., 2016; Suárez et al., 2008; Baluja et al., 2012; Ballester et al., 2019).

Because thermal and visible remote sensing imagery can capture different physiological changes in water stressed crops there is a need for improved methodologies to integrate both methods into a more holistic water stress assessment. Temperature-derived indicators would underestimate the net effect of severe water stress on biomass accumulation and growth and thus, a water stress index that is sensitive to both photosynthetic rates as well as to transpiration may be advantageous.

As water stress can damage crops, successful detection is helpful for irrigation scheduling and other management practices. Recently, Berni et al. (2009a) applied models based on canopy temperature estimated from high resolution airborne imagery to calculate tree canopy conductance and the crop water stress index (CWSI) of heterogeneous olive orchards. Baluja et al. (2012) assessed the water status variability of a rain-fed vineyard by thermal and multispectral imagery using an unmanned aircraft system (UAS). They found that strong correlations exist between stem water potential, stomatal conductance and various thermal and spectral indices. They further concluded that the relationship with thermal imagery and derived indices can be considered as a short-term response of the plant water status situation, while spectral vegetation indices are probably the result of cumulative water deficits. Espinoza et al. (2017) assessed the performance of multispectral and thermal remote sensing on water stress detection in subsurface irrigated grapevines with deficit and full irrigation. The data exhibited a relationship between remote sensing (spectral indices and canopy temperature) and response variables (stomatal conductance

and crop yield). However, one problem in using canopy temperature alone is that it ignores the air temperature, which is an important factor affecting latent heat fluxes and is incorporated in the CWSI calculation.

In their current form both thermal and spectral based water stress indicators have multiple limitations. The two standard forms of the temperature based CWSI algorithm require inputs of potential evapotranspiration, lower and upper limit of canopy temperature and air temperature difference, which is a significant number of measurements for each application. Meanwhile, the spectral indices are in fact sensitive to all forms of plant stress, not just water stress, as other biotic and abiotic stresses will result in similar physiological phenomenon. Additionally, researchers have found it difficult to select a single vegetation index for precise estimation of plant water status (Ihuoma and Madramootoo, 2019) as indices are sensitive to different parts of the electromagnetic spectrum and physiological changes to various plants do not affect their spectral signatures uniformly. Taking all these factors into consideration, a straightforward and direct indictor is needed for crop water stress estimation, so here we propose to make use of the Bowen ratio (Bowen, 1926).

The Bowen ratio (Bowen, 1926) was firstly proposed to quantify the ratio of heat losses by conduction and evaporation from any water surface. Heilman and Brittin (1989) and Wright et al. (1993) first introduced the Bowen ration as a method for latent heat flux calculation. In this research, Bowen Ratio, which is the ratio of sensible heat flux to latent heat flux, is proposed as a more robust and easier to calculate indicator of crop water stress. Compared with the thermal and multispectral indicators mentioned previously, it relies on solar radiation, wind speed, relative humidity, canopy temperature which can be easily acquired from a nearby weather station and a thermal camera mounted on a UAS into consideration and it can be calculated easier than the CWSI. In this chapter, the Bowen ratio is evaluated as a potential method for quantifying crop water stress by comparing it with measures of water stress and other well-known spectral water stress indicators including the REI, OSAVI and GRVI.

4.2 Methods

4.2.1 Field site

Figure 4.1. Location of the research field with respect to the main farm buildings at ACRE (left), and an image of the field experiment being studied showing the north-south orientation of plot rows and the JCEager experiment boundaries (right).

Data was collected in the summers of 2018 and 2020. All of the flights took place at the Agronomy Center for Research and Education (ACRE) managed by the Department of Agronomy at Purdue University. A single field experiment, hereafter referred to as “Field 54N” or “F54N” (40°28'43.8"N, 86°59'23.2"W) (Figure 4.1) is the target field for all flights. This field is about 0.9 hectares and was set up to support breeding experiments, with one or more experiments in corn or sorghum breeding established in the field every other year. For this study, each experiment consists of hundreds to thousands of smaller plots with different specific genotypes of corn as part of a breeding experiment. Within each plot, there are two replicate rows with the same genetics. The field was planted in from north to south and east to west, with rows running north to south. The field is planted in other crops, typically soybeans, in the off year.

4.2.2 Remote sensing data acquisition and processing:

Unmanned Aircraft System (UAS)

The unmanned aircraft system was built based on the DJI M600 platform and has one thermal sensing system and a multispectral camera mounted on its underside. The thermal sensing system consists of a ThermalCapture Fusion Zoom camera (TeAx, Germany) which has two sensors: a thermal infrared and a visible-light imager. The thermal imager has a resolution of 640×512 and a focal length of 19 mm with a field of view 32°× 26°. The thermal imager is sensitive to spectral wavelengths from 7.5 to 13.5μm and its measurement accuracy is ±5°C or 5% of reading in its operating temperature range (-20°C to +50°C). The thermal imager has been calibrated in the lab using methods described in (Zhu and Cherkauer, 2021). The visible-light imager has a resolution of 1920×1080.

The multispectral camera, a Rededge MX camera (MicaSense, Inc, Seattle, Washington) has a resolution of 1280×960 and a focal length of 5.4 mm, was mounted on the same platform. It has 5 spectral bands: blue (475 nm center, 32 nm bandwidth), green (560 nm center, 27 nm bandwidth), red (668 nm center, 14 nm bandwidth), red edge (717 nm center, 12 nm bandwidth), near-infrared (NIR; 842 nm center, 57 nm bandwidth).

Flight operations

The dual thermal and visible spectrum camera was mounted with a gimbal so that nadir images were always collected during flights. The RedEdge camera was mounted on the underside of the UAS in a fixed position so that it captured nadir images during most flight operations. Flights were conducted at an altitude of 60 m so that the ground sampling distance is about 5.4 cm per pixel for the thermal camera, 3.3 cm per pixel for the visible camera and 4.2 cm per pixel for all bands of the multispectral camera. The air speed of the UAS was 7.5 m/s and the spacing between flight paths was set to be 6.8 m to achieve a frontal overlap of 95% and a side overlap of 80% for thermal images and 81% frontal overlap and 87% side overlap for multispectral images. The camera takes fast still images at a frame rate of 5 fps and the multispectral camera only takes one image per second. A software named ThermoViewer (TeAx, Germany) is used for extracting thermal and RGB frames from the video. Most of the flights were conducted in the afternoon

around 2-4 pm to provide stable temperature conditions. Water targets were deployed at the edge of the field and were flew over both at the beginning and end of the fields to provide radiometric calibration for the thermal imagery see Zhu and Cherkauer (2021) for details of the process.

Spectral panels with reflectance of 7%, 12%, 22%, 36%, 48% from Tetracam (Tetracam Inc. Chatsworth, CA) were used for radiometric calibration. They are deployed in the field prior to flight operations in a location where they were viewed multiple times during the flight. Ground control points are deployed around the field to facilitate the generation of mosaics and registration as well as for pixel position accuracy validation.

Image processing

Pix4D Mapper software was used for creating mosaics for both thermal and multispectral datasets by using common tie-points between overlapping images to reconstruct the 3-D land surface and create a flat, geometrically aligned, merged image. The mosaic is then radiometrically calibrated using the spectral panels and water temperature targets for multispectral and thermal imagery, respectively. A composite RGB image is then generated from red, green and blue bands from the multispectral camera using layer stacking. After that RGB and thermal mosaics were registered in ENVI (L3Harris Geospatial, Colorado, USA) using ground control points deployed around the field. An area of any size usually in the shape of rectangle within the field can be selected, and a plot extraction algorithm (Ribera et al., 2017) developed from Purdue University was applied to acquire corner pixel coordinates of each individual row within this area. The imagery was then separated into pixels representing the plant canopy and soil using a supervised classification. The classification algorithm was implemented in ENVI software and training data of three classes: Dark soil, bright soil and vegetation was selected before running the program. The result is stored as a mask which has each class represented by a number and only the vegetation will be used for later calculations and all the dark and bright soil pixels will be filtered out. The classification results together with the plot extraction results which are the corner coordinates of each individual row were used as inputs in a python-based program to calculate vegetation spectral and thermal indices on a row level.

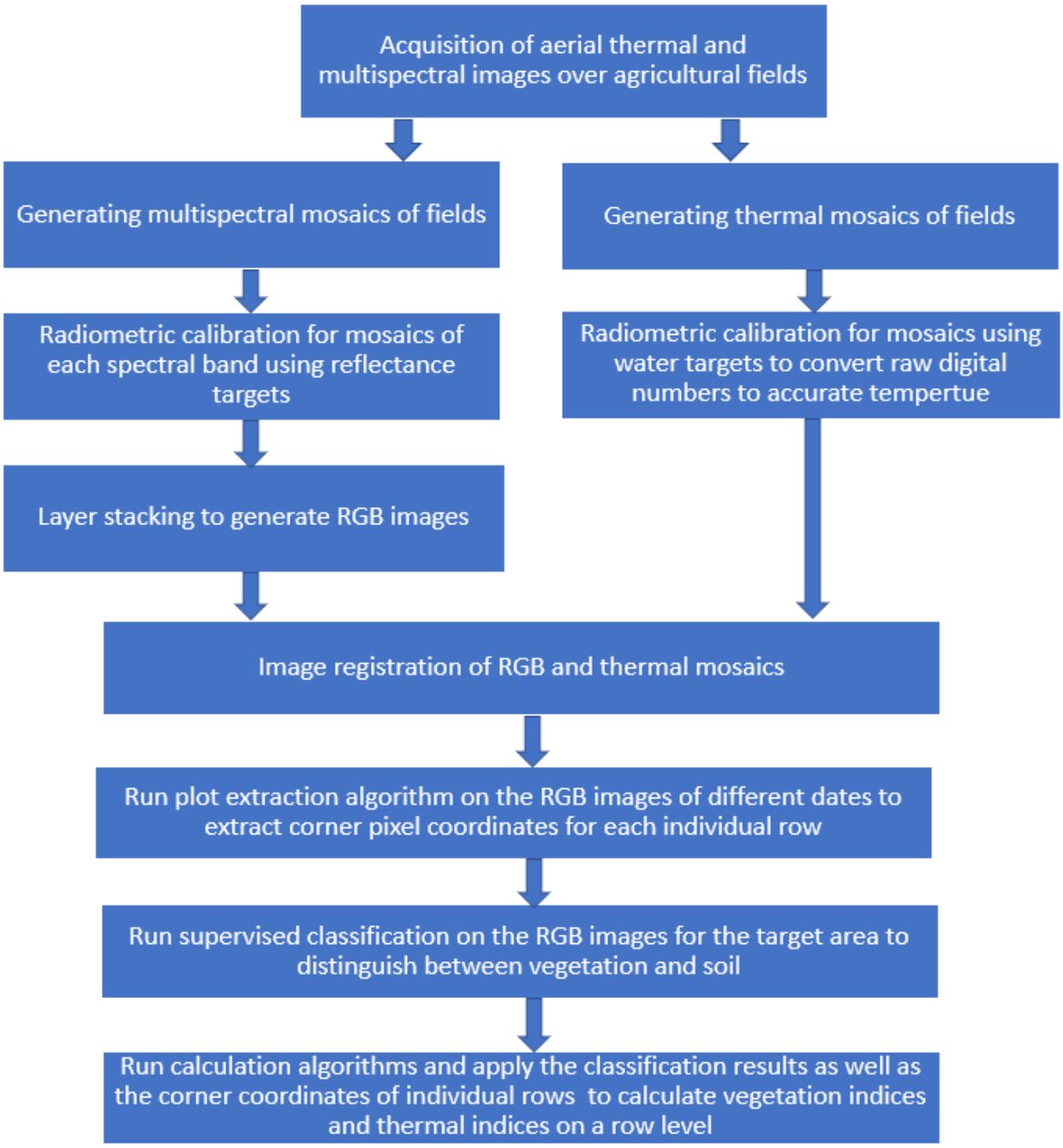

Figure 4.2. Flow chart illustrating the data processing and analysis pipeline developed for calculating the thermal and vegetation Indices.

4.2.3 Remote sensing derived water stress indices

Thermal indices calculation:

Two water stress indices will be computed from the thermal UAS data. The first is the CWSI (Crop water stress index) which is defined as (Equation 4.1) (Jackson et al., 1981):

$$CWSI = 1 - \frac{E}{E_P} = \frac{[(T_c - T_a) - (T_{nws} - T_a)]}{[(T_{dry} - T_a) - (T_{nws} - T_a)]} \quad (4.1)$$

Where E is the evapotranspiration, E_P is the potential evapotranspiration, T_c is the canopy temperature (°C), T_a is the air temperature (°C), T_{dry} is the water stressed canopy temperature (°C), T_{nws} is the non-water stressed canopy temperature (°C).

The second index is based on the Bowen Ratio, defined as (Equation 4.2):

$$B = \frac{H}{LE} \quad (4.2)$$

In which, H is the sensible heat flux and LE is the latent heat flux. The latent and sensible heat fluxes are calculated from thermal infrared imagery as described in Chapter 3.

Bowen ratio can be positive or negative depending on the direction of sensible heat flux (Equation 3.36) as latent heat will always be positive. Negative sensible heat flux occurs when the canopy is cooler than the surrounding air, so sensible heat flux is from the air to the leaf. During peak afternoon air temperatures, a plant with sufficient water can maintain a cooler canopy temperature through transpiration. Thus, negative values of the Bowen ratio indicate that there is no water deficit stress.

For this study, the range of Bowen ratio is limited to values greater than 0 where values from 0-1 indicates minor water stress, from 1 to 3 indicate moderate water stress and values of 3 or higher indicate severe water stress. This index will be calculated on pixel level (one Bowen ratio value for each pixel of the source image) and plot level (one Bowen ratio value for each experimental plot calculated by averaging all pixel values within the plot).

Multispectral spectral indices:

The sensitivity of the normalized difference vegetation index (NDVI) to soil background and atmospheric effects has generated an increasing interest in the development of new indices, such as the Optimized Soil Adjusted Vegetation Index (OSAVI) (Rondeaux, Steven and Baret, 1996), to minimize soil influences on canopy spectra by incorporating a soil adjustment factor into the denominator of the normalized difference vegetation index (NDVI) equation. The OSAVI is calculated as (Equation 4.4):

$$OSAVI = \frac{(1+0.16)\times(NIR-R)}{(NIR+R)+0.16} \quad (4.4)$$

In which, R and NIR represent the reflectance in the red and near infrared parts of the spectrum. The constant 0.16 is designed to correct for the mixing of soil with canopy in the image pixel.

The Green-Red Vegetation Index (GRVI) and the Red-Edge index (REI) are also assessed as they have been identified as being responsive to plants experiencing a mild level of water stress (Ballester et al., 2019) and use different spectral bands from the indices derived from NDVI. These indices are calculated using the following equations (Equation 4.5 and 4.6).

$$GRVI = \frac{G-R}{G+R} \quad (4.5)$$

$$REI = \frac{RE}{R} \quad (4.6)$$

In which, RE, R, and G represent the reflectance in the red edge. red and green spectral bands. All of these indices are design for use with wide-band multi-spectral cameras. Indices requiring the use of narrow-band or hyperspectral sensors are not evaluated.

These three vegetation indices have been found to be correlated with water deficit stress (Ihuoma and Madramootoo, 2019). For this analysis, the spectral indices are calculated only for pixels classified as vegetation. Then all values within 2 rows of the same genotype are averaged to yield a single vegetation index representing the two row plots. For all of these indices higher values indicate that the crop is less likely to be experiencing water stress.

Environmental measurements of water stress weather data collection:

An automatic meteorological station is located about 500 m southwest of F54N. The station records air temperature, relative humidity, solar radiation, precipitation, and wind speed at 30-minute intervals. These data were used to calculate the hourly reference latent heat flux according to the Penman-Monteith (PM) model (Allen et al., 1998) and are also used as inputs to calculate the latent heat flux and CWSI.

Soil Moisture Index (SMI):

The soil moisture index is defined as:

$$\text{SMI} = [\frac{5(SM-WP)}{(FC-WP)} - 5] \tag{4.7}$$

In which, SM is the soil moisture content; WP is the wilting point; FC is the field capacity. The field capacity is determined from the lab results of soil water retention curve from National Cooperative Soil Survey (NCSS) Soil Characterization Database as 0.34 cm^3/cm^3 and the wilting point is 0.20 cm^3/cm^3. Soil moisture is collected from a nearby field at ACRE also being managed with a corn-soybean rotation (40° 28' 52.61", -87° 0' 1.12"). The sensors were installed on July 17, 2017 at depths of 10 cm, 20 cm, 40 cm, 60 cm and 80 cm. The soil moisture content (SMC) and soil temperature measurements are obtained from ECH20 5TM sensors and stored on an EM50 data logger (METER Group, Inc., Pullman, Washington). Measurements are recorded at 10-minute intervals where SMC is reported as a fractional volumetric water content (cm^3/cm^3) and soil temperature is reported as units of degrees Celsius (°C). Data are typically downloaded bi-weekly during the growing season.

The effective root zone depth is the depth of soil used by the main body of the plant roots to obtain most of the stored moisture and plant food under proper irrigation. As a rule of thumb, about 70% of the moisture extracted by the root is obtained in the top half of the effective root zone; about 20% from the third quarter; and about 10% from the soil in the deepest quarter of the root zone (Kranz et al., 2008). Because the effective root zone of corn is about 60 cm, in this research, soil moisture data is calculated as the average of the total water content in the soil column of 60 cm.

The SMI is computed based on the soil characteristics and soil moisture conditions and the parameters include field capacity (FC), wilting point (WP), and soil moisture (SM). It offers an independent estimation of water stress based on soil moisture.

Table 4.1. SMI thresholds and their corresponding drought condition (Sridhar et al., 2008). Water deficit, or drought condition intensifies as the SMI decreases from 0, values greater than 0 are not in drought condition.

Drought condition	SMI
Minor	Greater than -1
Moderate	from -1 to -2
High	from -2 to -3
Severe	from -3 to -5
Extreme	-5 or less

Stomatal conductance

Stomatal conductance has been used as benchmark for detecting water deficit stress in many research studies (e.g., Ihuoma and Madramootoo, 2017; Zarco-Tejada et al., 2013; Baluja et al., 2012). In this research, a leaf porometer (SC-1, Decagon devices, Pullman, WA, USA) was used for taking stomatal conductance measurements and each porometer measurement is for only a small part of a single leaf on a plant, so a sampling strategy was implemented to obtain ET estimates relevant for estimating latent heat for the entire canopy. The plot was selected to be the second range inside the field and is to the south of a ground target. Two rows directly in front of the ground target were selected. The length of each row was determined with a tape measure. The length of each row is subdivided into equidistant sections within which measurements were taken. The sampling strategy for measuring stomatal conductance was to use the porometer to measure the two top leaves close to the tassel of a green and healthy plant at each point that will receive the most solar radiation compared with other leaves on the same plant. The leaves were also more visible than other leaves on the same plant since the UAS collected images with the camera oriented straight down. Consistent measurements are taken at the same point in the same rows. Within the predefined plot segment, four measurements were taken. As the growing season

progressed, it was at times necessary to adjust where in the segment measurements were taken because of the presence of damaged, unhealthy, or dying plants. By the end of the growing season, the entire row being sampled might need to be changed due to sample plants not completely yellowed.

4.2.4 Heritability test

Heritability is the measure of how well differences in the plant's genes account for differences in their traits. Heritable traits that can be identified from UAS imagery in addition to or instead of more traditional in-situ sampling are of value because of the relative ease with which such data can be generated. The results of the workflow developed to estimate latent heat and the Bowen ratio of the crops in the field have the potential to provide useful information related to the water use of plant varieties that would be difficult to obtain using other methods. Therefore, the latent heat and Bowen ratio measurements were tested for heritability for a single breeding experiment within Field 54 north (Figure 4.1). That experiment includes 20 varieties of corn with 3 repetitions for each variety that were selected initially for the biomass test.

The heritability, H^2, of a trait is calculated using Equation 4.8 (Tolley et al., 2021):

$$H^2 = \frac{\sigma_G^2}{\sigma_G^2 + \frac{\sigma_\varepsilon^2}{r}} \tag{4.8}$$

In which, σ_G^2 is genotypic variance, σ_ε^2 is the residual variance and r is the repetitions of each genotype in the test. Inputs like latent heat flux and Bowen ratio of each variety will be used to fit linear mixed-effects models and genotypic variance and residual variance can be acquired.

4.3 Results

Thermal and multispectral imagery as well as ground reference data were acquired from nine different dates over two field seasons, 2018 and 2020. The exact day and time for each flight as well as weather parameters are summarized in Table 4.2. Flight operations were conducted between 13:30 and 17:00 EDT, except for the flight on August 13, 2020, which occurred at 19:30

EDT. Afternoon flights were preferred as temperature is more consistent, though the sun angle is not optimal for the multispectral imagery.

Table 4.2. Environmental conditions for all flight dates in 2018 and 2020 used in the analysis. Weather observations were collected at the date and time provided for the flight. Times are local in Eastern Daylight Time (EDT). Weather conditions are for the time of flight, except for the 5-day Rain, which is the cumulative precipitation in the 5-days prior to flight operations. Days After Planting (DAP) is based on the day the field was planted in each year. The Soil Moisture Index (SMI) is based on soil moisture condition at the time of flight.

Flight Time	Air Temperature (^{0}C)	Wind Speed (m/s)	Relative Humidity (%)	Solar Radiation (W/m^2)	5-day Rain (mm)	DAP	SMI
2018/07/12 (16:00)	29.50	2.10	44.70	836.94	10.16	65	-0.90
2018/08/08 (15:30)	28.50	4.70	57.70	699.17	24.13	92	-0.23
2018/08/31 (17:00)	31.10	3.00	56.50	459.58	9.14	115	-0.04
2020/07/02 (17:00)	31.10	3.60	40.90	705.00	2.03	51	-0.64
2020/07/14 (16:30)	29.00	4.00	43.50	743.65	27.69	63	-0.60
2020/07/24 (17:00)	28.90	2.20	49.10	731.64	15.49	73	-0.53
2020/07/28 (17:00)	28.80	3.10	46.20	707.90	34.04	77	-0.34
2020/08/13 (19:30)	26.60	2.70	64.50	109.40	20.32	93	N/A
2020/08/28 (16:30)	30.70	3.10	60.00	568.30	5.84	108	-3.27

4.3.1 Bowen ratio vs. Soil Moisture Index (SMI)

The Bowen ratio is the sensible heat flux over the latent heat flux for a given location. As conditions get drier, it is expected that the latent heat will decrease due to lower water availability and the resulting plant physiological changes. As latent heat decreases, sensible heat will increase to maintain the land surface energy balance, so the Bowen ratio should get larger in response to increasing water deficit. With more water deficit, the SMI becomes increasingly negative, so the two metrics are negatively correlated (Figure 4.3). SMI and Bowen ratio values were compared at the field level because there is only one SMI value per flight date. Field level Bowen ratio is obtained by averaging values from each two-row plot in the experiment.

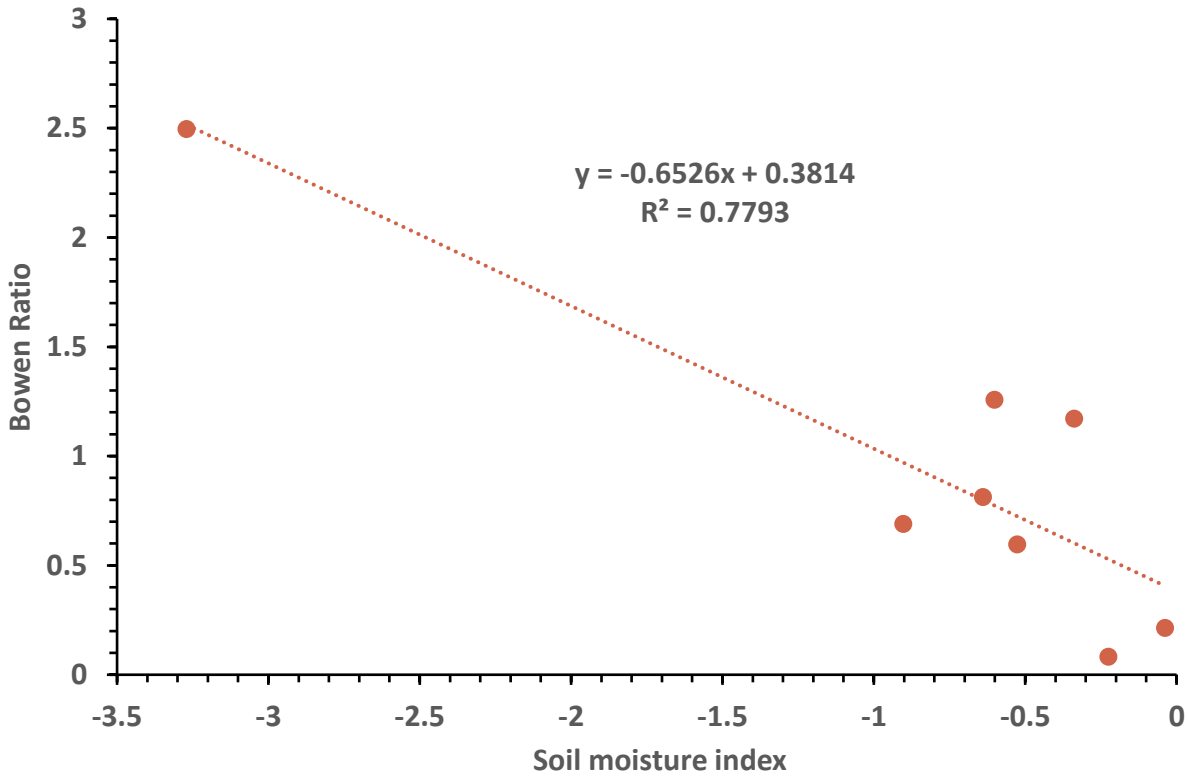

Figure 4.3. Relationship between whole field average Bowen ratio and SMI for all eight observation dates in 2018 and 2020.

SMI of most of the dates is above minus 1 which indicates a non-intense drought. There is one date, August 28, 2020, identified as in severe drought condition based on the SMI. From the Table 4.2, this date has the lowest 5-day precipitation compared with other dates in 2020 except July 2, 2020. The July 2 has the second lowest SMI in 2020.

4.3.2 Bowen ratio vs. Stomatal conductance

Bowen ratio values are also compared with in-situ stomatal conductance measurements (Figure 4.4). Bowen ratio values are different in Figures 4.3 and 4.4 because they are computed for different areas. As the stomatal conductance measurements are collected for only a few locations within the larger field experiment (as described in Section 4.2.4), Bowen ratio for this comparison is computed only for 35 canopy pixels in a small area around each measurement not for the entire field.

Water deficit causes the plant stomata to close to conserve a limited resource, which is measured as low conductance by the porometer. This results in a negative correlation with Bowen ratio with an R^2 = 0.75. The lowest stomatal conductance measurement (96.84 mmol m^{-2} s^{-1}) occurred on August 28, 2020, which is consistent with the date of lowest SMI and highest Bowen ratio.

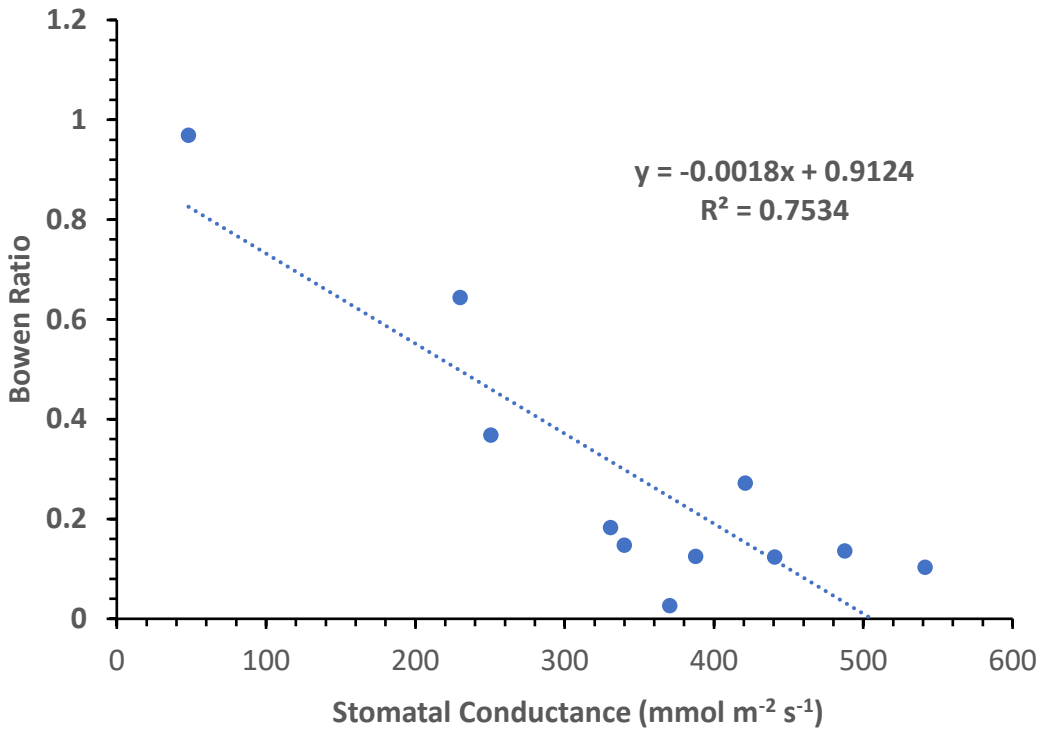

Figure 4.4. Correlation between average Bowen ratio and stomatal conductance for small areas around each stomatal conductance measurement for all observation dates in 2018 and 2020.

4.3.3 Bowen ratio vs. Crop Water Stress Index (CWSI)

The CWSI is a well-established index for water stress and was calculated using Equation 4.1. The index is designed to increase with greater water deficit, so it is positively correlated with the Bowen ratio with a coefficient of determination that is above 0.73. As with the stomatal conductance, the CWSI is computed only for select locations in the field where ground reference data was collected so Bowen ratio values are the same as those in Figure 4.5.

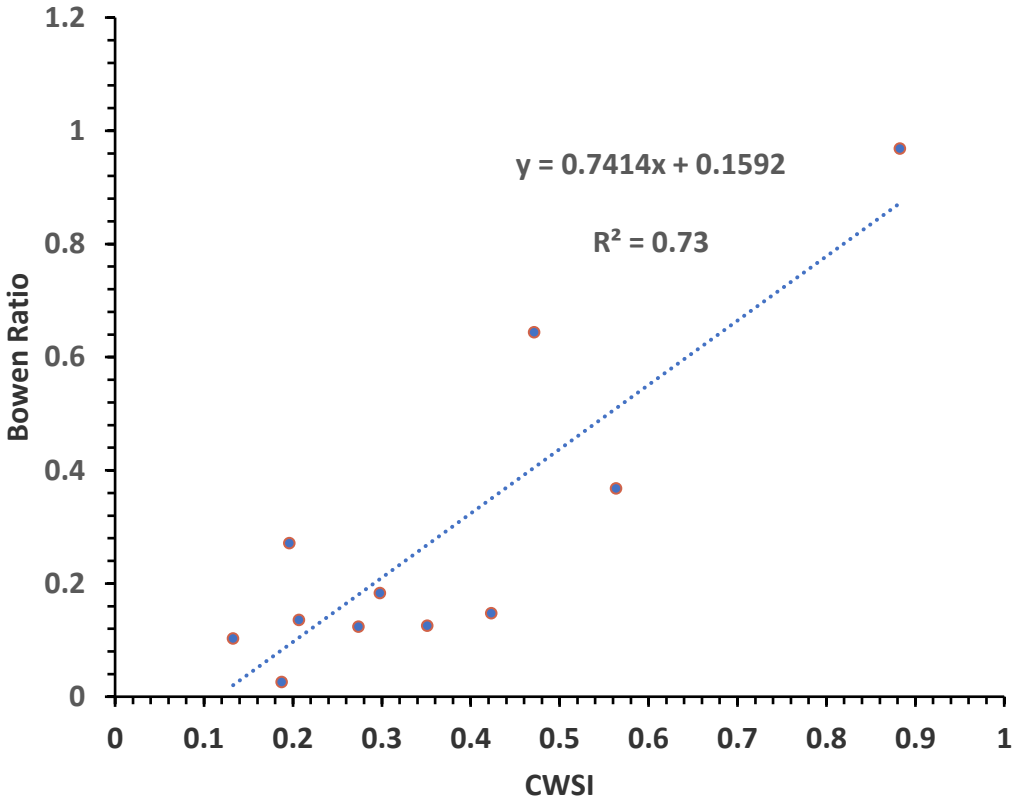

Figure 4.5. The correlation between Bowen ratio and CWSI. Each dot represents the CWSI and Bowen Ratio for a particular handheld stomatal conductance measurement area for all observation dates in 2018 and 2020.

4.3.4 Assessment of multi-spectral crop stress metrics

The three multi-spectral indices include in this study were also assessed against the three water stress indices (SWI, Stomal Conductance and CWSI) to assess how well they correlate with potential water deficit stress. As with the Bowen ratio comparisons in the previous sections, performance between the water stress indices was similar, so only comparisons versus stomatal conductance are presented here for each of the vegetation indices (Figures 4.6, 4.7 and 4.8). All three of the multi-spectral indices are weakly correlated with the stomatal conductance measurements with R-squared values of 0.1735, 0.0133 and 0.2655 for OSAVI, GRVI and REI, respectively. The indices are also all negatively correlated with higher stomatal conduction values associated with lower values of the indices. None of these comparisons support the idea that any of the multi-spectral indices evaluated here are sensitive to the level of water stress identified during flight operations.

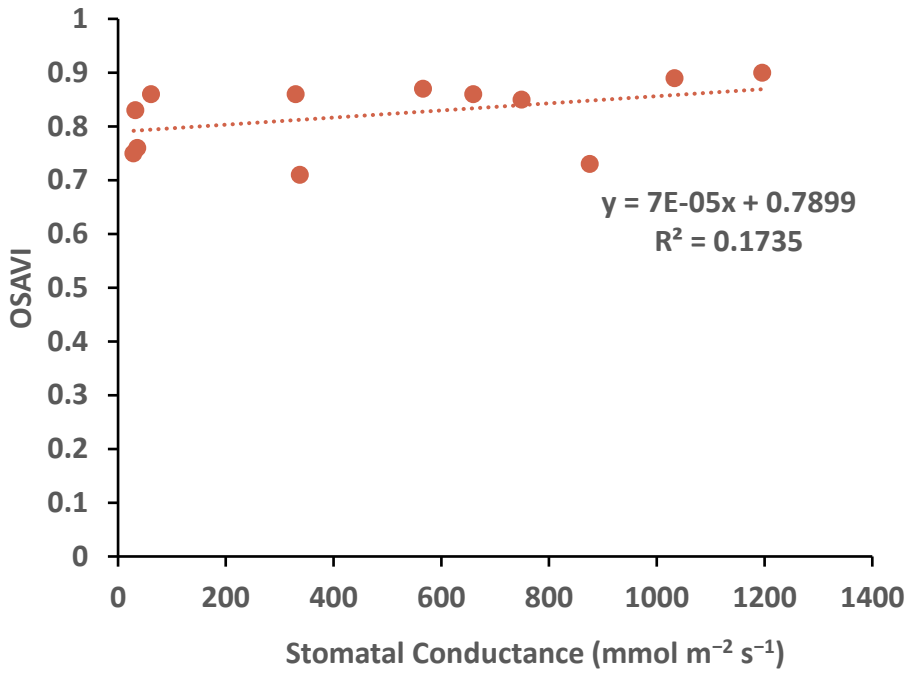

Figure 4.6.. The correlation between stomatal conductance and OSAVI. Each dot represents the stomatal conductance and OSAVI for a stomatal conductance measurement area. Values include comparisons for both 2018 and 2020.

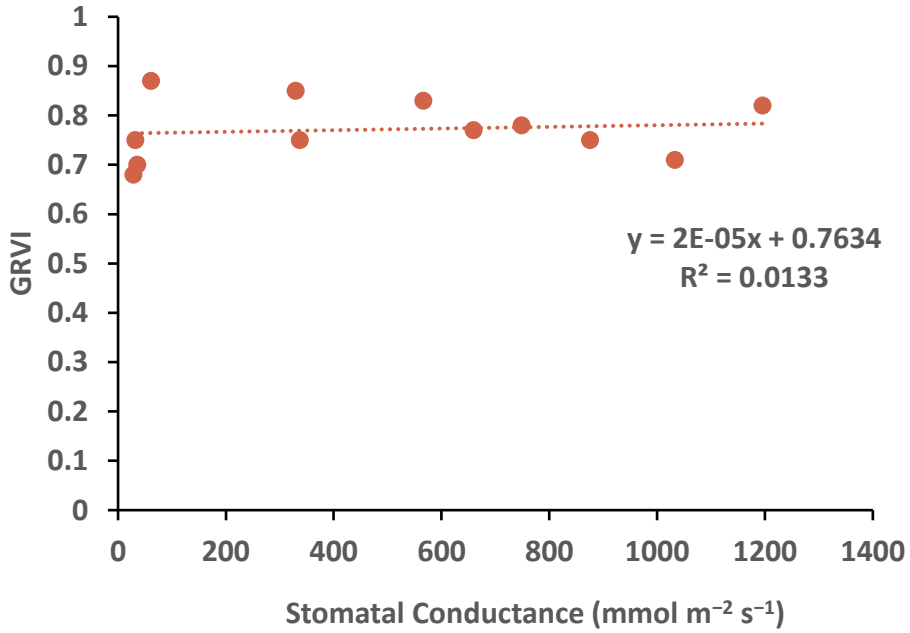

Figure 4.7. The correlation between stomatal conductance and GRVI. Each dot represents the stomatal conductance and GRVI for a stomatal conductance measurement area. Values include comparisons for both 2018 and 2020.

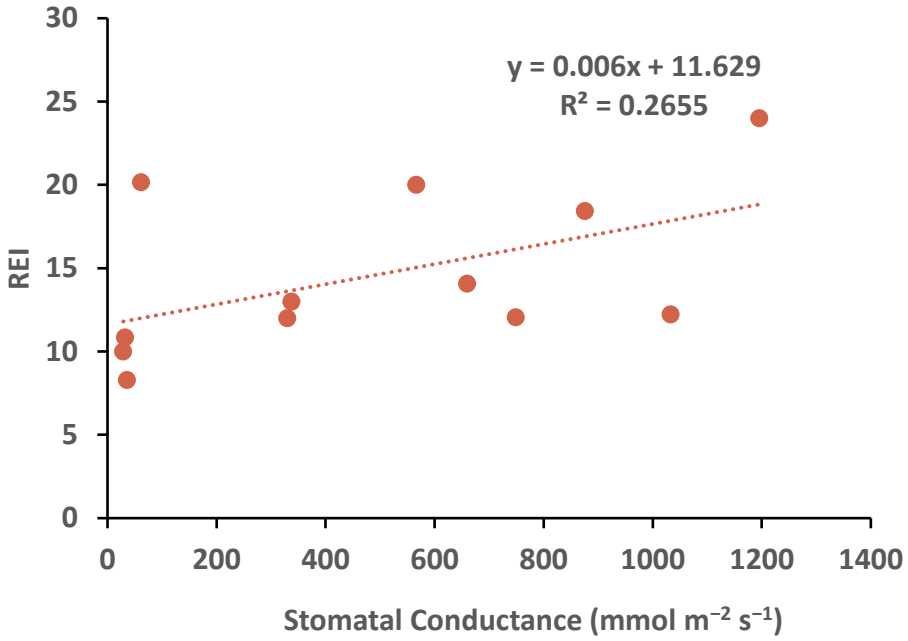

Figure 4.8. The correlation between stomatal conductance and REI. Each dot represents the stomatal conductance and REI for a stomatal conductance measurement area. Values include comparisons for both 2018 and 2020.

4.3.5 Spatial comparisons of water stress indices

A potential advantage of remote sensing-based water stress indices is their ability to quantify differences of water stress across fields and between experiments. To assess this potential, the Bowen ratio as well as the three multi-spectral indices (OSAVI, GRVI and REI) were computed for the entire field. Values are retained only for pixels classified as part of the crop canopy and are then averaged to produce a single value for each of two-row plots in the field. As described in Section 4.2.1., each of these plots is 4.8 meters by 1.6 meters with the longer side oriented north-south.

When assessing across field variability in water stress under the relatively mild stress conditions observed over the 2018 and 2020 field seasons, it is assuming that physical differences in the field environment and genetic differences within the experiment will be the major controls on observed water deficit stress. As topography is likely the largest driver of the spatial variability in water

deficit, a digital surface model (DSM) of the field is provided in Figure 4.9a. The DSM is constructed from high-resolution imagery taken prior to the emergence of crops in the 2020 field season. It highlights that the grassed alleyways around the field are raised with respect to the field itself, that the field slopes downward to the north and west, and that there is a ridge of high elevation at about 30 m east that stretches from the north to the south side of the field. While this field is well drained, water can pool at lower elevations in the spring and after substantial rain fall events. The higher elevation areas are more likely to suffer from water deficit later in the growing season. The rectangle of high elevation in the northwest corner of the figure is a vehicle.

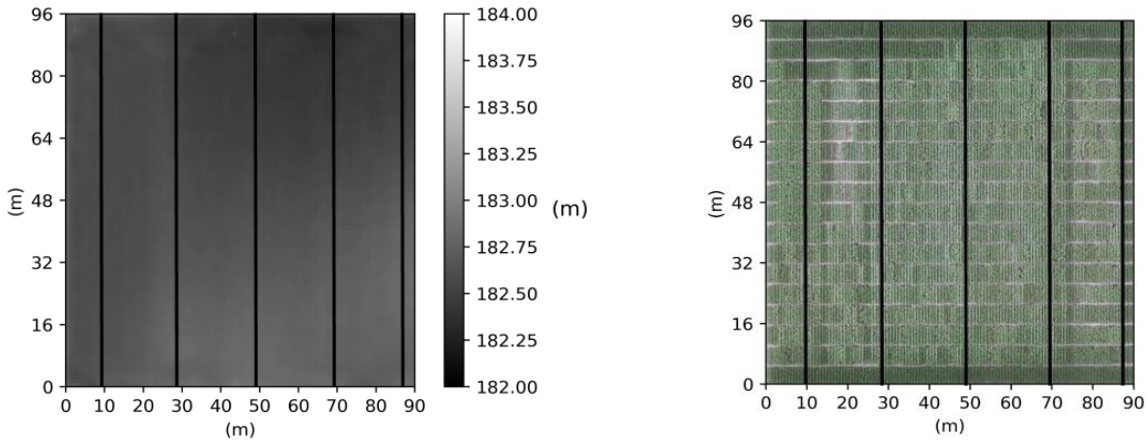

Figure 4.9. The layout of subsurface drainage lines (black) within F54N relative to (a) the digital surface model (DSM) constructed using imagery from May 30,2020 and (b) an RGB mosaic image illustrating the plot layout from the 2020 field season.

As with much of Indiana, the fields at ACRE are subsurface drained to remove excess water from the field in the spring. There are five subsurface drainage lines installed (Figure 4.7) running from north to south. Soil directly above the drainage lines is expected to dry more quickly than the soil farthest from (in the middle of) the drain lines. Note that there is a drainage line at 30 m east, which corresponds to the ridge of highest elevation (Figure 4.7a).

Three dates were selected from the 2020 field season, July 14 (Figure 4.10), July 24 (Figure 4.11) and July 28 (Figure 4.12), to illustrate the spatial variabilities identified using the Bowen ratio and the three multi-spectral indices OSAVI, REI and GRVI on a field level. Flight times are very similar between these dates as are the air temperature, humidity and incoming solar radiation (Table 4.2). More importantly, the SWI decreased from -1.18 on July 14 to -0.88 on July 28 with more than 15 mm of precipitation in the 5-day period before each flight. This means that the field transitioned from moderate water deficit to minor water deficit (Table 4.1) during this period. Unfortunately, due to technical issues multi-spectral images were not collected for the August 28, 2020 ate and thermal imagery is not available for the entire field. The SWI on that date was -3.35 indicating severe water deficit, so Bowen ratio values for the part of the field that was measured are included for comparison with the other dates (Figure 4.13).

Looking at the Bowen ratio maps, it is found that plots with high Bowen ratio values were usually around the field boundary. That is because the boundary plots are in the higher elevation locations and soil water in soil of these locations tend to move to the lower part of the field which makes these parts of the field more subject to water deficit stress. Besides that, the bare soil around the boundary plots also plays a role in increasing the nearby canopy temperature.

The Bowen ratio map of August 28, 2020 (Figure 4.13) is notable as this date has the lowest SWI (-3.27) indicating the highest degree of water deficit stress of any of the flight dates. UAS mapping highlights that it also has the largest area experiencing high Bowen ratios with nearly half of the imaged field experiencing Bowen ratios of greater than 5. The north-south stripes of higher Bowen ratio (around 8 meters and 28 meters east) highlight the effect of the underlying subsurface drainage. The cause of the east-west striping is harder to discern, since it cuts across the experiments and their border rows and does not correspond with any topographic features. It is possible that the high Bowen ratio areas correspond with areas of the field that have senesced or will be senescing soon.

On both July 14 and July 24 of 2020, the GRVI index maps display similar patterns as those are in OSAVI index maps. However, On July 28, the GRVI shows the opposite pattern as what can be seen from OSAVI map. The REI index maps are not correlated with either the OSAVI maps or the GRVI maps.

It is also noticed that the crops around or on top of the tile drainage lines usually have higher OSAVI and GRVI values compared with the crops growing in the middle of the field. This may be explained by when there is excess water in the field, the water will drain faster near the drainage lines which results in a more favorable growing condition for the crops.

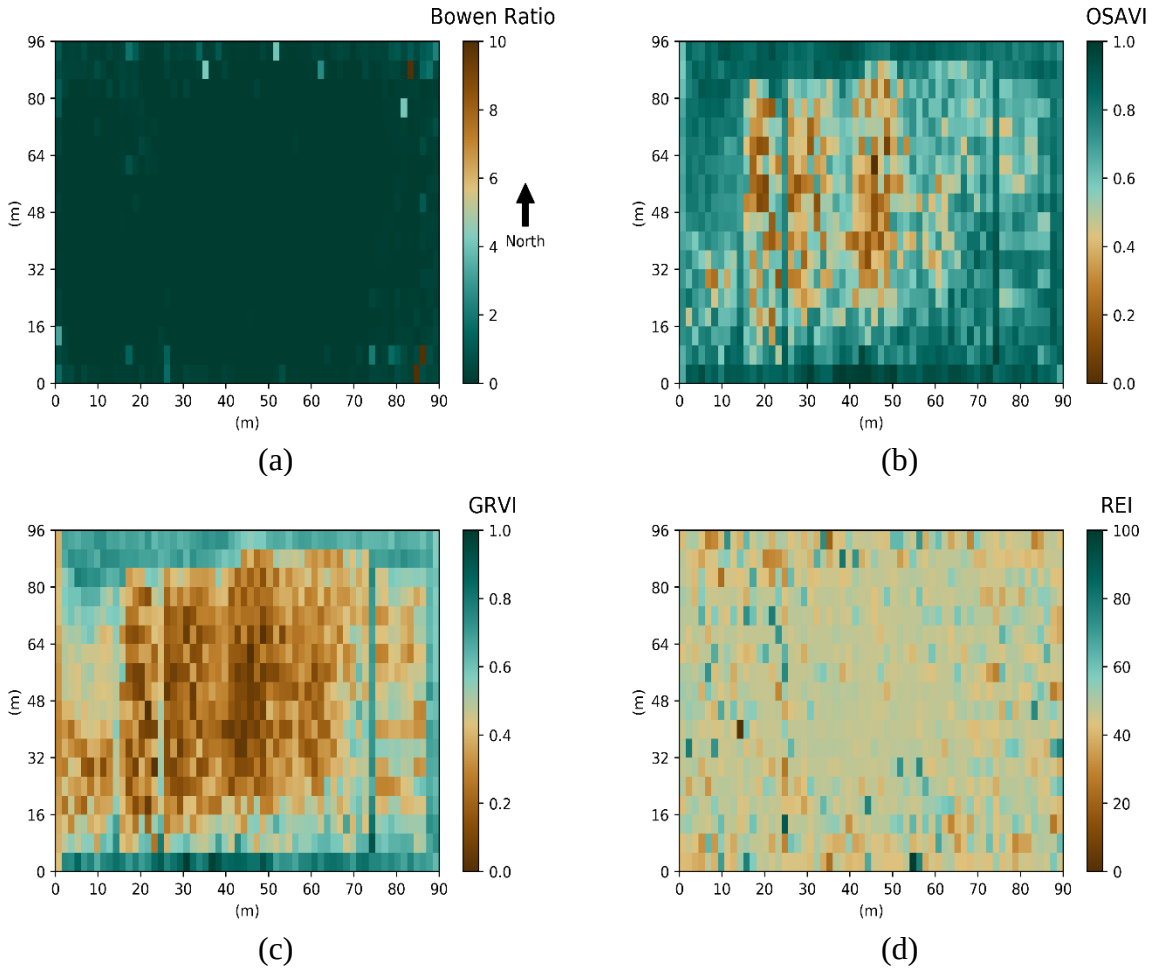

Figure 4.10. Comparison of proposed water stress indices (a) Bowen ratio map;(b) OSAVI map; (c) GRVI map; (d) REI map as computed for each two-row plot in the experiment using imagery from July 14, 2020.

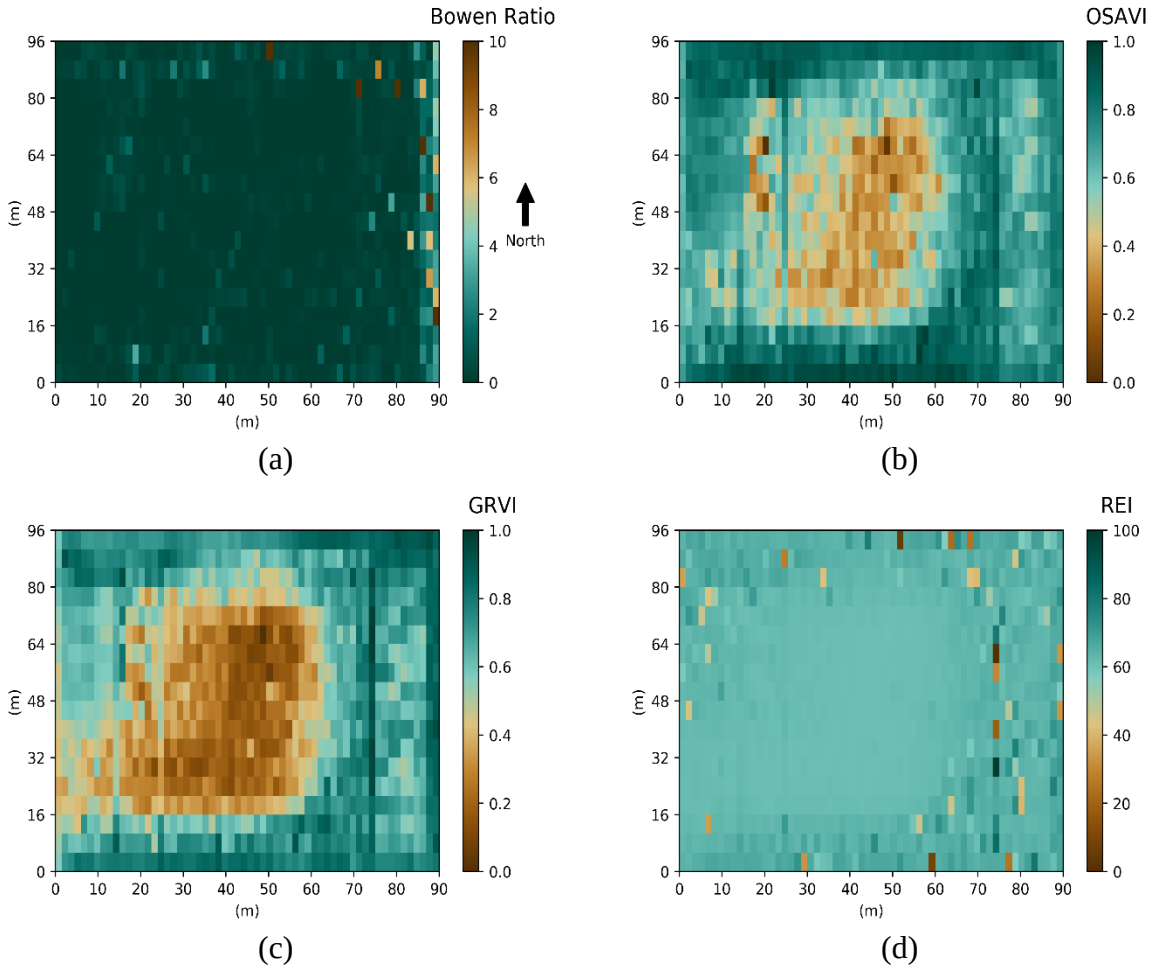

Figure 4.11. Comparison of proposed water stress indices (a) Bowen ratio map;(b) OSAVI map; (c) GRVI map; (d) REI map as computed for each two-row plot in the experiment using imagery from July 24, 2020.

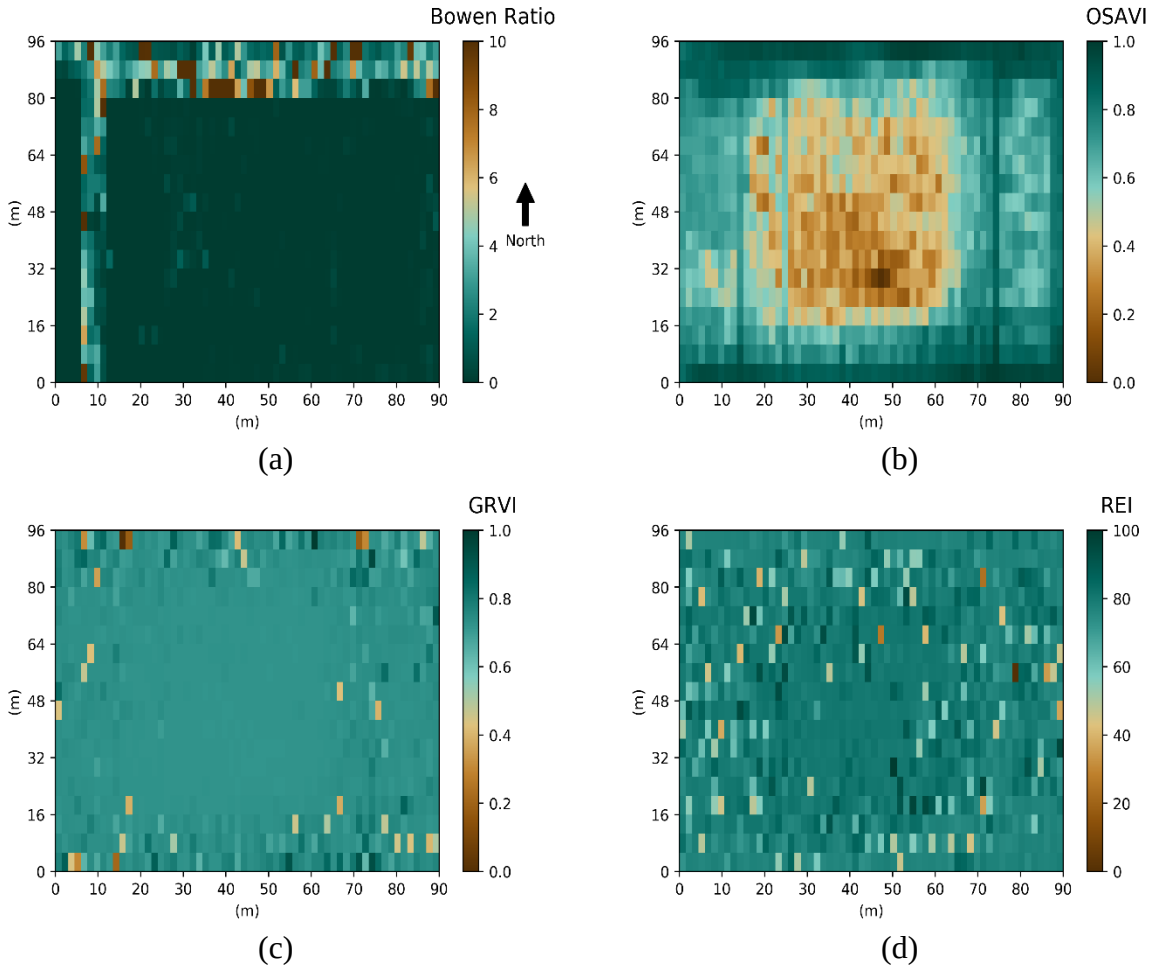

Figure 4.12. Comparison of proposed water stress indices (a) Bowen ratio map;(b) OSAVI map; (c) GRVI map; (d) REI map as computed for each two-row plot in the experiment using imagery from July 28, 2020.

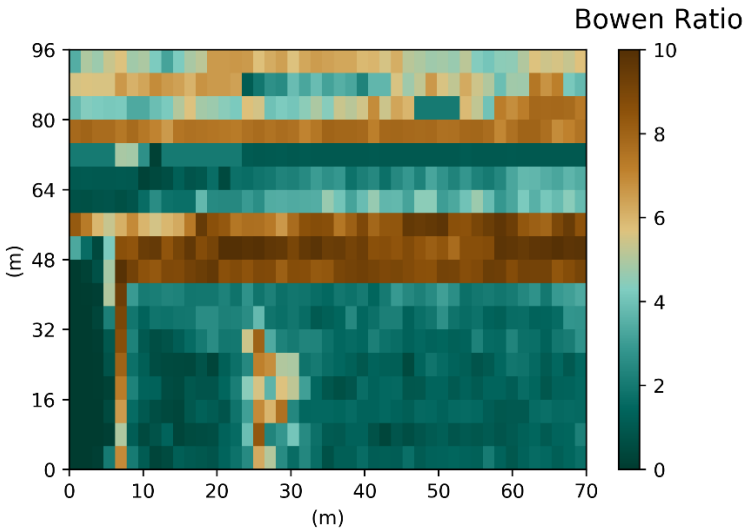

Figure 4.13. Bowen ratio from August 28, 2020. Technical issues resulted in no usable multi-spectral images and only partial flight coverage with the thermal camera. It is shown, however, as it is the day with substantial water stress (Table 4.2).

The correlation between stomatal conductance and the three vegetation indices was found to be very weak (Section 4.3.4), so it was anticipated that the multi-spectral indices are not sensitive to the same stressors as the Bowen ratio. The fact that the spatial patterns of the multi-spectral indices do not correlate with those of the Bowen ratio further illustrates the fact that these indices, if measuring crop stress are mot measuring crop water deficit stress. Other researchers have found that temperature-based indices represent a short-term, instantaneous indicator of water deficit stress, while the spectral vegetation indices are probably the result of cumulative water deficits (Baluja et al., 2012; Ballester et al., 2019). As the crops investigated as part of this study did not experience substantial cumulative water stress during the years of observation, no conclusions can be made as to what the multi-spectral indices were measuring.

4.3.6 Heritability test

Bowen ratio variability across the field was more in line with expectations of water stress causing factors such as proximity to the edge of the field. While environmental variability defined as location within the field explained some variability it was not the only driver. Therefore, the contribution of genetic variability was also evaluated by conducting a heritability test. This analysis focused on a subset of the field, the JCEager experiment located within Field 54 north

(Figure 4.1). Results for July 24, 2020, found the heritability of latent heat flux was 0.597 while that of the Bowen ratio was 0.002. From this analysis, latent heat flux was found to be more heritable than the Bowen ratio as it has a greater heritability value. This suggests that the direct measurement of latent heat flux should be further evaluated as a potentially useful phenotype, while Bowen ratio as calculated in this study is not useful under the environmental conditions assessed as part of this study.

4.4 Discussions

With the increased availability of lightweight, uncooled sensors to measure spectral reflectance and thermal emission, there is an increase in the use of UAS in agriculture. There is still a substantial need for research into practical applications for UAS imagery, and this research evaluates multiple methods to monitor the water status of the crops. Many water deficit stress indicators have been developed to quantify the water stress in the past using either canopy temperature or reflectance information. However, many of these require a significant amount of location and time sensitive data to build location specific water stress indicators reducing their effectiveness in rapid assessment across many fields or crops. Many of these indicators are also confounded by other sources of stress, which limits their applicability as tools for the management of water, such as with irrigation systems. There is a need for a simpler and more robust water stress indicator that can be calculated with readily available UAS imagery and that yields consistent measurements of water stress between fields and crops.

Berni et al. (2009) evaluated the theoretical baselines methods needed for the CWSI calculations and compared the CWSI with water potential and stomatal conductance in olive orchards. They found high correlations between them with a R^2 =0.82 between estimated CWSI and leaf water potential and a R^2 =0.91 between estimated CWSI and canopy conductance. However, they only tested it with a small range of conductance data and lack of data from moderate to minor water stress. In this research, we have independent validation of the Bowen ratio values versus local soil moisture deficit using the soil moisture index (SMI). For the work of Berni et al. (2009), the canopy conductance is not independent from the CWSI which may increase the performance of their model artificially.

Baluja et al. (2012) assessed the water status variability of a rain-fed vineyard by thermal and multispectral imagery using UAS. They found the correlation between CWSI and stomatal conductance to be less than 0.70, which is lower than the correlation found in this research (R^2 = 0.75). The relationship between thermal indices, multispectral indices and vineyard water status confirmed that thermal parameters could be considered as a short-term response while the vegetation indices were probably reflecting the result of cumulative water deficits, hence a long-term response.

Suárez et al. (2008) assess the canopy Photochemical Reflectance Index (PRI) as an indicator of water stress. Relationships were found between PRI and stomatal conductance with determination coefficients yielding from R^2 = 0.02 to R^2 = 0.49 at an individual tree level; while at a block scale (averaging the spectral reflectance from all trees irrigated under the same treatment), R^2 varies from 0.42 to 0.88. They concluded that PRI was able to track diurnal changes in stomatal conductance as function of water stress condition from the airborne imager.

It should be noted that the coefficient of determination derived from the relationship between Bowen ratio and stomatal conductance is relatively high compared with the results of these other research studies. The performance of Bowen ratio methods was also tested against independent measurements of soil moisture that were used to quantify water stress condition using the SMI, and again yielded a high coefficient of determination. Both tests indicate that the Bowen ratio method is highly sensitive to water stress in the observed crop. The relationship between Bowen ratio values and other spectral based vegetation indices values was not strong, which suggests that the spectral vegetation indices were not sensitive to the same changes in water stress observed with the Bowen ratio. This suggests that the Bowen ratio and vegetative stress indices were sensitive to different crop stress. This could be in part because the spectral indices are sensitive to physiological changes in the crop from any stress, but could also be related to the findings of Baluja et al. (2012) who proposed that temperature represents a short-term, instantaneous indicator of water deficit stress, while the spectral vegetation indices are more likely the result of cumulative water deficits. This suggests that there will be a lag between the stress indicators so that the spectral indices may not capture the effect of late season water deficit and may continue to be influenced by the effects of early season stresses after the temperature methods indicate that stress levels have

reduced. This suggests that a combination of both spectral and thermal methods might be most helpful in monitoring both short term and long-term water stress effects.

The results presented here prove that the Bowen ratio can be used as a water deficit stress indicator which demonstrated high correlation with other well-known water deficit stress indicators. The workflow developed here can be used to monitor instantaneous water deficit stress status of row crops by using high resolution thermal and RGB imagery from UAS. Challenges remain for further testing the index under a variety of conditions for example, in severe drought conditions.

4.5 Conclusions

A new indicator (Bowen ratio) of water deficit stress was proposed along with a workflow to derive this index for row crops using high resolution thermal and RGB imagery from UAS. The Bowen ratio has a high correlation with three well-developed water stress indicators: CWSI, stomatal conductance and SWI (R^2 = 0.73, 0.75 and 0.78 respectively). Among these indicators, SWI is an independent evaluation of crop water stress since it is based on observations of soil moisture and does not make use of any of the remote sensing or weather data required for the other indices. The results presented here prove that Bowen ratio is an effective indicator of instantaneous water deficit stress. The workflow developed here can be applied to monitor the instantaneous water stress conditions for all types of row crops using inexpensive cameras and calibration methods.

The relationship between Bowen ratio and several spectral indices (OSAVI, GRVI, REI) has also been investigated. Compared with direct measures of water stress (CWSI, stomatal conductance, SWI), correlation with these vegetation indices is much lower (R^2< 0.4). Correlation is also low between the vegetation indices and the direct measure of water stress, which suggests that the vegetation indices are less sensitive to the instantaneous water stress condition of the crop. Other researchers have postulated that the vegetative indices are more sensitive to long-term water deficit stress than the short-term water stress observed here as neither of the field seasons evaluated were especially affected by drought stress.

Both the in-field variability in elevation and the location of subsurface drainage lines were assessed as possible causes for observed spatial variability in water stress measurements. Spatial variability

in the Bowen ratio maps was correlated with the location of subsurface drainage and edge of field effects, while the vegetation indices were most affected by proximity to the edge of the field.

The heritability of latent heat flux is 0.597 which is higher than that of Bowen ratio. This indicates the variance of latent heat flux can be explained by the variance of genotypes in the field and latent heat flux can be a good phenotypic trait for breeders to focus on when selection of a drought tolerant genotype is needed.

Since all the data were collected in rain-fed corn field, and there were no substantial drought conditions observed during the data collection dates, future work will need to evaluate the performance of the Bowen ratio method and workflow for additional crops and under more extreme water stress conditions.

5. CONCLUSIONS AND FUTURE WORK

5.1 Summary

The overall goal of this work is to build a tool which takes vegetative surface temperature and other auxiliary data as inputs to estimate instantaneous water status of crops. Such a tool can be used by farmers or administrators for better management of water resources and to select more drought tolerant genotypes as part of breeding programs. To address this goal, the following objectives are established for this research project: (1) Improving the measurement accuracy of inexpensive uncooled thermal camera mounted on the UAS by conducting indoor and atmospheric correction of thermal camera calibration using water targets and compare calibrated and uncalibrated temperature measurements to quantify how the calibration improves the temperature measurements accuracy of the camera, (2) Customize the TSEB model to adapt it for high resolution thermal imagery from UAS for estimating latent heat flux from field plots and evaluate accuracy against ground reference datasets. (3) Calculate OSAVI, REI, GRVI, CWSI and Bowen Ratio by using spectral information and infrared thermometry information and test how these indices change with stomatal conductance and each other.

To increase the accuracy of the thermal camera, a method was introduced in Chapter 2 to improve the accuracy of temperature observations from a UAS-based uncooled thermal infrared camera using a combination of laboratory calibration and in-field water targets for atmospheric correction. The pixel-based thermal calibration method presented here was able to reduce the measurement uncertainty across all the pixels in the images, thus improving the accuracy and reducing the between-pixel variability of the measurements. After calibration, the camera was more accurate over the range of normal temperatures within its field of view during the growing season. The results suggest that a non-linear calibration function might be more appropriate if a wider calibration range is required. During field calibration, the RMSE values relative to ground reference targets for two flights in 2017 were reduced from 6.36°C to 1.24°C and from 4.56°C to 1.32°C, respectively. The results also indicate that building a single atmospheric correction relationship using the seed image and the ground-based water targets was sufficient to reduce measurement uncertainty in all cases for the duration of the flight.

The developed calibration methods are then applied to the thermal camera. In Chapter 3, Very high- resolution thermal datasets (0.05 m) and corresponding RGB datasets (0.03 m) were used for calculating crop latent hear flux using an adapted two source energy balance (TSEB) model. The RGB datasets were used for supervised classification of soil and vegetation, the classification results were then used to filter the thermal mosaics to separate vegetation and soil temperatures, then the vegetation temperature is used for calculating latent heat flux and finally the results are validated by ground porometry measurements as well as latent heat flux calculated from the Penman-Monteith (PM) equation using local weather data. The estimation results are not only consistent with the ground reference measurements by porometer but also consistent with the weather conditions on the date of observation. When comparing with the ground reference data, the RMSE for the validation data of 9 dates in 2018 and 2020 is 65.23 W/m^2 and the coefficient of determination (R^2) is above 0.9. The results indicate that the workflow developed here is suitable for using high resolution thermal imagery to calculate latent heat flux of corn accurately.

As latent heat flux is a direct measure of plant water use it can be used to monitor the water deficit stress level of crops in the field. In Chapter 4, an index: Bowen ratio is used for water deficit stress quantification. Very high-resolution thermal datasets (0.05 m) and corresponding RGB datasets (0.03 m) as well as multi-spectral datasets (0.04 m) were used as inputs for the calculation of multiple water stress indices found in literature. Then the latent and sensible heat from Chapter 4 is used for calculating the Bowen ratio (the ratio of sensible to latent heat). Finally, the various water stress indices are evaluated against three accepted measures of crop water stress potential: the soil moisture index (SMI), the crop water stress index (CWSI), and in-situ measurements of stomatal conductance. Nine dates over two field seasons (2018 and 2020) were evaluated and the coefficient of determination (R^2) of Bowen ratio versus the water stress indices SWI, CWSI and stomatal conductance are all above 0.73. These results indicate that the Bowen ratio can be used as an alternative for the well-known CWSI and even more advantageous because of its simplicity. The spectral vegetation indices were found to be less correlated with the water stress indices (Bowen Ration and CWSI), and were not well correlated spatially with the Bowen ratio method. As the spectral indices are more of a direct measurement of the physiological changes in the crop in response to stress, it is not unexpected that they are not as collated with the water stress indices. There is evidence in the literature that temperature-based indices such as the Bowen ratio are more

sensitive to short-term water deficit stress while the spectral indices are more sensitive to the cumulative effect of longer-term water stress. All observations used for this analysis were in rain-fed corn without substantial long-term water deficit, the validity of this relationship could not be tested.

5.2 Conclusions

Four hypotheses were proposed in Chapter 1 as a focus of this research, so each is reviewed here to assess how the research was or was not able to address each:

> **Hypothesis 1:** Calibration and atmospheric correction of uncooled thermal infrared cameras will increase the accuracy and decrease the variability in measurements of canopy temperature from UAS platforms as compared to uncalibrated and uncorrected imagery.

Confirmed. The pixel-based thermal calibration method presented here was able to reduce the measurement uncertainty across all the pixels in the images, thus improving the accuracy and reducing the between-pixel variability of the measurements. After calibration, the camera was more accurate over the range of normal temperatures within its field of view during the growing season. During field calibration, the RMSE values relative to ground reference targets for two flights in 2017 were reduced from 6.36°C to 1.24°C and from 4.56°C to 1.32°C, respectively. The above hypothesis was tested at a research farm in west-central Indiana. Further data analysis from flights in 2020 indicated that when using water targets with three temperatures, a minimum temperature less than 10°C, and a maximum temperature above 35°C, the RMSE of the calibrated temperature will always be less than 1.00°C. If the temperature range requirement is eased to 20°C, then there is only a 64% chance that the RMSE will be less than 1.49°C.

Calibration and atmospheric correction increased the range of measured temperatures in the images and increased the image contrast, which may help with identification of tie-points and stitching of images together to form whole-field mosaics. Image calibration and atmospheric correction are important for achieving the best accuracy in measured temperatures, which will become even more important as vegetative surface temperature is used to estimate latent heat flux and is included in multi-sensor fusion to better predict crop biomass and yield

Hypothesis 2: High resolution thermal infrared and RGB imagery from a thermal camera system mounted on a UAS can distinguish between soil and plants, thus increasing the accuracy of estimated ET from agricultural crops as compared to coarser resolution satellite imagery.

Confirmed. When comparing with the ground reference data, the RMSE for the validation data of nine observation dates over two field seasons (2018 and 2020) is 65.23W/m^2 and the coefficient of determination (R^2) is above 0.9. The results indicate that the workflow developed here is suitable for using high resolution thermal imagery to calculate latent heat flux of corn accurately. The above hypothesis was tested at the same location as for the hypothesis 1. Best estimation results were achieved in cloudless weather conditions when solar radiation did not change abruptly. When there were intense clouds in the sky, solar radiation could change dramatically which bring in huge errors to the estimation results. It is also observed that when the solar radiation is higher, there is a stronger linear relationship between estimated latent heat flux and reference latent heat flux, which indicated the performance of the model is more robust under high incoming solar radiation conditions.

It should be noted that the root mean square error is large when the reference LE is low (under deficit water stress or low incoming solar radiation) or high (with abundant water or having high incoming solar radiation). In the end, through the calibrations, we are still able to achieve reasonable results.

Hypothesis 3: Bowen ratio can be an alternative crop water stress indicator to other spectral or temperature-derived indicators.

Confirmed. The coefficient of determination (R^2) of Bowen ratio and SWI, CWSI and stomatal conductance are all above 0.73. The hypothesis was tested at one research field in west-central Indiana for two years. The Bowen ratio has a relative high correlation with three well-developed water stress indicators: CWSI, stomatal conductance and SWI (R^2 = 0.73, 0.75 and 0.78, respectively). Among these indicators, SWI is an independent test since it only uses the soil moisture and texture information and none of the weather data or remote sensing imagery used for the other indices. The results presented here prove that Bowen ratio is an effective indicator of

water deficit stress. The workflow developed here can be applied to monitor the instantaneous water stress conditions for row crops in the fields.

Hypothesis 4: Various vegetation and thermal indices acquired on plot level can be beneficial for genotypic selection in breeding.

Confirmed. The workflow and algorithms developed in this research help to calculate the heritability of latent heat flux and Bowen ratio of each genotype of crops in the field. The heritability of latent heat flux is 0.597 while that of Bowen ratio is 0.002. The hypothesis was tested at one research field in west-central Indiana for two years. The developed work flow demonstrates the ability to generate field thermal and multispectral mosaics and extract plots with different genotypes of the same crop planted in them. Heritability of latent heat flux and Bowen ratio can be calculated for each individual row and plot thus these indices of different genotypes can be compared with each other, and desirable genotype can be selected. Results for the one experiment analyzed suggests that the direct measurement of latent heat flux is more likely to be a useful phenotype for genetic selection than Bowen ratio. Additional work must be conducted to determine if this assessment holds up, and whether or not Bowen ratio would be a more heritable phenotype under conditions with more severe water deficit.

5.3 Future work

In this this study, a workflow was developed to take advantage of thermal remote sensing imagery collected from a UAS to quantify crop water status. In order to achieve this goal, the thermal camera first need to be calibrated. Although water targets have been built for this purpose, there is still a need to improve the design of the water targets to incorporate lessons learned after multiple seasons of use. Specifically, a new design focused on making the targets more mobile with a larger water surface area to increase their visibility would be beneficial. The calibration process should also be tested under a wider range of weather and surface conditions.

The workflow developed to quantify the latent heat flux and water deficit stress was tested only for corn and will need to be tested on more types of crops. Additionally, work should continue to assess differences in the latent heat flux between different parts of the crop canopy, such as

between sunlit leaves and shaded leaves of the same plant, but also between different plants in the same plot. A better understanding of the actual variability in latent heat (or stomatal conductance) can be used to improve latent heat estimated in the future. Additionally, the water stress experiments did not incorporate years with substantial water stress which may affect the relationship between the various indices tested. The workflow also needs to be evaluated for other types of crops. Future work should also consider the potential for a index the combines spectral and thermal information to quantity the combined effect of long and short-term water deficits.

REFERENCES

Aladenola, O.O. & Madramootoo, C.A. (2014). Evaluation of solar radiation estimation methods for reference evapotranspiration estimation in Canada. Theoretical and Applied Climatology, 118, 377–385. https://doi.org/10.1007/s00704-013-1070-2

Alchanatis, V., Cohen, Y., Cohen, S., Moller, M., Sprinstin, M., Meron, M., J. Tsipris, Y. Saranga & Sela, E. (2010). Evaluation of different approaches for estimating and mapping crop water status in cotton with thermal imaging. Precision Agriculture, 11(1), 27-41. https://doi.org/10.1007/s11119-009-9111-7

Allen, R. G., Pereira, L. S., Raes, D., & Smith, M. (1998) Crop evapotranspiration-Guidelines for computing crop water requirements-FAO Irrigation and drainage paper 56. FAO, Rome, 300, D05109.

Anderson, M. C., Allen, R. G., Morse, A., & Kustas, W. P. (2012) Use of Landsat thermal imagery in monitoring evapotranspiration and managing water resources. Remote Sensing of Environment, 122, 50-65. https://doi.org/10.1016/j.rse.2011.08.025

Ballester, C., Brinkhoff, J., Quayle, W. C., & Hornbuckle, J. (2019). Monitoring the effects of water stress in cotton using the green red vegetation index and red edge ratio. Remote Sensing, 11(7), 873. https://doi.org/10.3390/rs11070873

Baluja, J., Diago, M. P., Balda, P., Zorer, R., Meggio, F., Morales, F. & Tardaguila, J. (2012) Assessment of vineyard water status variability by thermal and multispectral imagery using an unmanned aerial vehicle (UAV). Irrigation Science, 30, 511-522. https://doi.org/10.1007/s00271-012-0382-9

Barbagallo, S., Consoli, S., & Russo, A. (2009). A one-layer satellite surface energy balance for estimating evapotranspiration rates and crop water stress indexes. Sensors, 9, 1–21. http://doi.org/10.3390/s90100001

Baret, F., & Guyot, G. (1991). Potentials and limits of vegetation indices for LAI and APAR assessment. Remote sensing of environment, 35(2-3), 161-173. https://doi.org/10.1016/0034-4257(91)90009-U

Barsi, J. A., Barker, J. L., & Schott, J. R. (2003). An atmospheric correction parameter calculator for a single thermal band earth-sensing instrument. IEEE International Geoscience and

Remote Sensing Symposium Proceedings (IEEE Cat. No.03CH37477). Piscataway, NJ: IEEE. http://doi.org/10.1109/IGARSS.2003.1294665

Behmann, J., Steinrücken, J., & Plümer, L. (2014). Detection of early plant stress responses in hyperspectral images. ISPRS Journal of Photogrammetry and Remote Sensing, 93, 98-111. https://doi.org/10.1016/j.isprsjprs.2014.03.016

Bellvert, J., Marsal, J., Girona, J., Gonzalez-Dugo, V., Fereres, E., Ustin, S. L., & Zarco-Tejada, P. J. (2016). Airborne thermal imagery to detect the seasonal evolution of crop water status in peach, nectarine and Saturn peach orchards. Remote Sensing, 8(1), 39. https://doi.org/10.3390/rs8010039

Berni, J. A. J., Zarco-Tejada, P. J., Sepulcre-Canto, G., Fereres, E. & Villalobos, F. (2009a). Mapping canopy conductance and CWSI in olive orchards using high resolution thermal remote sensing imagery. Remote Sensing of Environment, 113, 2380-2388. http://doi.org/10.1016/j.rse.2009.06.018

Berni, J. A. J., Zarco-Tejada, P. J., Suarez, L., & Fereres, E. (2009b). Thermal and narrowband multispectral remote sensing for vegetation monitoring from an unmanned aerial vehicle. IEEE Transactions on Geoscience and Remote Sensing, 47, 722-738. http://doi.org/10.1109/TGRS.2008.2010457

Bowen, I. S. (1926) The ratio of heat losses by conduction and by evaporation from any water surface. Physical review, 27, 779. http://dx.doi.org/10.1103/PhysRev.27.779

Bower, S., J. Kou & Saylor J. (2009) A method for the temperature calibration of an infrared camera using water as a radiative source. Review of Scientific Instruments, 80, 095107. https://doi.org/10.1063/1.3213075

Brenner, A. J., & Incoll, L. D. (1997). The effect of clumping and stomatal response on evaporation from sparsely vegetated shrublands. Agricultural and Forest Meteorology, 84(3-4), 187-205. https://doi.org/10.1016/S0168-1923(96)02368-4

Brutsaert, W. (2005). Hydrology: an introduction. Cambridge University Press.

Budzier, H., & Gerlach, G. (2015). Calibration of uncooled thermal infrared cameras. Journal of Sensors and Sensor Systems, 4, 187-197. http://doi.org/10.5194/jsss-4-187-2015

Campbell, G. S., & Norman, J. M. (2012). An introduction to environmental biophysics (2nd ed., pp.163). New York, USA: Springer Science & Business Media.

Cherkauer, K. A., Burges, S. J., Handcock, R. N., Kay, J. E., Kampf, S. K., & Gillespie, A. R. (2005). Assessing satellite-based and aircraft-based thermal infrared remote sensing for monitoring pacific northwest river temperature. Journal of the American Water Resources Association, 41, 1149-1159. http://doi.org/10.1111/j.1752-1688.2005.tb03790.x.

Colaizzi, P. D., Kustas, W. P., Anderson, M. C., Agam, N., Tolk, J. A., Evett, S. R., ... & O'Shaughnessy, S. A. (2012). Two-source energy balance model estimates of evapotranspiration using component and composite surface temperatures. Advances in water resources, 50, 134-151. https://doi.org/10.1016/j.advwatres.2012.06.004

Deery, D. M., Rebetzke, G. J., Jimenez-Berni, J. A., James, R. A., Condon, A. G., Bovill, W. D., Hutchinson, P., Scarrow, J., Davy, R., & Furbank, R. T. (2016). Methodology for High-Throughput Field Phenotyping of Canopy Temperature Using Airborne Thermography. Frontiers in Plant Science, 7, 1808. https://doi.org/10.3389/fpls.2016.01808

Devices, D. (2006) Leaf porometer. Operator's manual. Version 1.0. Decagon Devices. Inc., Pullman, WA.

De Maesschalck, R., Jouan-Rimbaud, D., & Massart, D. L. (2000). The mahalanobis distance. Chemometrics and intelligent laboratory systems, 50(1), 1-18. https://doi.org/10.1016/S0169-7439(99)00047-7

Doebelin, E. O., & Manik, D. N. (1996). Measurement systems: application and design (4th ed., pp. 44-56). New York, USA: McGraw-Hill.

Eitel, J. U., Keefe, R. F., Long, D., Davis, A., & Vierling, L. A. (2010). Active ground optical remote sensing for improved monitoring of seedling stress in nurseries. Sensors, 10, 2843-2850. http://doi.org/10.3390/s100402843

Espinoza, C. Z., Khot, L. R., Sankaran, S., & Jacoby, P. W. (2017). High resolution multispectral and thermal remote sensing-based water stress assessment in subsurface irrigated grapevines. Remote Sensing, 9(9), 961. https://doi.org/10.3390/rs9090961

FLIR. (2018a). How is NEDT measured? Retrieved from http://flir.custhelp.com/app/answers/detail/a_id/128/~/how-is-nedt-measured?

FLIR. (2018b). Infrared Camera Accuracy and Uncertainty in Plain Language. Retrieved from https://www.flir.com/discover/rd-science/infrared-camera-accuracy-and-uncertainty-in-plain-language/

Garces-Restrepo, C., Vermillion, D., & Muoz, G. (2007). Irrigation management transfer. Worldwide efforts and results.

Gerosa, G., S. Mereu, A. Finco & Marzuoli, R. (2012). Stomatal conductance modeling to estimate the evapotranspiration of natural and agricultural ecosystems. Evapotranspiration-Remote Sensing and Modeling. http://doi.org/10.5772/21825

Gowda, P. H., Chavez, J. L., Colaizzi, P. D., Evett, S. R., Howell, T. A., & Tolk. J. A. (2008). ET mapping for agricultural water management: present status and challenges. Irrigation Science, 26, 223–237. http://doi.org/10.1007/s00271-007-0088-6

Handcock, R., Gillespie, A., Cherkauer, K. A., Kay, J., Burges, S., & Kampf, S. (2006). Accuracy and uncertainty of thermal-infrared remote sensing of stream temperatures at multiple spatial scales. Remote Sensing of Environment, 100, 427-440. http://doi.org/10.1016/j.rse.2005.07.007

Heilman, J. L., Brittin, C. L., & Neale, C. M. U. (1989). Fetch requirements for Bowen ratio measurements of latent and sensible heat fluxes. Agricultural and Forest Meteorology, 44(3-4), 261-273. https://doi.org/10.1016/0168-1923(89)90021-X

Heitman, J. L., Horton, R., Sauer, T. J., Ren, T. S., & Xiao, X. (2010). Latent heat in soil heat flux measurements. Agricultural and Forest Meteorology, 150(7-8), 1147-1153. https://doi.org/10.1016/j.agrformet.2010.04.017

Hoffmann, H., Nieto, H., Jensen, R., Guzinski, R., Zarco-Tejada, P., & Friborg, T. (2016). Estimating evaporation with thermal UAV data and two-source energy balance models. Hydrology and Earth System Sciences, 20, 697-713. http://doi.org/10.5194/hess-20-697-2016

Howell, T. A., McCormick, R. L., & Phene, C. J. (1985). Design and installation of large weighing lysimeters. Transactions of the ASABE, 28(1), 0106-0112. http://doi.org/10.13031/2013.32212

Jones, H. G. (1999) Use of infrared thermometry for estimation of stomatal conductance as a possible aid to irrigation scheduling. Agricultural and Forest Meteorology, 95, 139-149. https://doi.org/10.1016/S0168-1923(99)00030-1

Idso, S. B., Jackson, R. D., Pinter Jr, P. J., Reginato, R. J., & Hatfield, J. L. (1981). Normalizing the stress-degree-day parameter for environmental variability. Agricultural meteorology, 24, 45-55. https://doi.org/10.1016/0002-1571(81)90032-7

Ihuoma, S. O., & Madramootoo, C. A. (2017). Recent advances in crop water stress detection. Computers and Electronics in Agriculture, 141, 267-275. https://doi.org/10.1016/j.compag.2017.07.026

Ihuoma, S. O., & Madramootoo, C. A. (2019). Sensitivity of spectral vegetation indices for monitoring water stress in tomato plants. Computers and Electronics in Agriculture, 163, 104860. https://doi.org/10.1016/j.compag.2019.104860

Ishimwe, R., Abutaleb, K., & Ahmed, F. (2014). Applications of thermal imaging in agriculture—a review. Advances in Remote Sensing, 3 (03), 128. http://doi.org/10.4236/ars.2014.33011

Jackson, R. D., S. Idso, R. Reginato & P. Pinter (1981) Canopy temperature as a crop water stress indicator. Water Resources Research, 17(4), 1133-1138. https://doi.org/10.1029/WR017i004p01133

Jackson, R. D., Kustas, W. P., & Choudhury, B. J. (1988). A reexamination of the crop water stress index. Irrigation Science, 9(4), 309-317. https://doi.org/10.1007/BF00296705

Jensen, A. M., McKee, M., & Chen, Y. (2014). Procedures for processing thermal images using low-cost microbolometer cameras for small unmanned aerial systems. IEEE Geoscience and Remote Sensing Symposium, pp. 2629-2632. Piscataway, NJ: IEEE. http://doi.org/10.1109/IGARSS.2014.6947013

Jensen, M. E. & Allen, R. G. (2016). Evaporation, evapotranspiration, and irrigation water requirements. American Society of Civil Engineers. https://doi.org/10.1061/9780784414057

Jones, H. G. (1999). Use of infrared thermometry for estimation of stomatal conductance as a possible aid to irrigation scheduling. Agricultural and Forest Meteorology, 95(3), 139-149. https://doi.org/10.1016/S0168-1923(99)00030-1

Katsoulas, N., Elvanidi, A., Ferentinos, K. P., Kacira, M., Bartzanas, T., & Kittas, C. (2016). Crop reflectance monitoring as a tool for water stress detection in greenhouses: A review. biosystems engineering, 151, 374-398. https://doi.org/10.1016/j.biosystemseng.2016.10.003

Kay, J. E., Kampf, S. K., Handcock, R. N., Cherkauer, K. A., Gillespie, A. R., & Burges, S. J. (2005). Accuracy of lake and stream temperatures estimated from thermal infrared images. Journal of the American Water Resources Association, 41, 1161-1175. http://doi.org/10.1111/j.1752-1688.2005.tb03791.x.

Khanal, S., Fulton, J., & Shearer, S. (2017). An overview of current and potential applications of thermal remote sensing in precision agriculture. Computers and Electronics in Agriculture, 139, 22-32. http://doi.org/10.1016/j.compag.2017.05.001

Kozak, J. A., Aiken, R. M., Flerchinger, G. N., Nielsen, D. C., Ma, L., & Ahuja, L. (2007). Comparison of modeling approaches to quantify residue architecture effects on soil temperature and water. Soil Tillage Research, 95, 84–96. http://doi.org/10.1016/j.still.2006.11.006

Kranner, I., Kastbergerb, G., Hartbauerb, M., & Pritcharda, H. W. (2010). Noninvasive diagnosis of seed viability using infrared thermography. Proceedings of the National Academy of Sciences, 107 (8), 3912-3917. http://doi.org/10.1073/pnas.0914197107

Kranz, W. L., S. Irmak, S. J. van Donk, C. D. Yonts, and Martin, D. L. (2008). Irrigation management for corn. NebGuide G1850. University of Nebraska Extension, Lincoln. Retrieved from http://extensionpublications.unl.edu/assets/pdf/g1850.pdf

Kustas, W. P. & Norman J. M. (1999). Evaluation of soil and vegetation heat flux predictions using a simple two-source model with radiometric temperatures for partial canopy cover. Agricultural and Forest Meteorology, 94, 13-29. https://doi.org/10.1016/S0168-1923(99)00005-2

Leinonen, I., Grant, O. M., Tagliavia, C. P. P., Chaves, M. M., & Jones, H. G. (2006). Estimating stomatal conductance with thermal imagery. Plant Cell and Environment, 29, 1508-1518. https://doi.org/10.1111/j.1365-3040.2006.01528.x

Lillesaeter, O. (1982). Spectral reflectance of partly transmitting leaves: laboratory measurements and mathematical modeling. Remote sensing of Environment, 12(3), 247-254. https://doi.org/10.1016/0034-4257(82)90057-8

Lillesand, T., Kiefer, R.W., & Chipman, J. (2014). Remote sensing and image interpretation (7th ed., pp. 243-265). NJ, USA: John Wiley & Sons.

Lowry, R. L. (1942). Consumptive use of water for agriculture. Transactions of American Society of Civil Engineering, 107(1), 1243-1302. https://doi.org/10.1061/TACEAT.0005507

Maes, W. H., Huete, A. R., & Steppe, K. (2017). Optimizing the processing of UAV-based thermal imagery. Remote Sensing, 9(5), 476. https://doi.org/10.3390/rs9050476

Maes, W. H., & Steppe, K. (2012). Estimating evapotranspiration and drought stress with ground-based thermal remote sensing in agriculture: a review. Journal of Experimental Botany, 63(13), 4671-4712. https://doi.org/10.1093/jxb/ers165

Mahajan, S., & Tuteja, N. (2005). Cold, salinity and drought stresses: an overview. Archives of Biochemistry and Biophysics, 444(2), 139-158. https://doi.org/10.1016/j.abb.2005.10.018

Mahlein, A. K., Oerke, E. C., Steiner, U., & Dehne, H. W. (2012). Recent advances in sensing plant diseases for precision crop protection. European Journal of Plant Pathology, 133, 197–209. http://doi.org/10.1007/s10658-011-9878-z

Marek, T. H., Schneider, A. D., Howell, T. A. & Ebeling, L. L. (1988). Design and construction of large weighing monolithic lysimeters. Transactions of the ASABE, 31(2), 0477-0484. https://doi.org 10.13031/2013.30734

Nieto, H., Kustas, W.P., Torres-Rúa, A. et al. (2019). Evaluation of TSEB turbulent fluxes using different methods for the retrieval of soil and canopy component temperatures from UAV thermal and multispectral imagery. Irrigation Science, 37, 389–406. https://doi.org/10.1007/s00271-018-0585-9

Norman, J. M., Kustas, W. P. & Humes, K. S. (1995). Source approach for estimating soil and vegetation energy fluxes in observations of directional radiometric surface temperature. Agricultural and Forest Meteorology, 77(3-4), 263-293. https://doi.org/10.1016/0168-1923(95)02265-Y

Norman, J., Kustas, W., Prueger, J., & Diak, G. (2000). Surface flux estimation using radiometric temperature: A dual-temperature-difference method to minimize measurement errors. Water Resources Research, 36(8), 2263-2274. https://doi.org/10.1029/2000WR900033

Nugent, P. W., Shaw, J. A., & Pust, N. J. (2013). Correcting for focal-plane-array temperature dependence in microbolometer infrared cameras lacking thermal stabilization. Optical Engineering, 52(6), 061304. http://doi.org/10.1117/1.OE.52.6.061304

O'Donnell, E. M., Schott, J. R., & Raqueno, N. G. (2002). Calibration history of Landsat thermal data. IEEE International Geoscience and Remote Sensing Symposium, 1, pp. 27-29. Piscataway, NJ: IEEE. http://doi.org/10.1109/IGARSS.2002.1024930

Ortega-Farías, S., Ortega-Salazar, S., Poblete, T., Kilic, A., Allen, R., Poblete-Echeverría, C., ... Sepúlveda, D. (2016). Estimation of energy balance components over a drip-irrigated olive

orchard using thermal and multispectral cameras placed on a helicopter-based unmanned aerial vehicle (UAV). Remote Sens., 8(8), 638. https://doi.org/10.3390/rs8080638

Orżanowski, T. (2016). Nonuniformity correction algorithm with efficient pixel offset estimation for infrared focal plane arrays. SpringerPlus, 5(1), 1831. http://doi.org/10.1186/s40064-016-3534-1

Osakabe, Y., Osakabe, K., Shinozaki, K., & Tran, L. S. P. (2014). Response of plants to water stress. Frontiers in Plant Science, 5, 86. https://doi.org/10.3389/fpls.2014.00086

Osroosh, Y., Peters, R. T., Campbell, C. S., & Zhang, Q. (2015). Automatic irrigation scheduling of apple trees using theoretical crop water stress index with an innovative dynamic threshold. Computers and Electronics in Agriculture, 118, 193–203. http://doi.org/10.1016/j.compag.2015.09.006

Pen, C., Bilanski, W., & Fuzzen, D. (1985). Classification analysis of good and bruised peeled apple tissue using optical reflectance. Transactions of the ASABE, 28, 326-330. http://doi.org/10.13031/2013.32251

Perry, D. L., & Dereniak, E. L. (1993). Linear theory of nonuniformity correction in infrared staring sensors. Optical Engineering, 32(8), 1854-1860. https://doi.org/10.1117/12.145601

Piccinni, G., Ko, J., Marek, T., & Howell, T. (2009). Determination of growth-stage-specific crop coefficients (KC) of maize and sorghum. Agricultural Water Management, 96(12), 1698-1704. https://doi.org/10.1016/j.agwat.2009.06.024

Priestley, C. & Taylor, R. (1972). On the assessment of surface heat flux and evaporation using large-scale parameters. Monthly Weather Review, 100(2), 81-92. https://doi.org/10.1175/1520-0493(1972)100<0081:OTAOSH>2.3.CO;2

Ribeiro-Gomes, K., Hernández-López, D., Ortega, J. F., Ballesteros, R., Poblete, T., & Moreno, M. A. (2017). Uncooled thermal camera calibration and optimization of the photogrammetry process for UAV applications in agriculture. Sensors, 17, 2173. http://doi.org/10.3390/s17102173

Ribera, J., Chen, Y., Boomsma, C., & Delp, E. J. (2017). Counting plants using deep learning. IEEE Global Conference on Signal and Information Processing (GlobalSIP), 2017, 1344-1348. https://doi.org/10.1109/GlobalSIP.2017.8309180

Riveros-Burgos, C., Ortega-Farías, S., Morales-Salinas, L., Fuentes-Peñailillo, F., & Tian, F. (2021). Assessment of the clumped model to estimate olive orchard evapotranspiration

using meteorological data and UAV-based thermal infrared imagery. Irrigation Science, 39(1), 63-80. https://doi.org/10.1007/s00271-020-00716-w

Rondeaux, G., Steven, M., & Baret, F. (1996). Optimization of soil-adjusted vegetation indices. Remote Sensing of Environment, 55(2), 95-107. https://doi.org/10.1016/0034-4257(95)00186-7

Rossini, M., Fava, F., Cogliati, S., Meroni, M., Marchesi, A., Panigada, C., ... & Colombo, R. (2013). Assessing canopy PRI from airborne imagery to map water stress in maize. ISPRS Journal of Photogrammetry and Remote Sensing, 86, 168-177. https://doi.org/10.1016/j.isprsjprs.2013.10.002

Roujean, J. L., & Breon, F. M. (1995). Estimating PAR absorbed by vegetation from bidirectional reflectance measurements. Remote Sensing of Environment, 51(3), 375-384. https://doi.org/10.1016/0034-4257(94)00114-3

Schott, J. R., Hook, S. J., Barsi, J. A., Markham, B. L., Miller, J., Padula, F. P., & Raqueno, N. G. (2012). Thermal infrared radiometric calibration of the entire Landsat 4, 5, and 7 archive (1982–2010). Remote Sensing of Environment, 122, 41-49. https://doi.org/10.1016/j.rse.2011.07.022

Scotford, I., & Miller, P. (2004). Combination of spectral reflectance and ultrasonic sensing to monitor the growth of winter wheat. Biosystems Engineering, 87, 27-38. http://doi.org/10.1016/j.biosystemseng.2003.09.009

Sepúlveda-Reyes, D., Ingram, B., Bardeen, M., Zúñiga, M., Ortega-Farías, S., & Poblete-Echeverría, C. (2016). Selecting canopy zones and thresholding approaches to assess grapevine water status by using aerial and ground-based thermal imaging. Remote Sensing, 8(10), 822. https://doi.org/10.3390/rs8100822

Singh, R. K. & Irmak, A. (2009). Estimation of crop coefficients using satellite remote sensing. Journal of Irrigation and Drainage Engineering, 135(5), 597-608. https://doi.org/10.1061/(ASCE)IR.1943-4774.0000052

Smith, R., Barrs, H., Steiner, J., & Stapper, M. (1985). Relationship between wheat yield and foliage temperature: theory and its application to infrared measurements. Agricultural and Forest Meteorology, 36, 129-143. http://doi.org/10.1016/0168-1923(85)90005-X

Song, L., Liu, S., Kustas, W. P., Zhou, J., Xu, Z., Xia, T., & Li, M. (2016). Application of remote sensing-based two-source energy balance model for mapping field surface fluxes with

composite and component surface temperatures. Agricultural and forest meteorology, 230, 8-19. https://doi.org/10.1016/j.agrformet.2016.01.005

Sosnowski, T., Bieszczad, G., Madura, H., Kastek, M., & Firmanty, K. (2010). The calibration stand for thermal camera module with infrared focal plane array. Proceedings of SPIE, 7660, 76603Y. http://doi.org/ 10.1117/12.851144

Sridhar, V., Hubbard, K. G., You, J., & Hunt, E. D. (2008). Development of the Soil Moisture Index to Quantify Agricultural Drought and Its "User Friendliness" in Severity-Area-Duration Assessment, Journal of Hydrometeorology, 9(4), 660-676. https://doi.org/10.1175/2007JHM892.1

Stajnko, D., Lakota, M., & Hocevar, M. (2004). Estimation of number and diameter of apple fruits in an orchard during the growing season by thermal imaging. Computers and Electronics in Agriculture, 42, 31-42. http://doi.org/10.1016/S0168-1699(03)00086-3

Suárez, L., Zarco-Tejada, P. J., Sepulcre-Cantó, G., Pérez-Priego, O., Miller, J. R., Jiménez-Muñoz, J. C., & Sobrino, J. (2008). Assessing canopy PRI for water stress detection with diurnal airborne imagery. Remote Sensing of Environment, 112(2), 560-575. https://doi.org/10.1016/j.rse.2007.05.009

Swinbank, W. (1951). The measurement of vertical transfer of heat and water vapor by eddies in the lower atmosphere. Journal of Meteorology, 8(3), 135-145. https://doi.org/10.1175/1520-0469(1951)008<0135:TMOVTO>2.0.CO;2

Tang, R., Li, Z. L., Jia, Y., Li, C., Chen, K. S., Sun, X., & Lou, J. (2013). Evaluating one-and two-source energy balance models in estimating surface evapotranspiration from Landsat-derived surface temperature and field measurements. International Journal of Remote Sensing, 34(9-10), 3299-3313. https://doi.org/10.1080/01431161.2012.716529

Todd, R. W., S. R. Evett & Howell, T. A. (2000). The Bowen ratio-energy balance method for estimating latent heat flux of irrigated alfalfa evaluated in a semi-arid, advective environment. Agricultural and Forest Meteorology, 103(4), 335-348. https://doi.org/10.1016/S0168-1923(00)00139-8

Tolley, S. A., Singh, A. & Tuinstra, M. R. (2021). Heterotic Patterns of Temperate and Tropical Maize by Ear Photometry. Frontiers in Plant Science 12, 616975. https://doi.org/ 10.3389/fpls.2021.616975

Torres-Rua, A. (2017). Vicarious calibration of sUAS microbolometer temperature imagery for estimation of radiometric land surface temperature. Sensors, 17, 1499. http://doi.org/10.3390/s17071499

Twine, T. E., Kustas, W. P., Norman, J. M., Cook, D. R., Houser, P., Meyers, T. P., ... & Wesely, M. L. (2000). Correcting eddy-covariance flux underestimates over a grassland. Agricultural and forest meteorology, 103(3), 279-300. https://doi.org/10.1016/S0168-1923(00)00123-4

Villalobos, F. J., Testi, L., & Moreno-Perez, M. F. (2009). Evaporation and canopy conductance of citrus orchards. Agricultural Water Management, 96(4), 565-573. https://doi.org/10.1016/j.agwat.2008.09.016

Wang, D. C., Zhang, G. L., Pan, X. Z., Zhao, Y. G., Zhao, M. S., & Wang, G. F. (2012). Mapping soil texture of a plain area using fuzzy-c-means clustering method based on land surface diurnal temperature difference. Pedosphere, 22, 394–403. http://doi.org/10.1016/S1002-0160(12)60025-3

Wang, X., Zhao, C., Guo, N., Li, Y., Jian, S., & Yu, K. (2015). Determining the canopy water stress for spring wheat using canopy hyperspectral reflectance data in loess plateau semiarid regions. Spectroscopy Letters, 48(7), 492-498. https://doi.org/10.1080/00387010.2014.909495

Weiss, A. & Norman, J. (1985) Partitioning solar radiation into direct and diffuse, visible and near-infrared components. Agricultural and Forest meteorology, 34(2-3), 205-213. https://doi.org/10.1016/0168-1923(85)90020-6

Wilson, K. B., Hanson, P. J., Mulholland, P. J., Baldocchi, D. D., & Wullschleger, S. D. (2001) A comparison of methods for determining forest evapotranspiration and its components: sap-flow, soil water budget, eddy covariance and catchment water balance. Agricultural and Forest Meteorology, 106(2), 153-168. https://doi.org/10.1016/S0168-1923(00)00199-4

Wright, G. C., Hubick, K. T., Farquhar, G. D., & Rao, R. N. (1993). Genetic and environmental variation in transpiration efficiency and its correlation with carbon isotope discrimination and specific leaf area in peanut. Stable Isotopes and Plant Carbon-water Relations (pp. 247-267). https://doi.org/10.1016/B978-0-08-091801-3.50025-8

Yang, Y., Long, D., Guan, H., Liang, W., Simmons, C., & Batelaan, O. (2015) Comparison of three dual-source remote sensing evapotranspiration models during the MUSOEXE-12 campaign: Revisit of model physics. Water Resources Research, 51(5), 3145-3165. https://doi.org/10.1002/2014WR015619

Yildirim, E., Saraç, Ş., & Aslan, A. (2012). Energy consumption and economic growth in the USA: Evidence from renewable energy. Renewable and Sustainable Energy Reviews, 16(9), 6770-6774. https:// doi.org/10.1016/j.rser.2012.09.004

Young, S. J., Johnson, B. R., & Hackwell, J. A. (2002). An in-scene method for atmospheric compensation of thermal hyperspectral data. Journal of Geophysical Research: Atmospheres, 107(D24), ACH-14. http://doi.org/10.1029/2001JD001266

Zhang, H., Han, M., Chávez, J. L., & Lan, Y. (2017). Improvement in estimation of soil water deficit by integrating airborne imagery data into a soil water balance model. International Journal of Agricultural and Biological Engineering, 10(3), 37-46. http://doi.org/ 10.3965/j.ijabe.20171003.3081

Zhang, H., Xiong, Y., Huang, G., Xu, X., & Huang, Q. (2017). Effects of water stress on processing tomatoes yield, quality and water use efficiency with plastic mulched drip irrigation in sandy soil of the Hetao Irrigation District. Agricultural Water Management, 179, 205-214. https://doi.org/10.1016/j.agwat.2016.07.022

Zhu, Y., Irmak, S., Jhala, A. J., Vuran, M. C., & Diotto, A. (2019). Time-domain and frequency-domain reflectometry type soil moisture sensor performance and soil temperature effects in fine-and coarse-textured soils. Applied Engineering in Agriculture, 35, 117-134. http://doi.org/10.13031/aea.12908

Zhu, Y., & Cherkauer, K. (2021). Pixel-Based Calibration and Atmospheric Correction of a UAS-Mounted Thermal Camera for Land Surface Temperature Measurements. Transactions of the ASABE, 64(6), 2137-2150. https://doi.org/10.13031/trans.14631

Zhu, Y., & Cherkauer, K. A. (2019, May). Estimation of crop latent heat flux from high resolution thermal imagery. In Autonomous Air and Ground Sensing Systems for Agricultural Optimization and Phenotyping IV (Vol. 11008, p. 1100803). International Society for Optics and Photonics. https://doi.org/10.1117/12.2519216